IJL, Vol. 25, Issue 1, 2026
http://doi.org/10.31900/ijl.v25i1.581

Research Article

IRAQI JOURNAL OF LASER

The Effect of Fe Doping on the Structural and Optical Properties of (CuO:ZnO) Thin Films Prepared by the PLD Technique

Rusul R. Alrubaye* and Ghuson H. Mohammed

Department of Physics, College of Science, University of Baghdad, Iraq
**Email address of the Corresponding Author: Rusul.Abd2404m@sc.uobaghdad.edu.iq*

Article history: Received 12 May. 2025, Accepted 10 Dec. 2025, Published online 15 Jun. 2026

Abstract: This study investigates the structural and optical properties of Fe-doped (CuO: ZnO) thin films with varying Fe contents (x = 0.1–0.5%) deposited on glass substrates via pulsed laser deposition (PLD) at ambient temperature under a vacuum of 1×10^{-2} mbar. X-ray diffraction (XRD) confirmed that all films maintained a monoclinic polycrystalline structure, with grain size decreasing with increasing Fe concentration. Energy Dispersive X-ray Spectroscopy (EDS) verified the successful incorporation of Fe without altering the Cu and Zn composition. Increasing Fe concentration significantly affected the optical transmission, absorption, refractive index (n), extinction coefficient (k), and dielectric constants, demonstrating that Fe doping strongly modifies the structural, optical, and dielectric properties of CuO: ZnO thin films.

Keywords: CuO: ZnO Thin Films, PLD, XRD, Nd:YAG laser, and structural properties.

1. Introduction

Transition metal oxides (TMOs), such as CuO, ZnO, TiO_2, and NiO, represent an important class of semiconductors widely employed in electronics, catalysis, and solar energy conversion [1]. These oxides exhibit excellent energy storage capabilities and possess notable functional properties, including chemical stability, biocompatibility, and pressure and gas-sensitivity, making them suitable for a wide range of practical applications [2]. Among TMOs, copper oxide semiconductors have been extensively studied due to their unique structural and optical properties. Two stable forms of copper oxide, CuO and Cu_2O, exhibit distinct differences in colour, crystal structure, and physical properties. TMOs, including CuO and ZnO, are commonly used as functional components in photovoltaic devices, serving as absorbing layers, electron transport layers, transparent conducting electrodes, and photoanodes [3]. CuO exhibits exceptionally high melting and boiling points, making it one of the most thermally stable materials. Its monoclinic crystal structure, intrinsically stable direct band gap (E_g = 1.2–1.9 eV), and the presence of negatively charged copper vacancies acting as acceptors classify CuO as an inherent p-type semiconductor. Owing to its outstanding visible-range absorption properties, CuO is a promising candidate as an active layer in photovoltaic and solar cell applications [4, 5]. Furthermore, CuO can be synthesized using cost-effective solution-based methods and possesses several advantageous properties, including non-toxicity, chemical

stability, electrochemical activity, and the abundance of readily available raw materials [6]. Copper oxide has been extensively studied due to its suitability for a wide range of practical applications, including micro-electromechanical systems, spintronics, solar cells, and gas sensors [7]. High surface-to-volume CuO nanostructures exhibit unique chemical and physical properties, making them useful in biosensors, supercapacitors, photodetectors, solar cells, and catalysis [8]. Zinc oxide (ZnO), another semiconductor, is widely used in the fabrication of photovoltaic solar cells [9]. ZnO is safe, easy to synthesize, and exhibits strong light absorption. Because it has a direct band gap, ZnO behaves as a p-type semiconductor, with an indirect band gap of 1–1.8 eV, which is nearly ideal for solar cells and helps it absorb sunlight effectively [10]. Doping with Fe significantly affects the magnetic and electrical properties of these semiconductors [11].

In addition to modifying the material dimensions, Fe doping influences multiple physical and chemical properties, yielding materials with enhanced functional characteristics [12]. Several methods have been employed to fabricate CuO thin films, including thermal oxidation of Cu films [13], reactive DC sputtering [14], sol-gel spin coating [15], RF magnetron sputtering [16], and spray pyrolysis [17]. Pulsed laser deposition is particularly advantageous due to its simplicity, scalability, environmental friendliness, and precise control over composition and film thickness. Many studies have been conducted in recent years to develop the structural and optical properties of copper oxide (CuO) using various techniques to improve its performance in electronic and optical applications. Borah and Sarma's study showed that films prepared using continuous magnetron sputtering exhibit omnidirectional structures with grain sizes up to 26 nm. They also demonstrated that reducing the sputtering pressure increases light absorption in the 280–400 nm range and improves optical transmittance by 80% [18]. Meanwhile, Abeer and Jamal prepared thin films of CuO and CuO mixed with Nd_2O_3 using pulsed laser deposition for ammonia gas sensing. The results showed that adding Nd_2O_3 altered the crystal structure, reducing the crystal size from 19 nm to 14.7 nm, and significantly improved the optical properties [19].

Furthermore, Soumen et al.'s study, which used a simple chemical method to prepare CuO nanotubes, showed that the prepared samples possessed a monoclinic structure with a band gap ranging between (2.86-2.89 eV), where these structures showed distinct photocatalytic activity in the decomposition of methylene blue dye [20]. Abeer and Jamal's study also showed that mixing lanthanum oxide (La_2O_2) with (CuO) prepared by the PLD method contributes to increasing the band gap from (2.25) to (2.85), which confirms the possibility of modifying the structural and optical properties of (CuO) through its combination with different oxides [21]. Based on the above, these studies clearly show that the properties of (CuO) are greatly affected by the type of doping and the method of preparation. However, the effect of the iron element in the composite system (CuO: ZnO) prepared by pulsed laser deposition purification has not been systematically and in-depth studied, which represents a clear research gap that deserves investigation. Hence, the importance of this study lies in providing a detailed description of the effects of different iron concentrations on the structural and optical properties of (CuO: ZnO) films prepared by PLD, while also demonstrating the relationships among crystal structure, energy gap, and optical absorption behaviour. This aims to improve the performance of these films, making them promising materials for optical and electronic applications such as solar cells and high-efficiency sensors.

2. Experimental

The deposition process was carried out using varying concentrations of cast iron (Fe) ranging from 0.1 - 0.5% weight percentages, added to an equivalent mixture of copper oxide (CuO) and zinc oxide (ZnO). The materials were then homogeneously mixed by mechanical separation to ensure a uniform distribution of iron particles. The resulting powder was then pressed 8 tons for 10 minutes using a hydraulic press, forming discs with a diameter of 1 cm and a thickness of 1 cm. These discs were then heated at 300°C for one hour

and allowed to cool to room temperature. The discs were subsequently placed in a pulsed laser deposition chamber to deposit a film on pre-cleaned glass substrates using a mixture of salt and alcohol, followed by ultrasonic testing for 15 minutes. A pulsed Nd: YAG laser with a fundamental wavelength of 1064 nm was used, with a pulse energy of 600 mJ, a repetition rate of 6 Hz, and a spot diameter of 4 mm. The laser beam was tilted at a 45° angle to the target surface, with 400 pulses. The chamber pressure was maintained at a constant 1×10^{-2} mbar, and the distance between the laser nozzle and the target was kept at 2 cm. The resulting film thickness was approximately 200 ± 5 nm. Structural analyses were performed using X-ray diffraction within an angular range of 10°–80° with Cu-Kα radiation at a wavelength of 0.154 nm. Optical properties were measured by spectroscopy over 340–1100 nm. Figure 1 shows a diagram illustrating the pulsed laser deposition system.

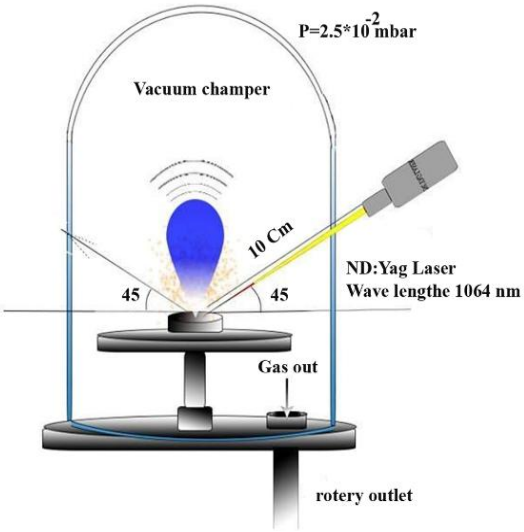

Fig. 1: Schematic illustration of the pulsed laser deposition system.

3. Result and discussion

3.1 X-ray diffraction analysis

The crystal structure of $(CuO: Zn)_{1-x}(Fe)_x$ thin films was analyzed using XRD within the 2θ range of 20°–80°. Figure 2 presents the XRD patterns of the (CuO: ZnO) Fe thin films with varying Fe concentrations. The diffraction patterns exhibit multiple peaks for all samples, confirming the polycrystalline nature of the deposited films. Four peaks were observed at 32.76°, 38.77°, 61.66°, and 66.06°, corresponding to the (110), (11–1), (111), and (–113) planes, respectively, with a preferred orientation along the (11–1) plane. These peaks can be indexed to the monoclinic structure of CuO and match well with JCPDS card No. 48-1548. Several less intense peaks were detected at 31.83°, 34.37°, and

36.45°, corresponding to the (100), (002), and (101) planes of ZnO, in agreement with JCPDS card No. 36-1451. The diffraction spectra confirm the successful crystallization of the CuO nanostructures within the deposited films. The Fe-doped films did not exhibit any secondary phases or additional peaks associated with Fe compounds. The absence of Fe-related peaks in the XRD patterns suggests that Fe ions were successfully incorporated into the CuO lattice by substituting Cu^{+} sites rather than forming separate phases. This observation indicates that the crystal structure of CuO remained stable upon Fe incorporation, confirming the successful substitution of Fe^{+} ions into the host lattice [22].

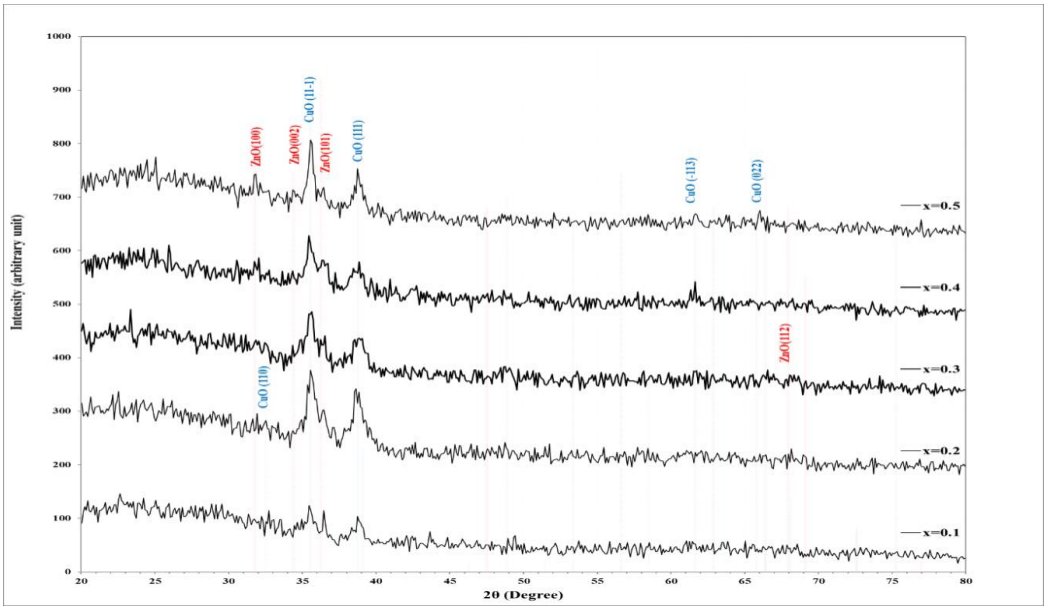

Fig.2: XRD diffraction pattern of Fe-doped CuO: ZnO thin films for different Fe content.

Scherrer's equation was used to determine and quantify the average crystallite size (L) as follows in Eq. (1), [23]:

$$L = K\lambda/\beta.\cos\theta \quad (1)$$

Where λ denotes the XRD wavelength in nanometers (nm), the value of β is the diffraction peak profile's peak width at half maximum height in radians. K is the shape factor, which is typically taken to be 0.89 for ceramic materials and, θ is the diffracted angle of the peak.

The interplanar spacing (d_{hkl}) was calculated using Bragg's law as follows in Eq. (2):

$$n\,\lambda = 2d_{hkl}\sin\theta_B \quad (2)$$

Where (θ_B) is Bragg's angle, λ is the X-ray wavelength, n is an integer representing the diffraction order (1, 2, etc.), and d_{hkl} is the interplanar spacing between two successive planes. The interplanar spacing for the samples was listed in Table 1.

The lattice constant (a) was also calculated from Eq. (3) and illustrated in Table 1.

$$\frac{1}{d^2} = \frac{h^2+k^2+l^2}{a^2} \quad (3)$$

Where (hkl) are miller indices.

The stability of the crystal structure of iron-doped (CuO: ZnO) films can be attributed to the ionic compatibility between Fe^{2+} and Cu^{2+} ions in the crystal lattice. This facilitates molecular substitution without causing significant structural distortions. It is believed that the introduction of iron into the copper sites improves intergranular bonding and reduces the density of crystal defects, which explains the appearance of the preferred orientation pattern at the (11-1) plane. The absence of additional phases further confirms that the doping did not cause chemical separation but merely stabilized the parent structure and improved its structural and optical properties.

Table 1. Structural parameters of Fe-doped CuO: ZnO thin films.

x	2θ (Deg.)	FWHM (Deg.)	d_{hkl} (Å)	D (nm)	Phase	hkl	δ ×10¹⁵ (line/m²)	ε
0.1	32.7620	0.5576	2.7313	14.9	CuO	(110)	4.5346	0.0083
	35.4569	0.6814	2.5297	12.2	CuO	(11-1)	6.6747	0.0093
	36.4481	0.4647	2.4631	18.0	ZnO	(101)	3.0870	0.0062
	38.7713	0.8364	2.3207	10.1	CuO	(111)	9.8633	0.0104
0.2	32.5452	0.5886	2.7490	14.1	CuO	(110)	5.0585	0.0088
	35.5808	0.7125	2.5211	11.7	CuO	(11-1)	7.2929	0.0097
	36.4481	0.5885	2.4631	14.2	ZnO	(101)	4.9509	0.0078
	38.6164	0.7124	2.3297	11.8	CuO	(111)	7.1623	0.0089
0.3	32.4832	0.4337	2.7717	12.8	CuO	(110)	6.1319	0.0098
	35.5498	0.7744	2.5238	19.8	CuO	(11-1)	2.5455	0.0057
	38.8023	0.9912	2.3277	21.7	CuO	(111)	2.1307	0.0048
0.4	31.9257	0.5886	2.8009	14.0	CuO	(110)	5.0743	0.0090
	35.4879	0.7434	2.5275	11.2	CuO	(11-1)	7.9433	0.0101
	36.5101	0.7434	2.4591	11.3	ZnO	(101)	7.3974	0.0098
	38.7093	0.8674	2.3243	9.7	CuO	(111)	10.6120	0.0108
	61.6004	0.5575	1.5044	16.6	CuO	(-113)	3.6335	0.0041
0.5	31.8327	0.6195	2.8089	13.3	ZnO	(110)	5.6237	0.0095
	34.3727	0.5575	2.6069	14.9	ZnO	(002)	4.4947	0.0079
	35.5498	0.4646	2.5233	18.0	CuO	(11-1)	3.1014	0.0063
	36.2932	0.5886	2.4733	14.2	ZnO	(101)	4.9570	0.0078
	38.7403	0.8363	2.3225	10.1	CuO	(111)	9.8628	0.0104
	61.6624	0.5886	1.5030	15.7	CuO	(-113)	4.0476	0.0043
	66.0609	0.5266	1.4132	18.0	CuO	(022)	3.0884	0.0035

3.2 Energy Dispersive X-ray Spectroscopy (EDS) analysis

Energy-Dispersive X-ray Spectroscopy (EDS) was performed to examine the effect of Fe incorporation on the elemental composition of the prepared films. Figure 3 presents the comparative EDS spectra obtained before and after Fe doping, highlighting changes in the intensities of Fe, Cu, and Zn peaks. Before the incorporation of Fe, the EDS spectrum exhibited prominent characteristic peaks corresponding to copper (Cu Kα ≈ 8.04 keV) and zinc (Zn Kα ≈ 8.63 keV), along with minor peaks from other trace elements. No detectable signals were observed in the energy range associated with Fe, and upon introducing a small fraction of Fe, a distinct new peak appeared at approximately 6.40 keV, corresponding to the Fe Kα line, providing qualitative confirmation of Fe incorporation into the film. The Fe Kβ line (≈ 7.06 keV The Fe Kβ line (≈ 7.06 keV) was not observed, which is expected due to the low Fe concentration and the inherently weaker intensity of the Kβ transition relative to Kα.

Notably, the intensities of Cu and Zn peaks remained nearly unchanged after Fe addition. The appearance of the Fe peak, without significant alteration in Cu and Zn intensities, indicates that Fe acted as a minor dopant incorporated into the CuO: ZnO lattice rather than substituting or diminishing the primary

constituent elements. Additional weak peaks of silicon and oxygen were also detected, originating from the underlying glass substrate. These results further confirm the successful and homogeneous incorporation of Fe within the host matrix, in good agreement with the XRD findings.

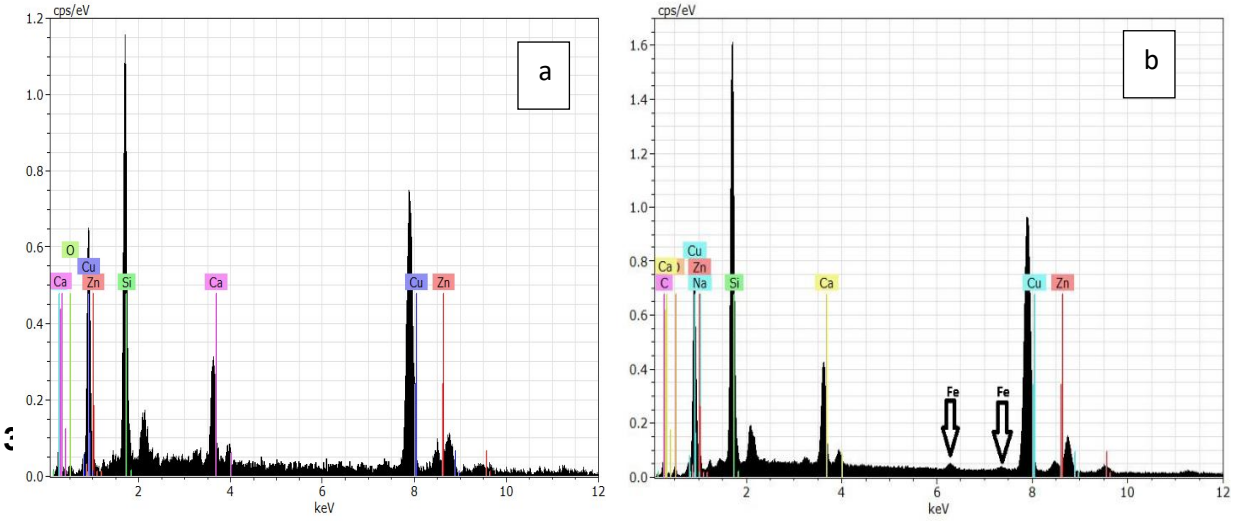

Fig.3: Energy Dispersive X-ray Spectroscopy of **a)** CuO:ZnO and **b)** Fe-doped CuO:ZnO thin films for 0.3 Fe content.

The UV–VIS–NIR spectrophotometer was employed to investigate the optical properties of the $(CuO: Zn)_{1-x}(Fe)_x$ thin films at room temperature. Figure 4 shows the variation in optical transmittance as a function of wavelength in the range of 340–1100 nm for the CuO: ZnO films doped with different Fe concentrations and deposited by the PLD technique. As illustrated in the Figure, the transmittance reached approximately 90% for the film with x = 0.1, but decreased to nearly 30% when the Fe content was increased to x = 0.5. This significant reduction in transmittance can be attributed to the formation of defect states within the band gap, which serve as additional absorption centres, as well as to modifications in the electronic structure that enhance photon absorption within the visible region. Additionally, Fe doping can influence the crystallinity and particle size of the samples, leading to enhanced light scattering and a further reduction in optical transmittance. These results are consistent with the findings reported by S. Sogan [24].

The absorption coefficient (α) was calculated using Eq. (4):

$$\alpha = 2.303A/t \quad (4)$$

Where A and t are the absorbance and film thickness, respectively.
Figure 5 presents the absorption coefficient (α) as a function of wavelength for the CuO: ZnO thin films doped with Fe (x = 0.1, 0.2, 0.3, 0.4, and 0.5). The absorption coefficient was determined by analyzing the high-absorption region near the fundamental absorption edge of the films. The results indicate that α increases progressively with increasing Fe concentration, reflecting enhanced light absorption. This behavior can be attributed to the formation of defect states and intermediate energy levels within the band gap, which facilitate electronic transitions between the valence and conduction bands. A distinct UV absorption band is observed around 340 nm in all films, while the absorbance stabilizes above 900 nm, illustrating the characteristic optical response of the Fe-doped sample.

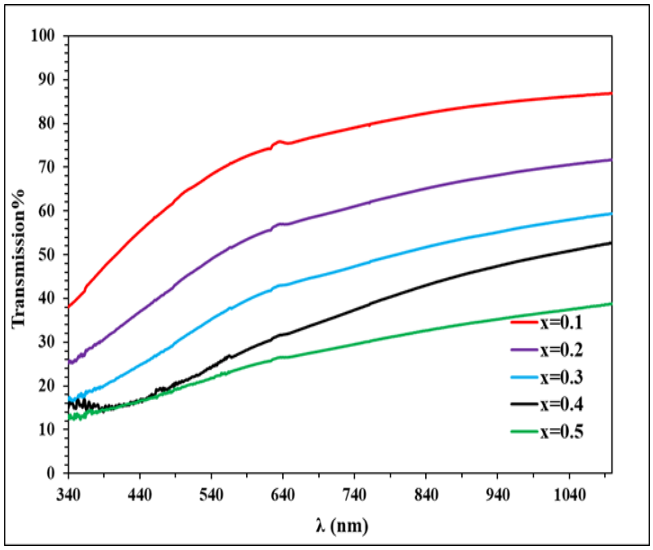

Fig.4: The variation of transmission with the wavelength for (CuO:Zn) -$_x$Fe$_x$ thin films with different concentrations of Fe.

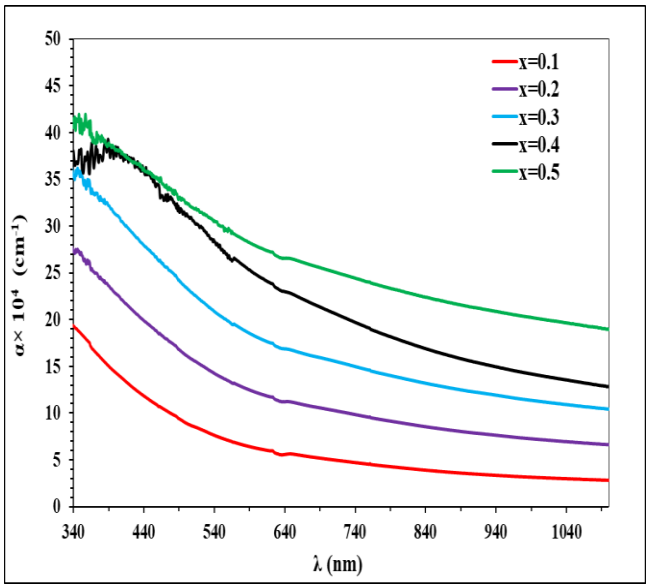

Fig.5: The absorption coefficient versus wavelength of $(CuO:Zn)_{1-x}(Fe)_x$ films prepared by PLD Technique.

The Tauc equation establishes a direct relationship between the absorption coefficient and the optical energy gap (E_g). In [25] Eq. (5),

$$(\alpha h\nu)^2 = B(h\nu - E_g) \quad (5)$$

The optical energy band gap (E_g) of the $(CuO: Zn)_{1-x}(Fe)_x$ thin films was determined using the Tauc method. In this approach, the photon energy (hν), absorption coefficient (α), Planck's constant (h), light frequency (ν), and the material-dependent parameter B—which is inversely related to amorphous content-are incorporated into the Tauc equation. The band gap was estimated by plotting $(\alpha h\nu)^2$ versus photon

energy (hν) and extrapolating the linear portion of the curve to α = 0, indicating direct allowed transitions, as shown in Figure 6.The results demonstrate that increasing Fe content leads to a progressive decrease in the optical band gap of the films. This reduction is attributed to the formation of defect states and localized energy levels within the band gap, which facilitate electronic transitions from the valence band to the conduction band, thereby lowering the energy required for these transitions. Consequently, higher Fe concentrations result in a narrower band gap and enhanced light absorption. These observations are in good agreement with previously reported studies [26, 27].

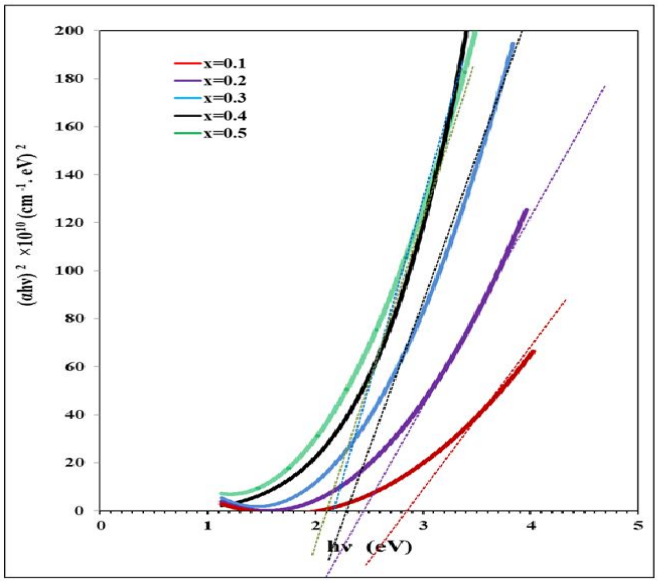

Fig.6: The Variation of (αhυ)2 with (hυ) for $(CuO:Zn)_{1-x}(Fe)_x$ thin films with different concentrations of Fe.

The refractive index (n) can be calculated from the reflectance coefficient r using Eq. (6) [28].

$$n = \text{sqrt}((1 + r) / (1 - r)) \quad (6)$$

The dependence of the refractive index on wavelength for the $(CuO: Zn)_{1-x}(Fe)_x$ thin films is presented in Figure 7.

In general, n increases with increasing wavelength, except for the films with x = 0.1 and x = 0.4. Furthermore, the refractive index decreases with the increasing Fe concentration, indicating a non-linear dependence of n on Fe doping. For low Fe concentrations (x = 0.1–0.3), n decreases with increasing wavelength because the limited number of localized defect states reduces electronic polarization.

At medium concentration (x = 0.4), n exhibits mixed behaviour, as the accumulation of defect states begins to enhance polarisation. At high concentration (x = 0.5), n increases significantly with wavelength, reflecting the pronounced influence of abundant localized states and enhanced electronic polarization. These observations are consistent with previous reports on CuO thin films prepared by the activated reactive evaporation technique, which exhibited similar refractive-index behavior [2]. The extinction coefficient was calculated using Eq. (7), [30]:

$$k = \frac{\alpha\lambda}{4\pi} \quad (7)$$

Figure 8 shows the variation of the extinction coefficient (k) as a function of wavelength for the $(CuO: Zn)_{1-x}(Fe)_x$ thin films at different Fe concentrations.

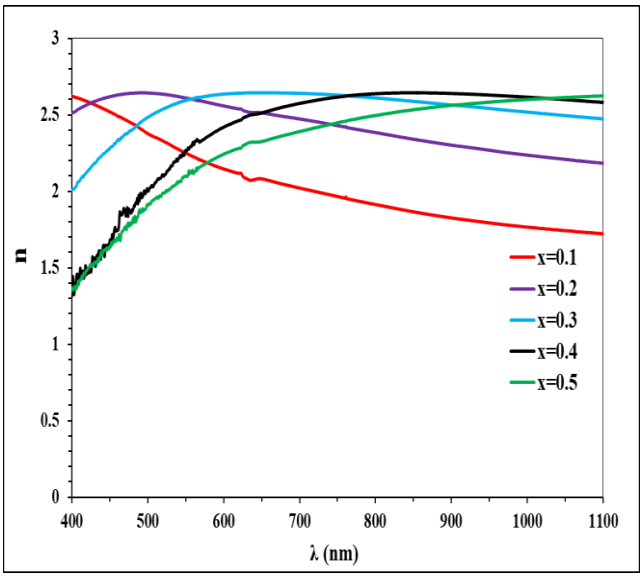

Fig.7: Variation of the refractive index (n) as a function of wavelength for $(CuO:Zn)_{1-x}(Fe)_x$ thin films with different Fe concentrations.

The results indicate that k increases progressively with increasing Fe content from x = 0.1 to 0.5. This behavior mirrors the trend observed for the absorption coefficient (α), suggesting that Fe incorporation enhances light absorption across the visible and near-infrared regions. The increase in k can be attributed to the formation of localized defect states within the lattice, which enhance electronic polarization and the interaction between light and the material. This progressive increase in k is consistent with the observed changes in refractive index, transmittance, and absorption, confirming that Fe doping effectively modifies the optical behavior of the films.

The real (εr) and imaginary (εi) parts of the dielectric constant were calculated using the following [30] relations:

$$\varepsilon r = n^2 - k^2 \quad (8)$$

$$\varepsilon i = 2nk \quad (9)$$

Figures 9 and 10 present the variations of the real (εr) and imaginary (εi) components of the dielectric constant as a function of wavelength for the $(CuO: Zn)_{1-x}(Fe)_x$ thin films with different Fe concentrations. Table 2 shows the variation in optical parameters with changes in the Fe content in the films. The film's dielectric behavior is strongly dependent on Fe content. At low Fe concentrations (x = 0.1), εr decreases while εi remains relatively high, indicating limited polarization and higher energy loss. For medium Fe concentrations (x = 0.2–0.3), εr stabilises and εi decreases gradually.

At high Fe concentrations (x = 0.4–0.5), εr increases while εi decreases, reflecting enhanced energy storage and reduced dielectric losses. These observations suggest that careful optimization of Fe content can improve the dielectric performance of CuO: ZnO films for applications in capacitors, sensors, and high-frequency devices.

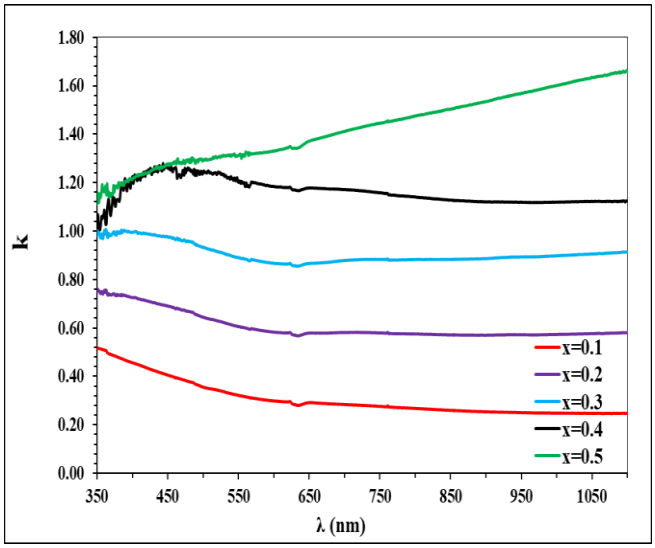

Fig.8: The variation of k with the wavelength for $(CuO:Zn)_{1-x}(Fe)_x$ thin films with different concentrations of Fe.

Table 2. Optical parameters of Fe-doped CuO: ZnO thin films.

Sample	A	T%	α (cm^{-1})	K	n	ε_r	ε_i	Eg (eV)
x=0.1	0.16	69.26	73466	0.322	2.250	4.959	1.448	2.90
x=0.2	0.30	50.04	138474	0.606	2.611	6.447	3.166	2.50
x=0.3	0.44	36.15	203482	0.891	2.594	5.934	4.623	2.30
x=0.4	0.60	25.36	274379	1.202	2.269	3.704	5.452	2.00
x=0.5	0.65	22.36	299601	1.312	2.100	2.690	5.511	2.00

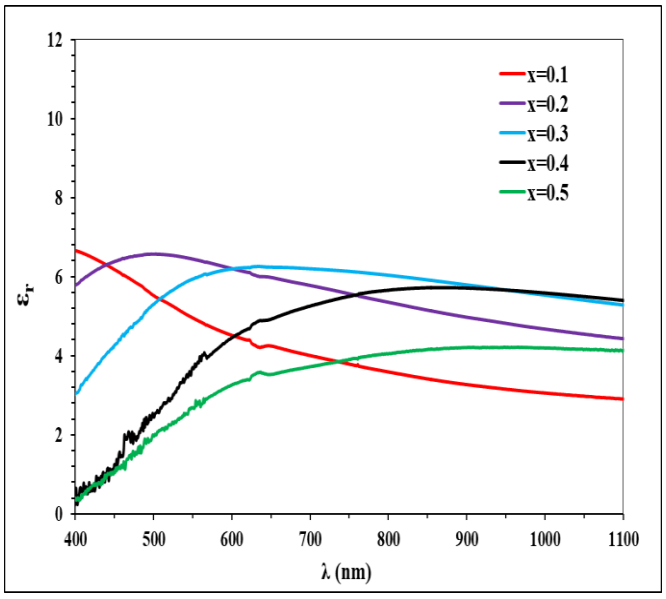

Fig.9: The variation of εr with the wavelength for $(CuO: Zn)_{1-x}(Fe)_x$ thin films with different concentrations of Fe.

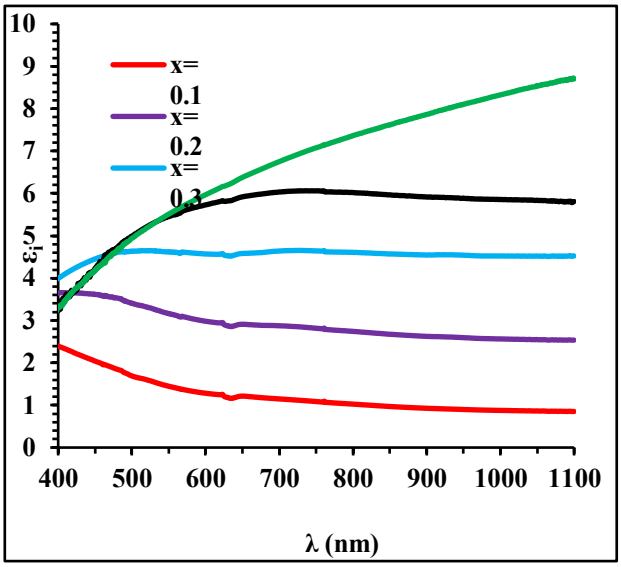

Fig.10: The variation of εi with the wavelength for $(CuO: Zn)_{1-x}(Fe)_x$ thin films with different concentrations of Fe.

4. Conclusions

Fe-doped $(CuO: Zn)_{1-x}(Fe)_x$ thin films with Fe concentrations ranging from 0.1 to 0.5% were successfully fabricated using the pulsed laser deposition (PLD) technique. The incorporation of Fe was found to significantly influence the structural, optical, and dielectric properties of the films. Specifically, Fe doping led to improved crystallinity, modified optical absorption and band gap, enhanced refractive index and extinction coefficient, and optimised dielectric behaviour. These enhancements demonstrate that Fe incorporation effectively tailors the material's performance, making the films up-and-coming for optoelectronic applications, including photovoltaic cells, optical sensors, capacitors, and high-frequency electronic devices.

References

[1] S. Siwatch, V. S. Kundu, A. Kumar, S. Kumar, N. Chauhan, & M. Kumari, "Morphology correlated efficiency of ZnO photoanode in dye sensitized solar cell," Materials Research Express, 6, 1050d3 (2019).
[2] A. S. Maktoof, G. H. Mohammed, & H. H. Abbas, "Effect of annealing process on structural and optical properties of Au-doped NiO: WO3 thin films fabricated by PLD technique," Applied Surface Science, 450, 123–130 (2022).
[3] Z. Kayani, S. Iram, R. Rafi, S. Riaz, & S. Naseem, "Effect of Cu doping on the structural, magnetic and optical properties of ZnO thin films," Applied Physics A, 124(7), 468 (2018).
[4] J. K. Wu, W. J. Chen, Y. H. Chang, Y. F. Chen, D. R. Hang, C. T. Liang, & J. Y. Lu, "Fabrication and photoresponse of ZnO nanowires/CuO coaxial heterojunction," Nanoscale Research Letters, 8, 387 (2013).
[5] M. Kawwam, F. H. Alharbi, T. Kayed, A. Aldwayyan, A. Alyamani, N. Tabet, & K. Lebbou, "Structural and optical properties of CuO thin films," Applied Surface Science, 276, 7–12 (2013).
[6] A. El-Trass, M. M. El-Khatib, A. M. Abdel-Ghany, & H. M. El-Shazly, "Structural and optical characterisation of copper oxide thin films prepared by chemical methods," Applied Surface Science, 258, 2997–3001 (2012).
[7] D. N. Jassim, J. M. Mansour, & G. H. Mohammed, "Influence of Mn2O3 concentrations on the structural and optical characterisation of ZnO: CuO thin films prepared by laser technique," Journal of Optics, (2024).
[8] S. Ghosh, P. Srivastava, B. Pandey, M. Saurav, P. Bharadwaj, D. Avasthi, D. Kabiraj, & S. Shivaprasad, "Study of ZnO and Ni-doped ZnO synthesised by atom beam sputtering technique," Materials Science and Engineering B,

90(4), 765–769 (2008).
[9] C. Gümüş, O. M. Ozkendir, H. Kavak, & Y. Ufuktepe, "Structural and optical properties of CuO thin films," Journal of Optoelectronics and Advanced Materials, 8(1), 299–303 (2006).
[10] M. Rusu, G. G. Rusu, M. Girtan, & S. Dabos Seignon, "Structural and optical characterisation of nanocrystalline CuO thin films," Journal of Non-Crystalline Solids, 345, 4461–4464 (2008).
[11] F. Zahra, et al., "Characterisation techniques of Fe-doped CuO thin films deposited by the spray pyrolysis method," arXiv preprint, arXiv:1807.09697 (2018).
[12] C. H. B. Ng & W. Y. Fan, "Optical properties of copper oxide thin films," Journal of Physical Chemistry B, 110, 20801–20806 (2006).
[13] V. Figueiredo, E. Elangovan, G. Goncalves, P. Barquinha, L. Pereira, N. Franco, E. Alves, R. Martins, & E. Fortunato, "Effect of post-annealing on the properties of copper oxide thin films obtained from the oxidation of evaporated metallic copper," Applied Surface Science, 254, 3949–3954 (2008).
[14] P. Samarasekara, N. T. R. N. Kumara, & N. U. S. Yapa, "Sputtered copper oxide (CuO) thin films for gas sensor devices," Journal of Physics: Condensed Matter, 18, 2417–2420 (2006).
[15] D. Jundale, S. Pawar, M. Chougule, P. Godse, S. Patil, B. Raut, S. Sen, & V. Patil, "Nanocrystalline CuO thin films for H2S monitoring: microstructural and optoelectronic characterisation," Journal of Sensor Technology, 1, 36–46 (2011).
[16] S. Sinthamani, M. Ranjithkumar, S. K. Bharatan, & S. Anitha, "Optical characterisation of RF sputtered copper oxide for thin film solar cell applications," Materials Today: Proceedings, 59,814–818 (2022).
[17] I. Singh & R. K. Bedi, "Studies and correlation among the structural, electrical and gas response properties of aerosol spray deposited self-assembled nanocrystalline CuO," Applied Surface Science, 257, 7592–7599 (2011).
[18] Borah, J., & Sarma, B. K. (2022). Structural, optical and electrical properties of CuO nanostructures prepared by reactive DC magnetron sputtering. Materials Today: Proceedings, 65, 2523-2528.
[19] Mohammed Enad, A., & Rzaij, J. M. (2025). Synthesis of CuO Thin Film Incorporated with Nanostructured Nd2O3 Deposited by Pulsed Laser Deposition for Ammonia Sensing Applications. Nano, 20(03), 2450113.
[20] Rakshit, S., Mondal, K. G., Jana, P. C., Kamilya, T., & Saha, S. (2023). Structural and optical properties of chemically synthesised copper oxide nanoparticles and their photocatalytic application. Journal of Materials Science: Materials in Electronics, 34(32), 2141.
[21] Enad, A. M., & Rzaij, J. M. (2025). Study on the Structural and Optical Properties of CuO Thin Films Mixed with La2O3 Deposited using Pulsed Laser Deposition for Future Optoelectronic and Gas Sensing Devices Applications. Samarra Journal of Pure and Applied Science, 7(2), 185-198.
[22] Enad, A. M., & Rzaij, J. M. (2024). Investigate the structural, morphological, and topographical characteristics of CuO thin films utilising a pulsed laser deposition method-Journal of Theoretical and Applied Physics, 18.
[23] A. B. Taha, M. S. Essa, and B. T. Chiad, "Study the effect of reaction time on preparation of iron oxide nanoparticles by hydrothermal technique," Materials Science Forum, vol. 1084, pp. 23–30, 2023.
[24] A. M. El Sayed, & M. Shaban, "Structural, optical and photocatalytic properties of Fe and (Co, Fe) co-doped copper oxide spin-coated films," Spectrochimica Acta Part A: Molecular and Biomolecular Spectroscopy, 149, 638–646 (2015).
[25] P. Rani, S. Kumar, & R. Singh, "Study of structural and optical properties of Fe-doped CuO nanoparticles," AIP Conference Proceedings, 1728(1), 057007 (2016).
[26] B. Balamurugan & B. R. Mehta, "Optical and structural properties of nanocrystalline copper oxide thin films prepared by activated reactive evaporation," Thin Solid Films, 396, 90–96 (2001).
[27] J. Pankove, Optical Processes in Semiconductors, Prentice-Hall, New Jersey, Vol. 92 (1971).
[28] E. Hecht, *Optics*, 4th ed., Addison-Wesley, San Francisco, pp. 1–690 (2002).
[29] Nesa, M. (2016). Characterisation of zinc-doped copper oxide thin films synthesised by the spray pyrolysis technique.
[30] Palik, E. D. (1991). Optical properties of solids.

تأثير التطعيم بالحديد على بعض الخصائص التركيبية والبصرية لأغشية (CuO:ZnO) الرقيقة المحضرة بتقنية الترسيب بالليزر النبضي

رسل ربيع عبدالوهاب*، غصون حميد محمد

قسم علوم الفيزياء, كلية العلوم,جامعة بغداد, بغداد,العراق.

البريد الالكتروني للباحث:Rusul.Abd2404m@sc.uobaghdad.edu.iq

الخلاصة: تمت دراسة الخصائص التركيبية والبصرية لأغشية CuO:ZnO الرقيقة المشوبة بالحديد (Fe) بتراكيز مختلفة من 0.1 الى 0.5% والمترسبة على ركائز زجاجية باستخدام تقنية الترسيب بالليزر النبضي (PLD) عند درجة حرارة الغرفة وتحت ضغط فراغي مقداره 1×10^{-2}ملي بار. أظهرت نتائج حيود الأشعة السينية (XRD) أن جميع الأغشية احتفظت ببنيتها متعددة التبلور ذات الطور الاحادي، في حين انخفض الحجم الحبيبي مع زيادة تركيز الحديد. كما أكد تحليل مطيافية تشتت الطاقة للأشعة السينية (EDS) نجاح دمج عنصر الحديد دون التأثير على نسب عنصري النحاس والزنك. وقد تبين أن زيادة تركيز الحديد تؤثر بشكل ملحوظ في النفاذية البصرية والامتصاص ومعامل الانكسار (n) ومعامل الخمود (k) والثوابت العازلة، مما يدل على أن التشويب بالحديد يحدث تغييرا جوهريا في الخصائص التركيبية والبصرية والعازلية لأغشية CuO:ZnO الرقيقة.

IJL, Vol. 25, Issue 1, 2026
http://doi.org/10.31900/ijl.v25i1.556

Research Article

IRAQI JOURNAL OF LASER

The Plasmonic Influence on the Performance of Laser-Scribed Front-Contact Gold Layer in Ultra-Thin Film Silicon Solar Cell

Rusul A. Dahab* and Hussein A. Jawad

Institute of Laser for Postgraduate Studies/ University of Baghdad/Baghdad/Iraq.
**Email address of the Corresponding Author: rusul.ahmed2301m@ilps.uobaghdad.edu.iq*

Article history: Received 23 Dec. 2025, Accepted 1 Mar. 2026, Published online 15 Jun. 2026

Abstract: Laser scribing of the front-layer metal contact in thin-film silicon solar cell is one method that enhances optical absorption through localized surface plasmon resonance (LSPR) induced at the laser-scribed gold nano-grooves. A new approach investigates both the plasmonic effect and increasing the absorption of the gold via laser scribing to improve the cell performance. A 3D ultra- thin film silicon solar cell (dimensions of $400 \times 400 \times 900$ nm^3 for width, length, and height) was designed, with a 50 nm thick gold front contact scribed at groove depths of 10, 20, 30, and 40 nm (fixed width of 100 nm). COMSOL Multiphysics software version 6.2, using the finite element method (FEM), was employed to design and numerically investigate the proposed cell. The results revealed a maximum photocurrent of 24.66 mA/cm^2 at a scribed depth of 40 nm. The laser-scribed nano-grooves excite localized surface plasmon resonances at the gold-silicon interface, enhancing electromagnetic field confinement and light trapping in the ultra-thin silicon layer. It is concluded that the laser scribing of the front gold contact improves the light absorption, leading to a significant increase in photo-generation rate and photocurrent density due to plasmonic field enhancement.

Keywords: COMSOL Multiphysics, Laser scribing, Plasmonic, Silicon.

1. Introduction

Recent global economic development has led to adverse climate changes. Therefore, efficient renewable energy sources are in high demand [1,2]. Currently, solar cells represent the essential devices that depend on the photovoltaic materials, ranging from p-n junction solar cells to dye solar cells (DSCs). DSCs have gained wide interest due to several reasons, including their environmental friendliness, low energy fabrication, and low cost, but their efficiency remains limited (maximum reported of 13 %). Perovskite solar cells improved efficiency to, 22.1 % but stability over long period is poor compared to conventional cells, which ordinary work for 25 years [3, 4].

The substantial components of the optical electronics are the semiconductor devices, including various applications such as photodetectors, photodiodes, photo sensors, and solar cells. Those devices are essential for optoelectronic, where they are distinguished by tunable properties that have attracted a great interest of researchers [5, 6]. Silicon solar cells emerged among the mentioned sources because of the low cost of the engineering process and their affinity with adaptable substrates [7].

The main issue with first-generation silicon solar cells is the active layer thickness (100 to 300 micrometers), requiring high-purity silicon and increasing costs [8]. Researchers developed thin-film solar cells to reduce thickness as much as possible, but this decreased absorption length and efficiency. Current efforts focus on maximizing absorption thin-film solar cells. A new problem

appeared, represented by the reduction of the absorption thickness of the active layer. As a result, the length of effective absorption is reduced, and for sure, the efficiency of the cell is decreased. The next purpose of the researchers is to find a certain method to increase the optical path length. The recent research works are focused on the design of thin-film solar cells with maximum absorption, without ignoring their efficiency [9-11]. The plasmonic effect enhances solar cell performance by increasing the field intensity, and hence, the produced photocurrent. In p-n junction silicon solar cells, plasmons raise light absorption, reduce exciton energy (improving photocurrent), and lengthened absorption paths (leading to increase current and voltage). Plasmonics significantly enhances efficiency [12].
The front contact of ultra-thin film solar cells affects light absorption and the efficiency, therefore, various structures were designed for this purpose. Laser-scribed metal contacts are promising, as this non-contact method minimizes damage and contamination. Laser scribing increases exposed surface area, raising absorption. The efficiency of the solar cells could be increased by laser scribing through the reduction in the optical losses. To ensure long-term stability of the scribed module, different factors should be taken into account, including the criteria of grooves and the balance between the optical and electrical losses [13, 14]. The scribing of the front layer is increasing the surface area that is exposed to the incident light, leading to raise the rate of absorption. The gold nanoparticles are widely used in solar cell due to its unique optical and electrical properties. Gold nanoparticles enhance absorption via plasmonic effect. Because of the small front-layer contact area of the thin-film solar cell, the surface area should be enlarged to get higher efficiency. The previous studies used laser scribing for the variation of the structures which cannot be obtained through traditional methods. The present work investigates the possibilities of laser scribing to get a larger surface area within similar dimensions. A new approach is investing both the plasmonic effect and increasing the absorption of the gold via laser scribing to enhance the cell performance. This work is to design and investigate an ultra-thin film silicon solar cell with a laser-scribed gold front contact to increase the optical absorption.

2. The proposed cell

The structure of ultra-thin film silicon with Laser- scribed gold layer solar cell was designed. COMSOL Multiphysics software version 6.2, using the finite element method (FEM), Electromagnetic field, Frequency Domain (EWFD), was performed to study the optical properties of the suggested design numerically, as shown in Fig. 1.

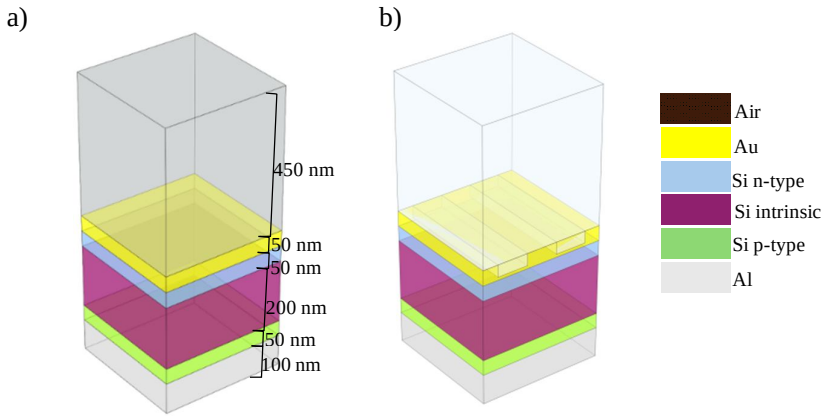

Fig. 1: The design of silicon solar cell, a) with a gold layer front contact, b) with a scribed gold front contact.

The structure of the proposed cell consisted of Au (front contact, n, k from Werner et al, 2009, 0.0176-2.48 µm), n-type Si Silicon ETL [600 Ω-cm], p-type Si, active layer/HTL (n, k from Shkondin et al.,

2017, 2-20 µm), (14 ohm-cm) and Al back reflector contact (McPeak et al., 2015). The energy band of the silicon solar cell is depicted in Fig. 2.

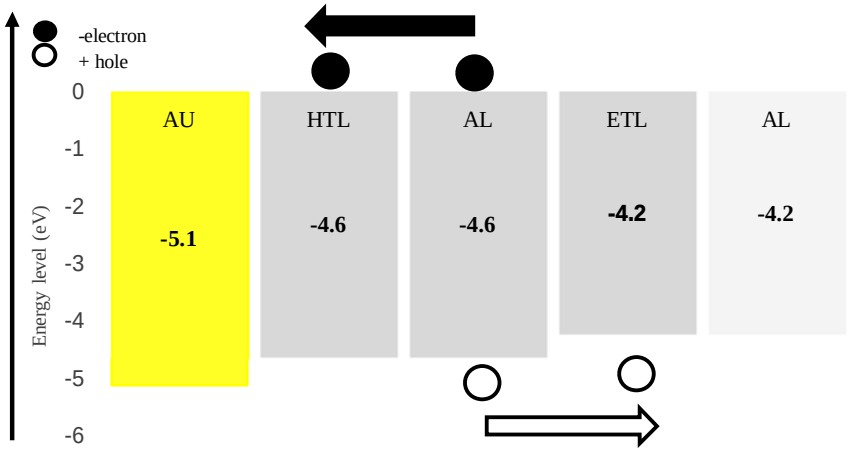

Fig. 2: Energy bands of the proposed cell.

Layer thicknesses were 450 nm air, 50 nm Au, 50 nm ETL, 200 nm AL, 50 nm HTL, and 100 nm Al from top to bottom. Cell dimensions of the cell were 400 × 400 × 900 nm³. A plane wave (y-polarized, normal incidence along z) illuminated the cell under AM1.5G spectrum (300-1300 nm, 10 nm steps). Periodic boundary conditions (PBCs, 900 nm period, Floquet type) applied in x-y direction, perfect electric conductor (PEC) on Al back. They acted as a back reflector to reflect the incident light to be absorbed again. The utilized mesh was set on a User-controlled, finer elements (max 49.5 nm, min 3,6), swept for Al/HTL/air, tetrahedral for active/ETL/Au. The width between the grooves was fixed at 100 nm, related to the gold layer width and the focal spot diameter of the laser used. To observe the effect of the groove dimension on the absorption of the cell, different depths were chosen (10-40) nm, as shown in Fig. 3.

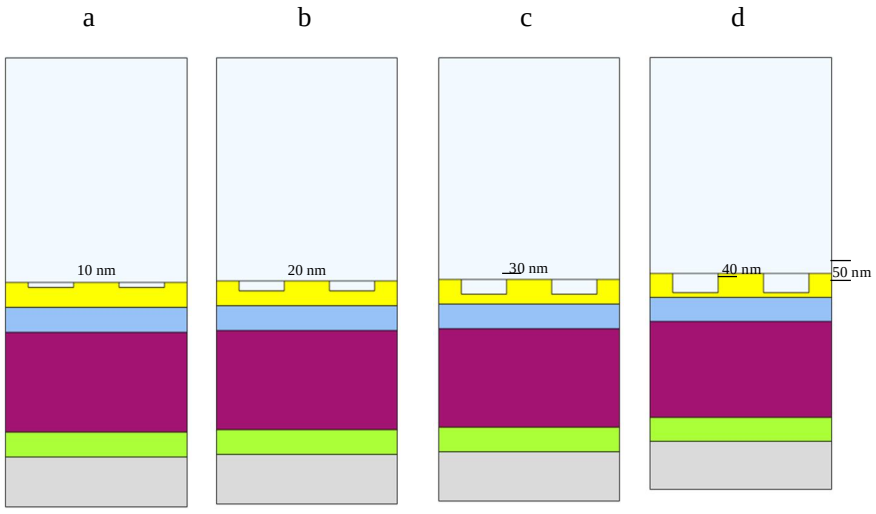

Fig. 3: The proposed cell with scribing laser groove on the front contact at varying depths: (a) 10 nm, (b) 20 nm, (c) 30 nm, and (d) 40 nm.

The optical properties of different structures used in the current study were investigated and analyzed, including (optical absorption, photo-generation rate, photocurrent density, and electric field distribution profile).

The light absorption and electromagnetic field (EM) distribution were calculated and simulated by solving the well-established Helmholtz equation $\nabla \times \nabla \times \vec{E} - k_0^2 \epsilon_r \vec{E} = 0$ [15], where K_0 is the wave vector of the incident light, ϵ_r is the dielectric permittivity of the concerned medium.

Reflection *(R(ω))* and transmission *(T(ω))* monitors were installed above and below the structure to measure the absorption *(A(ω))* by Eq. (1) [16]:

$$A(\omega) = 1 - R(\omega) - T(\omega) \quad (1)$$

The calculation of the power absorbed density in a unit cell is illustrated in Eq. (2):

$$P_{abs}(\lambda) = 0.5\omega |E(\omega)|^2 Im(\epsilon(\omega)) \quad (2)$$

The optical carrier generation rate is the number of photons absorbed in the ultra-thin film silicon solar cell per unit volume G_{ph}, and was calculated by Eq. (3) [16]:

$$G_{ph} = \int_{300}^{1300} \frac{P_{abs}}{hc/\lambda} d\lambda \quad (3)$$

Where $|E(\omega)|$ and *Im((ω))* is the electric field at angular frequency ω and the imaginary part of the dielectric constant of the material, respectively [17]. The photocurrent could be calculated as Eq. (4) [12]:

$$J_{ph}(\lambda) = \frac{e\lambda}{hc} \int_{300}^{1300} P_{abs} I_{AM.1.5}(\lambda) d\lambda \quad (4)$$

3. Result and discussion

The simulation results for the proposed cell with a 50 nm thick gold layer thickness and the solar cell with a scribed gold layer are presented and analyzed. The investigation covered normalized absorption, photo-generation rate, photocurrent density, and electric field distribution.

3.1. Normalized absorption

The normalized absorption was calculated using Eq. (2). Fig. 4 shows the absorption spectra for the proposed cell and the reference with a scribed layer. Normalized absorption as a function of wavelength is shown for different groove depths (10, 20, 30, and 40 nm).

Resonance wavelengths appeared at 400, 490, and 650 nm in the visible region, plus one peak in the IR region at 1050 nm. These optical absorptions clearly indicated the effect of plasmonic LSPR. Absorption of the resonance wavelength increased with groove depth. An IR shift in the resonance wavelength was observed with increasing depth.

This is attributed to plasmonic effect in the gold layer, which became prominent as light penetrates deeply. LSPR also indicated indication of the near-field intensity. The depth of 40 nm gives the highest absorption. The resonance wavelengths are a little bit shifted to IR. The normalized absorption for all resonance wavelengths at different depths is illustrated in Table 1.

Maximum absorption values corresponding to the groove depth are 0.39, 0.5, 0.81, and 0.87 for 10, 20, 30, and 40 nm, respectively. The influence of the groove depth on the optical absorption is shown in Fig. 5. A linear increase was observed, with maximum absorption at 40 nm. This is expected because increasing groove depth reduces the effective gold thickness, directly enhancing light absorption and revealing the plasmonic effect. Subtracting the 40 nm groove depth from the 50 nm gold thickness leave 10 nm, which supports the LSPR and enhances the plasmonic effect. Maximum normalized absorption values as a function resonance wavelength and depth are shown in Fig. 6.

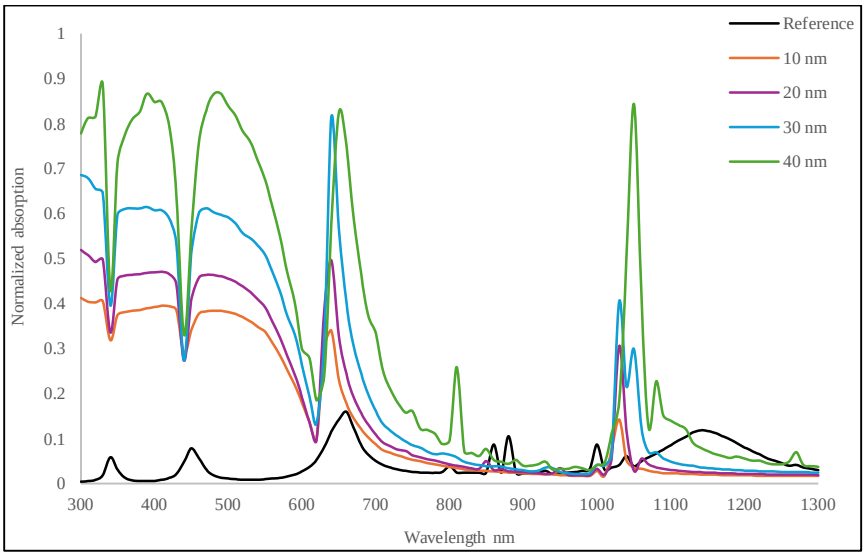

Fig. 4: Normalized absorption for the scribed laser with different groove depth (10, 20, 30, and 40) nm with the reference cell.

Table 1. Normalized absorption at each groove depth and resonance wavelengths.

λ (nm)	A (10 nm)	A (20 nm)	A (30 nm)	A (40 nm)
400	0.39	0.47	0.62	0.87
490	0.38	0.46	0.6	0.87
650	0.23	0.5	0.81	0.82
1050	0.14	0.31	0.4	0.84

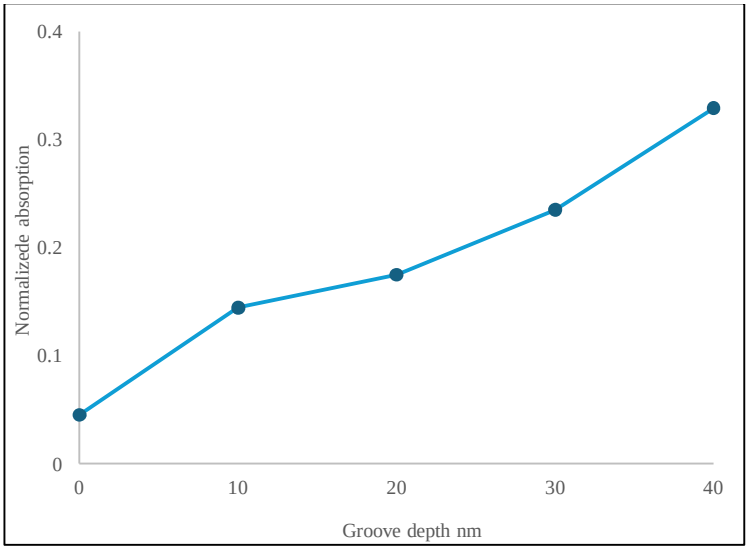

Fig. 5: Normalized absorption for the scribed laser with different groove depth (10, 20, 30, and 40) nm with the reference cell.

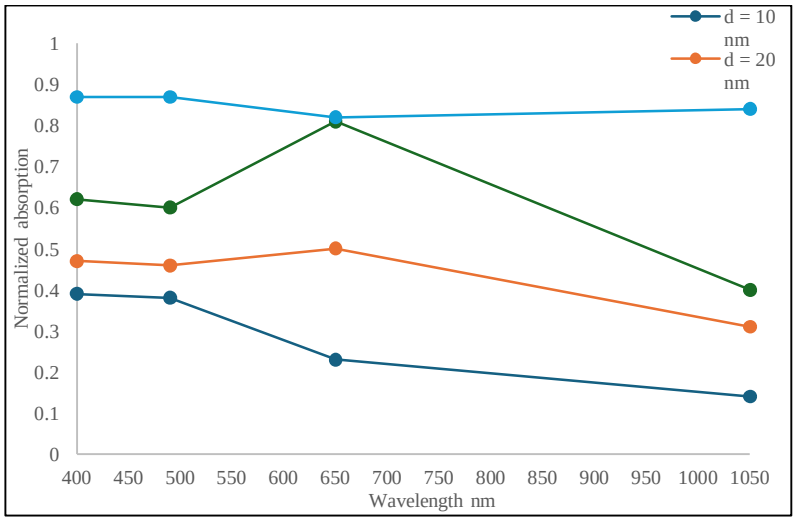

Fig. 6: Maximum normalized absorption for all resonance wavelengths at various depths (10, 20, 30, and 40) nm.

3.2. Photo-generation rate

Photo-generation rate as a function of wavelength is shown in Fig. 7, (based on Eq. 6). Similar behavior was observed across cases, with the maximum at 1050 nm, with decreasing toward shorter wavelengths and a minimum at 420 nm. Groove depth clearly influences the photo-generation rate, with deeper grooves yielding higher as absorption increases toward the electron transport layer. Surface plasmon polariton became prominent. Incident light on the gold surface, raises absorption via local surface plasmon polariton (near-field) or by scattering (far-field).

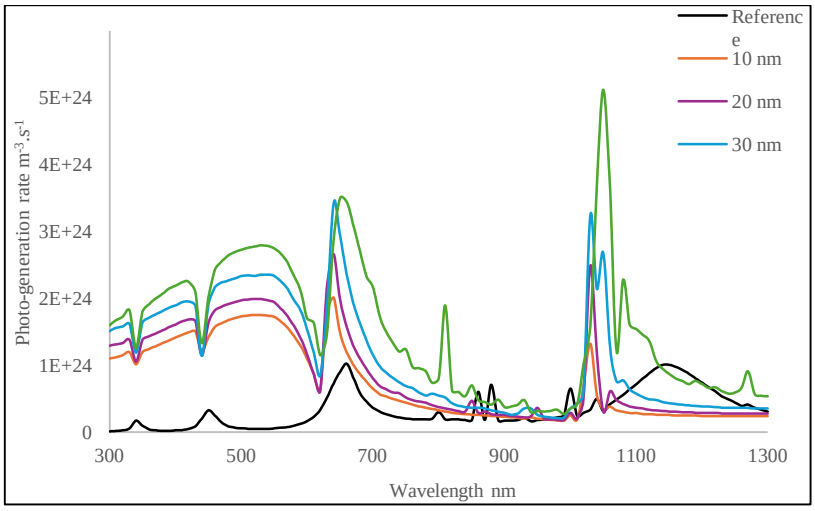

Fig. 7: Spectra of photo-generation rate for the scribed laser with different groove depth (10, 20, 30, and 40) nm with the reference cell.

The impact of groove depth on photo-generation rate is shown in Fig. 8. Similar behavior of normalized absorption was observed, remaining linear regardless of absolute values at each wavelength.

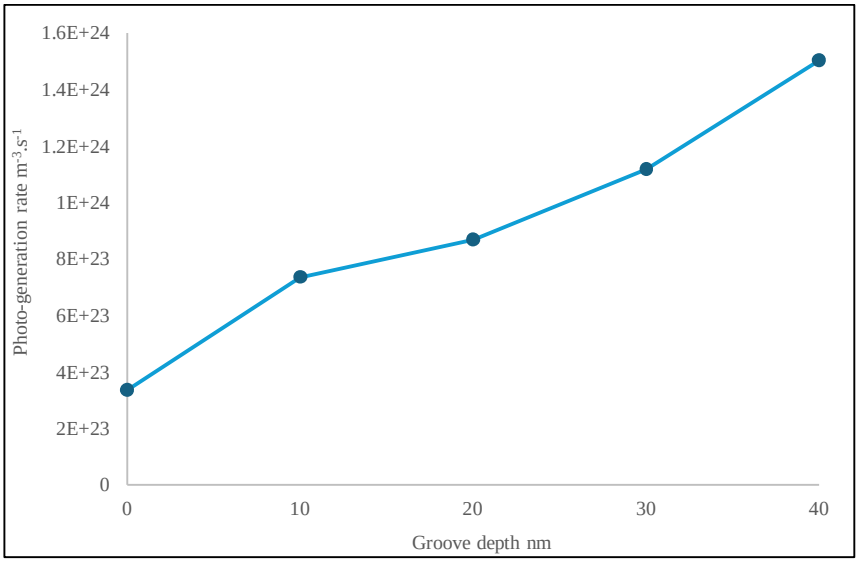

Fig. 8: Photo-generation rate for the scribed laser with different groove depth (10, 20, 30, and 40) nm with the reference cell.

Photo-generation rate represents the number of electron-hole pairs per unit volume per unit time due to the absorption of the light. Plasmonic enhanced absorption, therefore, increased the photogeneration rate.

3.3 Photocurrent density

Cell efficiency of the proposed ultra-thin film silicon solar cell with a scribed gold layer is determined by the produced photocurrent using Eq. (4) Fig. 9 shows the photocurrent versus the related wavelength. Here, the maximum photocurrent is detected at 660 nm, decreasing toward shorter wavelength then decreased toward shorter wavelengths, with another peak at1050 nm in the IR region. Photocurrent enhancement was due to increase absorption in the flowing mechanism: higher photo-generated rate, and thus greater photocurrent. This behavior is mainly influenced by the distribution of the incident light on the solar cell (A.M 1.5 G), with two peaks at 650 and 1050 nm matching high intensity region.

This wavelength was located in the maximum spectral intensity region of the incident light. It was noticed that the photocurrent of the proposed cell increased in comparison to the reference cell with a plane gold layer, indicating clearly the effect of the absorption of the incident light through the large surface area, regardless of the groove depth. Deeper grooves yielded higher photocurrent at all resonance wavelengths. Visible spectral region contributions improved overall performance related to IR. Groove depth impact on the photocurrent density was also investigated. The photocurrent density versus groove depth is shown in Fig. 10, with linear behavior.

According to equations (1), (3), and (4), photocurrent depends on the photo-generation rate, which is tied to the light absorption of the incident light.

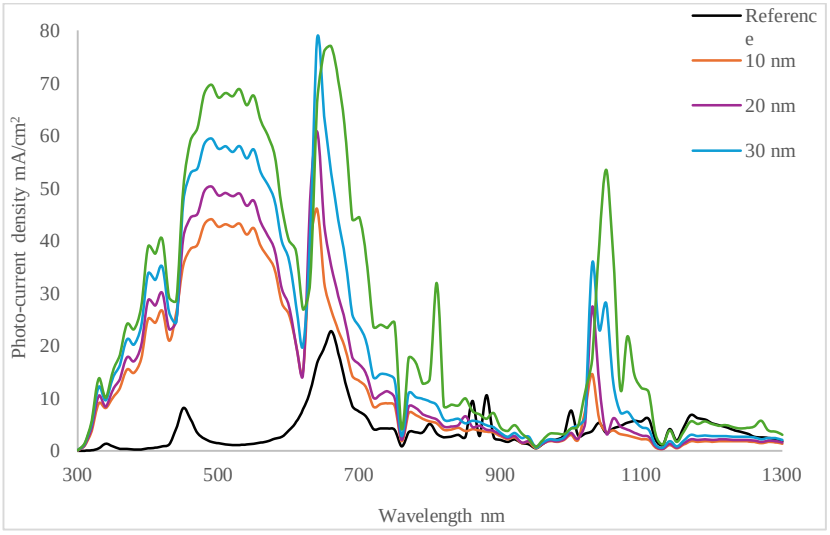

Fig. 9: Spectra of photocurrent density for the scribed laser with different groove depth (10, 20, 30, and 40) nm with the reference cell.

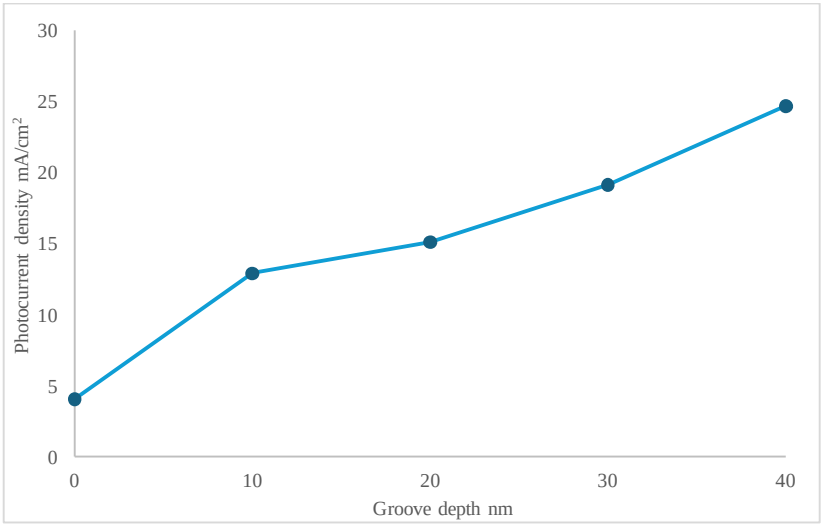

Fig. 10: Photocurrent density for the scribed laser with different groove depth (10, 20, 30, and 40) nm with the reference cell.

3.4 . Electric field distribution

Electric field scattering is related to absorption region, with maximum value at plasmonic sites (near-field LSPR or far-field scattering). Combining o LSPR (near-field enhancement) and far-field scattering (redirected light for absorption) enhance the performance of the cell. Distribution at resonance wavelengths are shown in Figs 11-14 for visible (400, 490, and 620 nm) and IR (1050 nm).

It was observed that the electric field distribution concentrated on the gold, was the strongest at groove depth edges. The difference in the field distribution intensity is related to their absorption, and the highest intensity field was observed in the deepest grooves (40 nm). Table 2 demonstrates the results of normalized absorption (A), photo-generation rate (G_{ph}), and photocurrent density (J_{ph}) for the proposed cell in comparison to the reference cell.

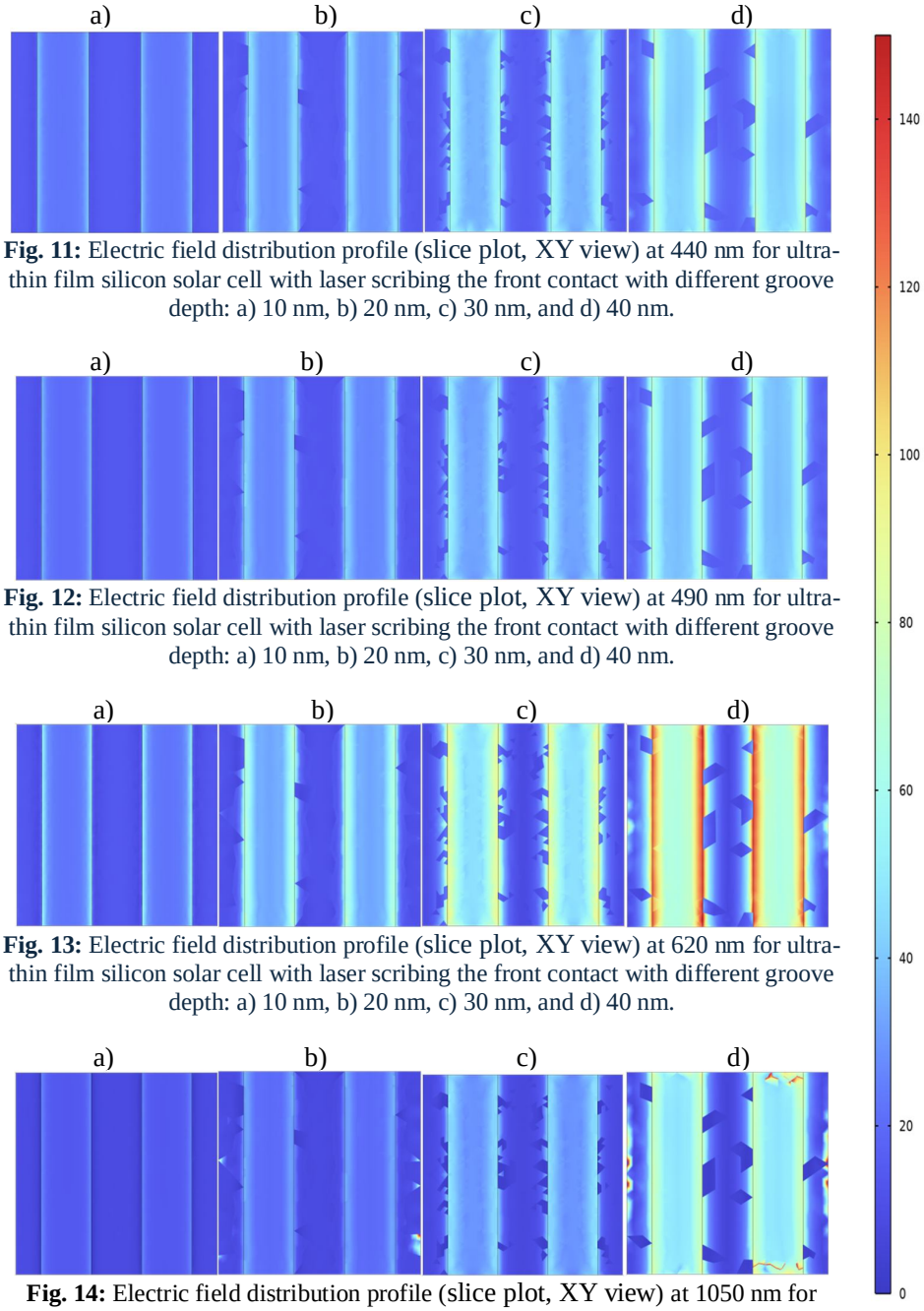

Fig. 11: Electric field distribution profile (slice plot, XY view) at 440 nm for ultra-thin film silicon solar cell with laser scribing the front contact with different groove depth: a) 10 nm, b) 20 nm, c) 30 nm, and d) 40 nm.

Fig. 12: Electric field distribution profile (slice plot, XY view) at 490 nm for ultra-thin film silicon solar cell with laser scribing the front contact with different groove depth: a) 10 nm, b) 20 nm, c) 30 nm, and d) 40 nm.

Fig. 13: Electric field distribution profile (slice plot, XY view) at 620 nm for ultra-thin film silicon solar cell with laser scribing the front contact with different groove depth: a) 10 nm, b) 20 nm, c) 30 nm, and d) 40 nm.

Fig. 14: Electric field distribution profile (slice plot, XY view) at 1050 nm for ultra-thin film silicon solar cell with laser scribing the front contact with different groove depth: a) 10 nm, b) 20 nm, c) 30 nm, and d) 40 nm.

Table 2. Performance comparison of the scribed laser front contact layer silicon solar cell with different groove depths.

Groove depth (nm)	Reference cell	10	20	30	40
Normalized absorption	0.05	0.14	0.17	0.23	0.33
G_{ph} $\times 10^{24}$ ($m^{-3}.s^{-1}$)	0.34	0.74	0.87	1.12	1.5
J_{ph} (mA/cm^2)	4.06	12.92	15.09	19.13	24.66

It was observed that the behavior of the electric field for all resonance wavelengths reflects the absorption of incident light and hence boosting in electric field via the plasmonic effect.

Limitations of the work included small cell dimensions of the proposed cell and manufacturing cost.

4. Conclusion

The extracted results showed clear improvements in ultra-thin-film silicon solar cells using laser scribing for the gold layer. LPRS (near-field) depends mainly on the light absorbed via enlarged gold surface area and light trapping, enhancing absorption through local surface plasmon polariton (near-field) or by scattering (far-field). Performance enhancement of the optical properties was (0.33, 1.5 $m^{-3}.s^{-1}$, 24.66 mA/cm^2) for normalized absorption, photo-generation rate, and photocurrent density, respectively. The increasing of absorption was leading to an increment in the photo-generated rate, reaching to the final result of a rise in the produced photocurrent. The depth of the scribed groove influenced clearly on the cell performance, the deepest groove (40 nm) performs the best, representing the thinnest gold (10 nm remaining), minimizing optical losses and increased absorption at resonance wavelengths. COMSOL is distinguished in handling complex multiphysics simulations, such as electromagnetic waves, multi-layered thin films, and field distributions for absorption efficiency. The proposed cell advances high-efficiency ultra-thin film silicon designs.

References

[1] AL-Hamdani, A., Blawa, B., & Al-Bayati, E. M. (2011). Hybrid (Luminescent and Fresnel) Concentrators to Improve Solar Panel Conversion Efficiency. Baghdad Science Journal, 8(2), 20. https://doi.org/10.21123/bsj.2011.8.2.577-580.
[2] Geng, C., Chen, X., Li, S., Ding, Z., Ma, W., Qiu, J., ... & Fan, H. J. (2021). Graphene quantum dots open up new prospects for interfacial modifying in graphene/silicon Schottky barrier solar cell. Energy Material Advances. DOI: 10.34133/2021/8481915.
[3] Abd alkareem Fadhil, E., & Abdullah, M. M. (2020). CdSe/ZnS core/shell for luminescent solar concentrator. Iraqi Journal of Science, 1645-1649. https://doi.org/10.24996/ijs.2020.61.7.12.
[4] Kong, X., Zhang, L., Liu, B., Gao, H., Zhang, Y., Yan, H., & Song, X. (2019). Graphene/Si Schottky solar cells: a review of recent advances and prospects. RSC advances, 9(2), 863-877. DOI: 10.1039/C8RA08035F.
[5] Sibu, G. A., Gayathri, P., Akila, T., Marnadu, R., & Balasubramani, V. (2024). Manifestation on the choice of a suitable combination of MIS for proficient Schottky diodes for optoelectronic applications: A comprehensive review. Nano Energy, 125, 109534. https://doi.org/10.1016/j.nanoen.2024.109534.
[6] Gatea, M. A., Jawad, H. A., & Hamidi, S. M. (2019). Detecting the thermoplasmonic effect using ellipsometry parameters for self-assembled gold nanoparticles within a polydimethylsiloxane matrix. Applied Physics A, 125(2), 103. https://doi.org/10.1007/s00339-019-2401-7.
[7] Heidarzadeh, H., & Shahabi, T. (2025). Boosting optical current in amorphous silicon solar cells using Multi-layer bimetallic plasmonic Nano-ring structures. Plasmonics, 1-10. https://doi.org/10.1007/s11468-025-02759-1.
[8] Green, M. A. (2009). The path to 25% silicon solar cell efficiency: History of silicon cell evolution. Progress in photovoltaics: research and applications, 17(3), 183-189. https://doi.org/10.1002/pip.892
[9] Heidarzadeh, H., Rostami, A., Matloub, S., Dolatyari, M., & Rostami, G. (2015). Analysis of the light trapping effect on the performance of silicon-based solar cells: absorption enhancement. Applied Optics, 54(12), 3591-3601. doi.org/10.1364/AO.54.003591.
[10] Trompoukis, C., Abdo, I., Cariou, R., Cosme, I., Chen, W., Deparis, O., ... & Depauw, V. (2015). Photonic nanostructures for advanced light trapping in thin crystalline silicon solar cells. physica status solidi (a), 212(1), 140-155. https://doi.org/10.1002/pssa.201431180.
[11] Heidarzadeh, H., Dolatyari, M., Rostami, G., & Rostami, A. (2015, June). Modeling of solar cell efficiency improvement using pyramid grating in single junction silicon solar cell. In 2nd International Congress on Energy Efficiency and Energy Related Materials (ENEFM2014) Proceedings, Oludeniz, Fethiye/Mugla, Turkey, October 16-19, 2014 (pp. 61-67). Cham: Springer International Publishing. https://doi.org/10.1007/978-3-319-16901-9_8

[12] Abdulmalek, N. M., & Jawad, H. A. (2023). Combination of near-field and scattering effects in plasmonic perovskite solar cell including cobalt doped nickel oxide HTL. Optik, 280, 170808. https://doi.org/10.1016/j.ijleo.2023.170808.
[13] de Oliveira, P. R., de Freitas, R. C., de Souza Carvalho, J. H., Camargo, J. R., e Silva, L. R. G., & Janegitz, B. C. (2024). Overcoming disposable sensors pollution: using of circular economy in electrodes application. Current Opinion in Environmental Science & Health, 38, 100540. https://doi.org/10.1016/j.coesh.2024.100540.
[14] Sadhukhan, S., Acharya, S., Panda, T., Mandal, N. C., Bose, S., Nandi, A., ... & Saha, H. (2022). Evolution of high efficiency passivated emitter and rear contact (PERC) solar cells. In Sustainable Developments by Artificial Intelligence and Machine Learning for Renewable Energies (pp. 63-129). Elsevier. https://doi.org/10.1016/B978-0-323-91228-0.00007-0.
[15] Chen, Y., Du, C., Sun, L., Fu, T., Zhang, R., Rong, W., ... & Shi, D. (2021). Improved optical properties of perovskite solar cells by introducing Ag nanopartices and ITO AR layers. Scientific Reports, 11(1), 14550. https://doi.org/10.1038/s41598-021-93914-1.
[16] Mehrpanah, A., Saghai, H. R., Sakkaki, B., & Daghigh, A. (2025). Design of Graphene-Based Core/Shell Nanoparticles to Enhance the Absorption of Thin Film Solar Cells. Plasmonics, 20(6), 3051-3057. https://doi.org/10.1007/s11468-024-02476-1.
[17] Singh, G., & Verma, S. S. (2019). Design and analysis of thin film GaAs solar cells using silver nanoparticle plasmons. Photonics and Nanostructures-Fundamentals and Applications, 37, 100731. https://doi.org/10.1016/j.photonics.2019.100731.
[18] Elshorbagy, M. H., García-Cámara, B., López-Fraguas, E., & Vergaz, R. (2019). Efficient light management in a monolithic tandem perovskite/silicon solar cell by using a hybrid metasurface. Nanomaterials, 9(5), 791. https://doi.org/10.3390/nano9050791.

التاثير البلازموني على اداء الخلية الشمسية السليكونية فائقة الدقة ذات طبقة الذهب الامامية المحفورة بالليزر

رسل احمد ذهب*، حسين علي جواد

فرع التطبيقات الهندسية والصناعية، معهد الليزر للدراسات العليا، جامعة بغداد، بغداد، العراق

البريد الالكتروني للباحث: *rusul.ahmed2301m@ilps.uobaghdad.edu.iq*

الخلاصة: الحفر بالليزر لطبقة المعدن الأمامية من الخلية السليكونية فائقة الدقة تعتبر احد الطرق التي تحسن الأداء من خلال زيادة المساحة السطحية لطبقة المعدن والتي تؤدي إلى امتصاص اعلى. لهذا الغرض، تم تصميم خلية سليكونية فائقة الدقة ذات الطبقة الأمامية من الذهب بالأبعاد nm^3 (400×400×900) للطول والعرض والارتفاع تواليا حيث كان سمك طبقة الذهب هو 50 nm. تم اجراء عملية الحفر على طبقة الذهب بمختلف الأعماق (10, 20, 30, 40) nm وبعرض ثابت قدره 100 nm. استخدم البرنامج الحاسوبي COMSOL بطريقة العناصر المحدودة FEM لتصميم وبحث النتائج رقميا. أظهرت النتائج المستخلصة ان التيار الصوئي النتاتج من الخلية المفترضة هو $26.66\ mA/cm^2$ والذي يمثل اعلى قيمة تيار عند العمق 40 nm . يمكن ان نستنتج بان الخلية السليكونية ذات دقة الذهب المحفورة تؤدي إلى زيادة التيار المنتج في الخلية مما يؤدي إلى تحسن الأداء.

IJL, Vol. 25, Issue 1, 2026
http://doi.org/10.31900/ijl.v25i1.559

Research Article

IRAQI JOURNAL OF LASER

Surface Modification of Ti6Al4V Alloy by Q-switched Nd: YAG Laser

Fatima F. Hasan[1], Haider Y. Hammod[1,]*, Mohammed. K. Khalaf[2]

[1]*Department of Physics, College of Science for Women, University of Baghdad, Iraq*
[2]*Scientific Research Commission, Baghdad, Iraq*
* *Email address of the Corresponding Author: dr.hayder.y.phy@gmail.com*

Article history: Received 3 Jan. 2026, Accepted 4 Mar. 2026, Published online 15 Jun. 2026

Abstract: In this study, Ti6Al4V alloy was exposed to a Q-switched Nd:YAG laser (wavelength 1064 nm, 6 Hz repetition rate, 10 ns pulse duration, and 4 mm spot size) with energies of (280-460) mJ. This process is referred to as laser surface modification (LSM). The effect of laser energy on crystalline structure, surface wettability, hardness, and topography was systematically evaluated using appropriate measurement techniques such as (XRD, contact angle, Vickers micro hardness tester, SEM). Significant increases were observed in hardness and wettability during the decrease in the contact angle and along with an enhancement in other surface properties.

Keywords: Surface modification, laser energy, wettability, microhardness, Ti6Al4V, Nd:YAG laser.

1. Introduction

Titanium alloys are frequently implanted into the human body to enhance physiological processes[1, 2] . The field of biomaterial study is multidisciplinary, encompassing elements of chemistry, physics, biology, medicine, and materials science. A biomaterial is a non-viable substance used in medical devices that are meant to interact with biological systems to assess, treat, enhance, or replace any bodily tissue, organ, or function[3].

The development of biomedical implants and tissue engineering heavily depends on the functionality and uses of biomaterials in biological systems. The human body can employ a wide range of biomaterials, including metals (such as stainless steel, cobalt alloys, and titanium alloys), ceramics (such as aluminum oxide, zirconium, and calcium phosphates), and synthetic and natural polymers [4]. Among these, titanium (Ti) and titanium alloys are regarded as some of the most important biomaterials because of their high corrosion resistance, great tensile strength, flexibility, and resistance to the effects of bodily fluids. This particular combination of strength and biocompatibility [5, 6] makes them appropriate for use in medical applications. For instance, the most common material for dental implants is commercially pure titanium (c.p.Ti), whereas Ti-6Al-4V alloy is employed for orthopedic applications[7-9].

Bioactive surface coatings have been widely explored to enhance the biological performance of titanium-based implants. Coatings such as hydroxyapatite (HA) and titanium oxide (TiO_2) layers are known to improve cell adhesion, osseointegration, and corrosion resistance. These coatings act as a complement to physical surface modification methods and have been successfully applied in various biomedical

applications, providing a favorable environment for bone integration and long-term implant stability[10]. Despite concerns regarding the potential biological effects of alloying elements such as aluminum and vanadium, Ti-6Al-4V remains one of the most widely used titanium alloys in biomedical applications. This widespread use is attributed to its excellent mechanical strength, high corrosion resistance, favorable fatigue behavior, and long-term clinical performance[11].

Numerous in vitro and in vivo studies have demonstrated that Ti-6Al-4V exhibits acceptable biocompatibility and minimal ion release under physiological conditions, particularly when a stable oxide layer is present on the surface. Consequently, Ti-6Al-4V continues to be extensively employed in orthopedic and dental implants, with surface modification techniques commonly applied to further enhance its biological response[12].

Therefore, this study aims to investigate the effects of laser surface modification (LSM) on the Ti6Al4V alloy, focusing not only on surface properties such as roughness, wettability, and hardness, but also on their potential impact on cell adhesion and osseointegration, which are critical for biomedical applications. It should be noted that the present study focuses exclusively on Ti6Al4V alloy, and no comparative evaluation with commercially pure titanium (CP-Ti) or other biomaterials, such as polymers or ceramics, was conducted. The main objective is to investigate the effects of LSM on the surface properties of this alloy, while comparative studies with other materials could be considered in future research.

2. Materials and Methods

2.1 Specimen Preparation

Ti6Al4V alloy specimens were prepared by sequential grinding and mirror polishing [13]. The specimens were first ground using a series of silicon carbide (SiC) papers with grain sizes of 180, 400, 600, 800, 1000, 1200, and 2500 μm, employing the KNUTH-ROTOR 2 system (Denmark). Polishing was then carried out using DP-cloth and DP-suspension (1 μm and ¼ μm) to achieve a mirror-like surface finish as shown in Fig.1.

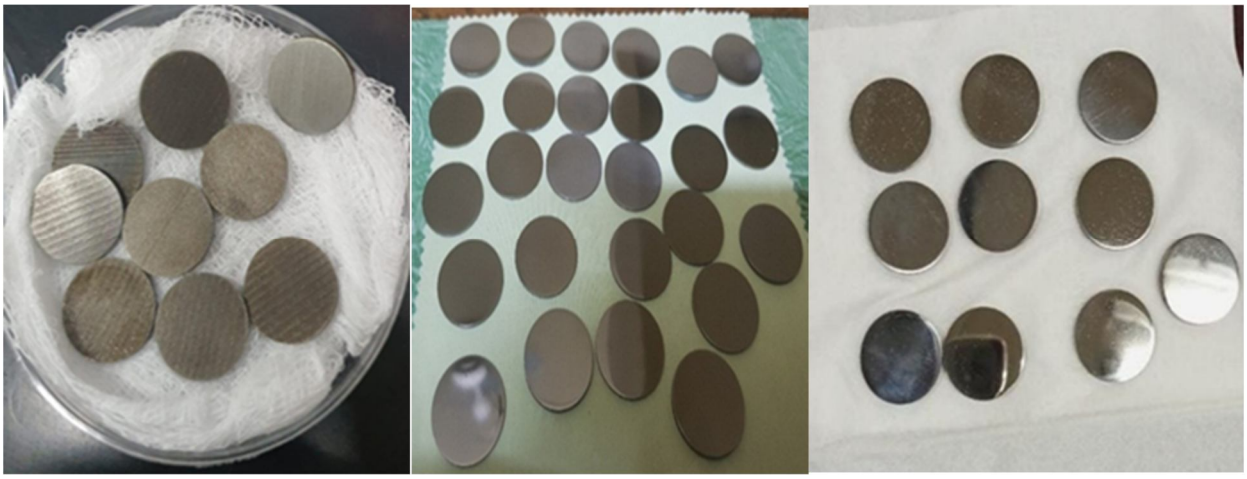

Fig.1: Photograph of mirror-polished Ti6Al4V alloy specimens after sequential grinding and polishing, showing smooth reflective surfaces used for laser surface modification experiments.

2.2 Experimental Setup for Laser-Induced Plasma (LIP) System

Surface treatment of Ti6Al4V specimens was performed using a Q-switched Nd:YAG laser with the following parameters:

- Wavelength: 1064 nm
- Pulse duration: 10 ns
- laser energies: 280, 340, 400, and 460 mJ
- repetition rate: 6 Hz
- spot size: 4mm

All experiments were conducted in air. The laser beam was focused onto the sample surface using a lens positioned at a 45° angle relative to the beam direction, with a working distance of approximately 10 cm. Plasma emission from the laser-treated surface was collected using an optical fiber (125 µm core diameter) positioned 10 cm from the target, and analyzed with a spectrometer, as shown schematically in Fig.2.

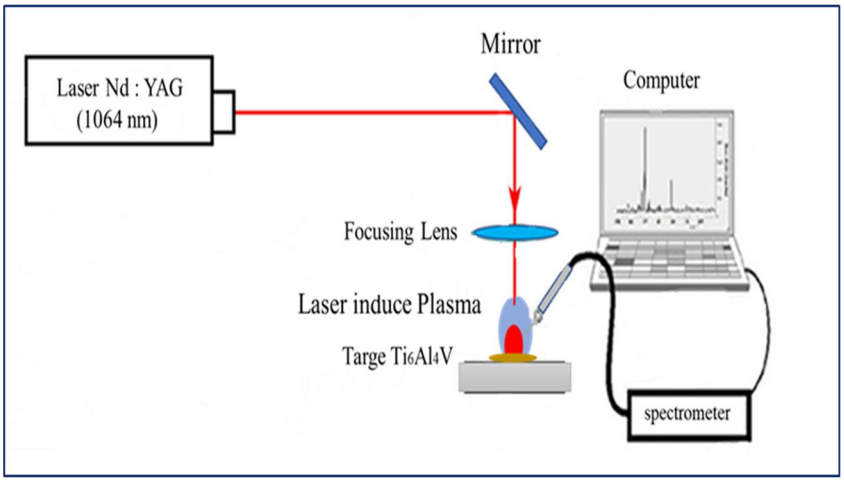

Fig.2: Schematic illustration of the laser-induced plasma system used for surface modification of Ti6Al4V alloy.

3. Results and Discussion

3.1. X-Ray Diffraction (XRD) measurements

XRD analysis of untreated and laser-treated Ti6Al4V samples (laser energies: 280, 340, 400, 460 mJ; repetition rate: 6 Hz) confirmed that all diffraction peaks correspond to the α-Ti phase with a hexagonal close-packed (HCP) structure. Peaks at 2θ angles of 35.6, 38.7, 40.6, 53.5, 63.7, 71.3, 75.2, and 78.8° correspond to the (010), (002), (011), (012), (110), (013), (112), and (021) planes of Ti, with no additional peaks indicating secondary phases (Fig. 3). Average crystallite sizes, calculated using the Debye–Scherrer equation [14], were assigned as follows: untreated sample (32.08 nm), 280 mJ (31.81 nm), 340 mJ (22.5 nm), 400 mJ (26.9 nm), and 460 mJ (31.05 nm).

$$D = \frac{k\lambda}{(\beta \cos\theta)} \quad (1)$$

Where λ is the X-ray wavelength, β is the full width at half maximum (FWHM) of the peaks at the θ diffracting angle with respect to Bragg's angle position, D is the crystallite size and k is the Scherer's constant (k = 0.9).

The reduction in crystallite size at lower laser energies indicates grain refinement due to rapid melting and resolidification induced by laser irradiation. This refinement is associated with increased defect density and enhanced surface activity. At higher laser energies, a slight increase in crystallite size is observed, likely

due to crystal rearrangement. Peak broadening is mainly attributed to reduced crystallite size and residual strain, while instrumental broadening was minimized through standard calibration. A noticeable reduction in peak intensity is observed after laser treatment compared to the untreated sample, which is attributed to grain refinement and stress generated during the rapid laser-induced thermal process. Although lattice parameters and residual stresses were not calculated in this study, these factors may be considered in future work to provide a more comprehensive structural analysis.

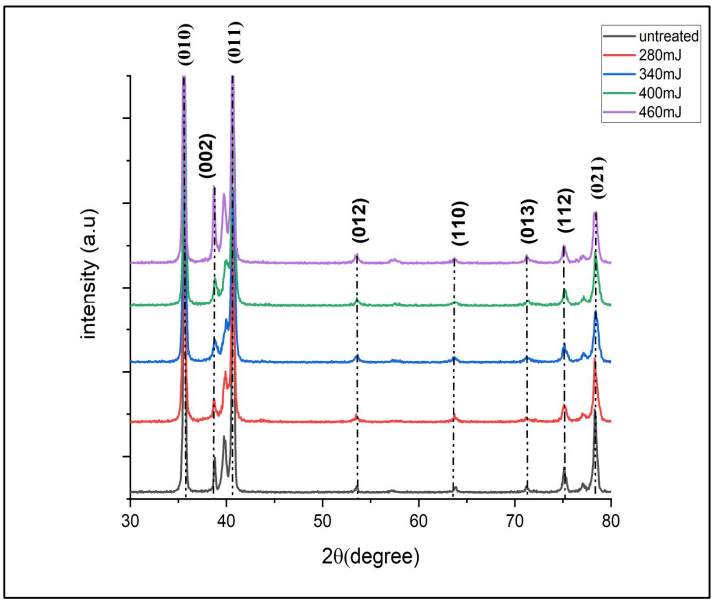

Fig. 3: XRD patterns of untreated and laser-treated Ti6Al4V samples at various laser energies.

3.2. Surface Wettability

Contact angles were measured by placing a 2 μL water droplet on the sample surface and photographing the droplet (Fig. 4). The laser-treated Ti6Al4V samples exhibited a modest decrease in contact angle compared to the untreated sample. The untreated surface showed the highest contact angle, indicating relatively low surface energy and the absence of significant topographical or chemical modifications. Although surface roughness measurements (e.g., AFM or profilometry) were not performed, the observed trend is consistent with the expected effect of laser-induced surface roughness on wettability, as described by Wenzel's model. The measurement was performed twice for each sample and at different locations on the surface.

Table 1. show how laser energy affects the contact angle of the Ti6Al4V alloy.

Condition		Contact angle	
Repetition Rate	**Energy**	**CA left [°]**	**CA right [°]**
Untreated	Untreated	103.92	103.72
6Hz	280mJ	94.6	94.89
6Hz	340mJ	94.49	94.28
6Hz	400mJ	92.64	91.02
6Hz	460mJ	92.39	92.66

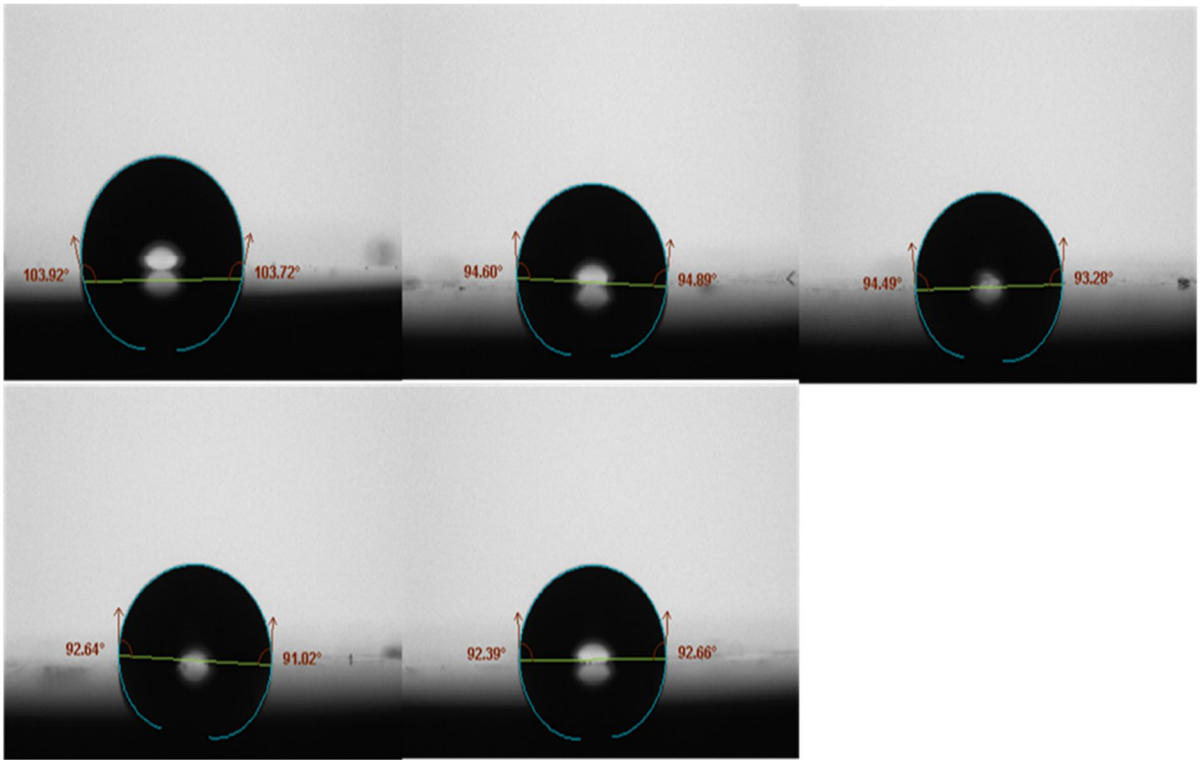

Fig. 4: Variation of water contact angle on Ti6Al4V surfaces treated with different laser energies, showing a decrease in contact angle and enhanced surface wettability due to laser-induced microstructural modifications.

3.3. Hardness

Microhardness measurements were performed using a digital Vickers microhardness tester (HVS-1000, China) under a load of 4.9 N for 15 s. The untreated sample exhibited the lowest hardness (240 HV). Increasing the laser energy from 280 to 460 mJ resulted in a gradual increase in hardness, reaching 301 HV at the highest energy. This enhancement is attributed to surface melting followed by rapid cooling, which produces a fine microstructure, refines grains, and increases dislocation density and residual stresses, thereby limiting plastic deformation and improving hardness. Each hardness value represents the average of three measurements. Based on the data mentioned above, a graph can be created to illustrate the effect of laser energy on the microhardness of the samples.

Table 2. Microhardness (HV) of the Ti6Al4V alloy as a function of laser energy

Repetition Rate	Energy (mJ)	Hardness (HV)
Untreated	Untreated	240 ± 3
6 Hz	280	247 ± 2
6 Hz	340	261 ± 4
6 Hz	400	285 ± 3
6Hz	460	301 ± 2

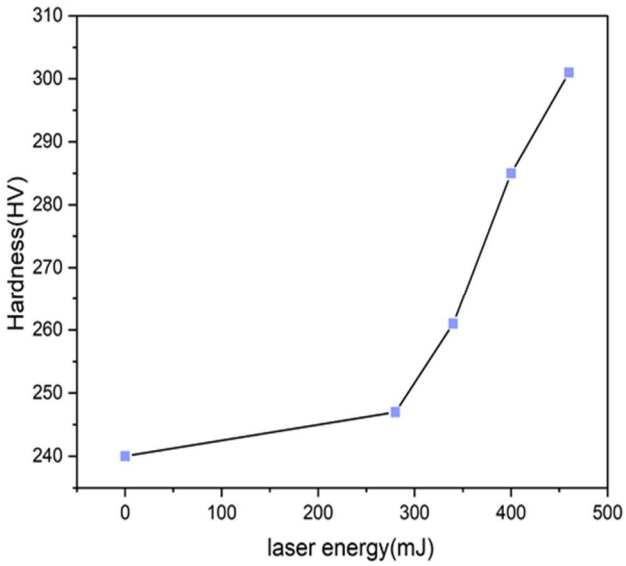

Fig. 5: Effect of laser energy on Vickers microhardness of Ti6Al4V alloy. Hardness increases with laser energy, reflecting grain refinement, higher dislocation density, and residual stresses from rapid surface melting and solidification.

3.4. Scanning Electron Microscope (SEM)

A scanning electron microscope (SEM) image of the untreated sample of Ti6A4V alloy shows a relatively smooth and homogeneous surface with fine, directional scratches resulting from mechanical preparation processes such as grinding and polishing. No signs of surface melting, re-solidification or thermal damage are observed, indicating that the surface remained in its original state and serves as a reference condition for comparison, as shown in Fig.6.

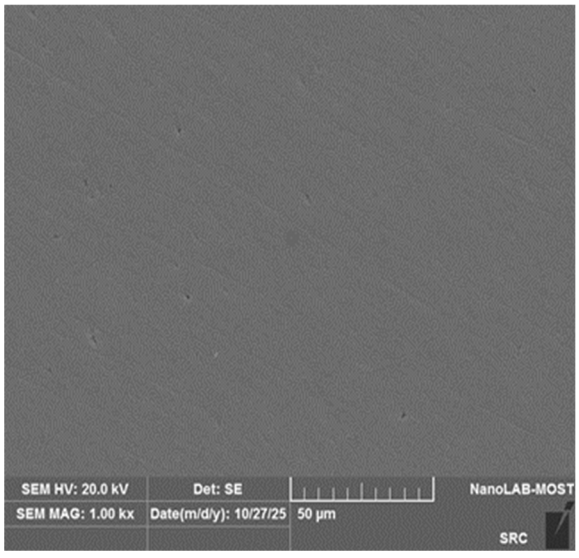

Fig. 6: SEM image showing the as-received Ti6Al4V surface with smooth morphology and minimal topographical features before laser treatment.

After laser treatment at energy of 280 mJ, initial surface modification becomes evident. The surface exhibits slight melting features and shallow surface ripples, accompanied by a modest increase in surface roughness. These changes suggest partial surface melting without inducing severe thermal effects. At laser energy of 340 mJ, the surface morphology shows more pronounced modification. The density of surface ripples and grooves increases, and the melted regions appear more uniform. This behavior is attributed to enhanced laser–material interaction, leading to more effective melting and rapid re solidification of the surface layer. When the laser energy is increased to 400 mJ, the surface undergoes significant modification, characterized by deeper grooves and a rougher surface texture. The microstructural features become more distinct due to higher thermal input, resulting in intensified melting and faster cooling rates, which promote noticeable surface restructuring. At the highest applied laser energy of 460 mJ, the surface exhibits the most severe modification, with dense and deep ripples, increased surface roughness, and signs of localized thermal stress. These features indicate excessive energy input, which enhances surface deformation and may introduce local non-uniformity due to rapid heating and cooling.

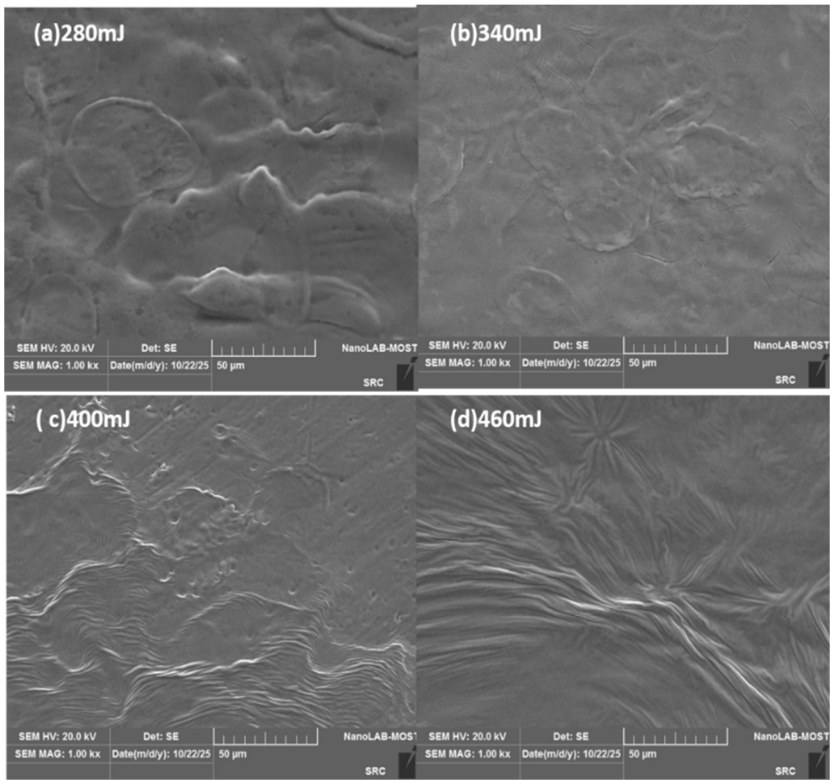

Fig. 7: SEM images of Ti6Al4V surfaces treated with increasing laser energies. Progressive surface modification is observed, from slight melting and shallow ripples at 280 mJ to dense, deep ripples and higher roughness at 460 mJ, indicating the effect of laser energy on surface morphology and microstructural restructuring.

4. Conclusion

Laser surface modification (LSM) of Ti6Al4V alloy significantly alters its surface properties. Increasing the laser energy within the tested range led to enhanced surface wettability, as indicated by a decrease in water contact angle and a corresponding increase in surface roughness. Additionally, microhardness measurements showed a gradual increase in surface hardness with increasing laser energy, which can be attributed to grain refinement and higher dislocation density resulting from rapid surface melting and

solidification. These results demonstrate the potential of LSM to modify surface characteristics; however, further studies are required to evaluate biological performance and corrosion behavior.

References

[1] O. Bialas, A. Kunwar, A. Taratuta, M. Skonieczna, K. Matus, and M. Adamiak, "Surface Engineering of Ti13Zr13Nb Biomaterial Alloy with Gold Via Laser Melting for Enhanced Biocompatibility and Functional Performance," *Metallurgical and Materials Transactions A*, 1–17 (2025).
[2] M. Balazic, J. Kopac, M. J. Jackson, and W. Ahmed, "Titanium and titanium alloy applications in medicine," *International Journal of Nano and Biomaterials*, 1 (1), 3–34 (2007).
[3] D. F. Williams, "On the nature of biomaterials," *Biomaterials*, 30 (30), 5897–5909 (2009).
[4] D. Mihov and B. Katerska, "SOME BIOCOMPATIBLE MATERIALS USED IN MEDICAL PRACTICE," *Trakia Journal of sciences*, 8 (2010).
[5] D. F. Williams, "On the mechanisms of biocompatibility," *Biomaterials*, 29 (20), 2941–2953(2008).
[6] H. Y. Hammod and T. J. Mossa, "Influence of optical fiber diameters on the performance of surface plasmon resonance sensor," *Baghdad Science Journal*, 19 (6), 34 (2022).
[7] D. M. Brunette, P. Tengvall, M. Textor, and P. Thomsen, *Titanium in medicine: material science, surface science, engineering, biological responses and medical applications*. Springer, (2001).
[8] H. J. Ali, M. K. Khalaf, B. M. Ahmed, and H. M. Fadhel, "Enhancing Ti6Al4V biomedical alloy's corrosion resistance with tin, TiO2, and TiO2/TiN multilayer coatings using DC reactive sputtering technique," in *AIP Conference Proceedings*, 3282 (1), 050024, (2025).
[9] N. H. Harb, "Preparation and characterization of NiONPS sensor Prepared by Different Q-switched Nd: YAG Laser parameter: energy pulse and wavelength," *Baghdad Science Journal*, 22 (2), (2025).
[10] K. Homa *et al.*, "Surface functionalization of titanium-based implants with a nanohydroxyapatite layer and its impact on osteoblasts: a systematic review," *Journal of Functional Biomaterials*, 15 (2), 45 (2024).
[11] Y. K. Balasubramanian Gayathri, R. L. Kumar, V. V. Ramalingam, G. S. Priyadharshini, K. S. Kumar, and T. R. Prabhu, "Additive manufacturing of Ti-6Al-4V alloy for biomedical applications," *Journal of Bio-and Tribo-Corrosion*, 8 (4), 98 (2022).
[12] E.-S. M. Sherif, S. A. Ragab, and H. S. Abdo, "Role of vanadium additions on the corrosion mitigation of Ti-6Al-xV alloy in simulated body fluid," *Metals*, 10 (7), 903 (2020).

تعديل سطح سبيكة Ti6Al4V بواسطة ليزرQ-switched Nd:YAG

فاطمة فلاح حسن[1] , حيدر يحيى حمود[1]*,محمد خماس خلف[2]

[1]قسم الفيزياء، كلية العلوم للبنات، جامعة بغداد، العرا ق

[2]هيئة البحث العلمي، بغداد،العراق

البريد الالكتروني للباحث: dr.hayder.y.phy@gmail.com

الخلاصة : اجري في هذه الدراسة تعريض سبيكةTi6Al4V الى ليزر Q-switched Nd:YAG (ذو الطول الموجي 1.064 نانومتر,معدل تكرار 6 هرتز ,عرض النبضة 10 نانوثانية,وحجم البقعة 4 مم) مع طاقات تتراوح بين (280-460) مللي جول . ويشار الى هذه العملية بأسم تعديل السطح بالليزر(LSM) .تم تقييم تأثير طاقة الليزر على البنية البلورية وقابلية التبلل السطحي والصلابة والتضاريس بشكل منهجي وباستخدام تقنيات القياس المناسبة مثل (XRD , زاوية الميل,اختبار الصلادة الدقيقة فيكرز, SEM) .وقد لوحظ زيادة كبيرة في الصلابة وقابلية البلل اثناء انخفاض زاوية الميل بالاضافة الى تحسن في خصائص السطح الاخرى.

IJL, Vol. 25, Issue 1, 2026
http://doi.org/10.31900/ijl.v25i1.563

Research Article

IRAQI JOURNAL OF LASER

Laser Direct Energy Deposition of Stainless Steel 316L: Investigation of Processing Parameters on Porosity and Microstructural Evolution

Samir Noori Ali[1,*], Ziad Aeyad Taha[1], Barbara Previtali[2]

[1]*Institute of Laser for Postgraduate Studies, University of Baghdad, Baghdad, Iraq*
[2]*Department of Mechanical Engineering, Politecnico di Milano, Via La Masa 1, 20156 Milan, Italy*
**Email address of the Corresponding author: samirnoori@ilps.uobaghdad.edu.iq*

Article history: Received 21 Jan. 2026, Accepted 6 Mar. 2026, Published online 15 Jun. 2026

Abstract: Laser direct energy deposition (LDED) was employed to fabricate low-carbon stainless steel 316L and to evaluate the influence of processing parameters on porosity, relative density, and microhardness. A fiber laser system operating at 1070 nm (YLS-3000-CUT, IPG ABB) was used. The spot size was 1.2 mm, the powder feed rate was 9.5 g/min, the layer thickness was 0.2 mm, the carrier gas flow rate was 7.5 L/min, and the shielding gas flow rate was 25 L/min. Laser power (420, 600, and 800 W) and scan speed (20, 25, and 30 mm/s) were systematically varied, producing nine samples with linear energy densities between 14 and 40 J/mm and volumetric energy densities from 59 to 167 J/mm³. Microstructural features and pore morphology were examined using optical microscopy and scanning electron microscopy. Porosity and relative density were quantified by full cross-sectional image analysis. Microhardness was measured using a Vickers indenter with a 300 g load and 10 s dwell time. Microhardness values ranged from 185.4 to 207.3 HV. Porosity values varied between 0.198% and 0.831%, while relative density ranged from 99.169% to 99.802%. Lower volumetric energy densities produced reduced porosity and increased relative density at all scan speeds. The minimum porosity (0.198%) and maximum relative density (99.802%) were obtained at a scan speed of 30 mm/s and a volumetric energy density of 59 J/mm³. The results quantify the effect of laser power and scan speed on densification and mechanical response in LDED-processed 316L and define a limited processing window for defect minimization.

Keywords: Laser direct energy deposition**,** Energy density**,** Scan speed.

1. Introduction

Laser direct energy deposition (LDED) is an additive manufacturing technique used to fabricate complex three-dimensional metallic components with reduced material waste and high deposition flexibility [1]. In LDED, metallic powder or wire feedstock is injected into a focused laser beam, where it melts and is deposited onto a substrate in a layer-by-layer manner [2]. This process enables near-net-shape manufacturing and repair of high-value components that are difficult or impractical to produce using conventional machining routes. Despite these advantages, the adoption of LDED for safety-critical applications remains limited due to the formation of process-induced defects, particularly porosity [3]. Porosity in LDED arises from multiple mechanisms, including gas entrapment within the melt pool, lack-

of-fusion between adjacent tracks or layers, keyhole instability, and pre-existing pores in atomized powder feedstock [4]. Even at low volume fractions, such defects can significantly degrade mechanical performance, especially tensile strength, ductility, and fatigue resistance [5]. The severity of these effects depends strongly on pore morphology and spatial distribution. Irregular lack-of-fusion pores generally exert a more detrimental influence on mechanical properties than spherical gas pores of comparable size, highlighting the need to control both pore formation mechanisms and their evolution during deposition [6].

Austenitic stainless steel 316L is widely used in marine, chemical, and biomedical applications due to its corrosion resistance, moderate strength, and excellent weldability [7]. In LDED processing, material quality is strongly governed by energy input, commonly expressed as energy density. Laser power and scan speed directly regulate the thermal energy delivered per unit length, thereby influencing melt pool geometry, cooling rate, solidification behavior, and defect formation [8]. Insufficient energy input leads to incomplete fusion and lack-of-fusion porosity, whereas excessive energy input promotes keyhole formation and subsequent gas entrapment during collapse [9]. Achieving full densification therefore requires a balanced processing window that enables adequate fusion while minimizing excessive vaporization and instability [10].

Although prior studies have demonstrated the sensitivity of porosity to processing parameters, the combined and systematic effects of laser power and scan speed on porosity characteristics, microstructural evolution, relative density, and mechanical response remain insufficiently resolved, particularly for 316L fabricated by LDED [11]. In addition, many investigations report microstructural observations without directly linking them to quantified porosity levels and local mechanical properties. This limits the ability to establish reliable process–structure–property relationships.

Microstructural characterization using optical microscopy and scanning electron microscopy provides essential insight into grain morphology, dendritic structure, phase distribution, and defect types formed during LDED [12]. Complementary microhardness measurements serve as a sensitive indicator of local microstructural variations and compositional inhomogeneity induced by thermal history. Together, these techniques enable correlation between processing conditions, microstructural features, and mechanical response at the microscale. Such correlations are necessary for defining processing windows suitable for defect minimization and performance consistency [13].

Several recent studies highlight both the potential and limitations of DED-based processing of stainless steels. Saboori et al. [14] emphasized that although DED enables fabrication of complex and functionally graded structures, incomplete understanding of microstructure evolution and defect formation continues to hinder industrial maturity. G. A. Barragán et al. [15] demonstrated that directed energy deposition (DED) can produce dense AISI 316L stainless steel deposits with strong metallurgical bonding and low porosity when appropriate processing conditions are employed. Their results confirmed that high cooling rates inherent to DED promote fine cellular and dendritic austenitic microstructures, which are closely associated with improved material integrity. Although their study focused on coating applications, it highlighted the importance of controlling process parameters to minimize porosity and preserve alloy chemistry during deposition.

H. Shi et al. [16] investigated the influence of additive manufacturing–induced microstructural features on the high-temperature behavior of laser metal deposited 316L stainless steel. Their work showed that phase segregation and δ-ferrite formation at grain boundaries are strongly linked to thermal history and energy input during deposition. These findings emphasize that process-controlled microstructural evolution plays a critical role in determining material performance, reinforcing the need for systematic parameter control in LDED. Zhou and Ning et al. [17] examined the effects of process parameters on porosity formation and microstructural refinement in DED-fabricated 316L-based systems. Their study demonstrated that variations in energy input significantly affect melt pool stability, grain morphology, and defect formation.

Increased energy density promoted grain refinement but also increased the likelihood of porosity and cracking when excessive thermal input led to melt pool instability. This highlights the narrow processing window required to balance densification and defect suppression.

Z. Ma et al. [18] reported that multiple DED process parameters simultaneously influence density, surface quality, and microstructural uniformity in stainless steel–based structures. Their statistical analysis showed that scan speed plays a dominant role in controlling surface integrity, while thermal input strongly affects densification behavior. These results underscore the necessity of isolating and quantifying the individual and combined effects of laser power and scan speed on relative density and defect formation.

Zürcher et al. [19] investigated the wear behavior of additively manufactured 316L stainless steel produced by the laser metal deposition (LMD) process, with a specific focus on its suitability for repair applications. The authors evaluated friction and wear under dry sliding conditions using a flat-on-flat configuration against AISI 52100 steel and compared LMD-fabricated 316L with conventionally rolled 316L. Microstructure, residual stresses, and hardness were characterized prior to tribological testing to support interpretation of wear mechanisms.

Despite these advances, a quantitative and systematic correlation between laser power, scan speed, porosity, relative density, microstructural characteristics, and microhardness in LDED-fabricated 316L stainless steel remains limited [20]. Experimental studies that directly link energy density regimes to both defect metrics and mechanical response under controlled conditions are scarce [21].

Accordingly, the present work focuses on systematically varying laser power and scan speed during LDED of 316L stainless steel to quantify their effects on porosity formation, relative density, microstructure, and microhardness. By combining optical microscopy, scanning electron microscopy, image-based porosity analysis, and microhardness testing, this study establishes evidence-based process–structure–property relationships consistent with the scope defined in the abstract.

2. Materials and Methods

This section outlines the materials used, the experimental setup employed for laser direct energy deposition, and the processing parameters selected to fabricate 316L stainless steel samples. It also describes the characterization techniques applied to evaluate the microstructural, mechanical, and porosity-related features of the deposited materials, along with the methodology used to quantify porosity and assess the quality of the fabricated parts.

2.1. Materials

Low-carbon austenitic stainless steel 316L powder was used as the feedstock material for laser direct energy deposition. The powder particle size ranged from 56 to 100 μm, which was made by the gas atomization manufacturing method, ensuring stable flowability and consistent interaction with the laser-induced melt pool, as shown in Fig. 1. Also, the volumetric distribution and volume transformation are shown in Figs. 2and 3 respectively. The chemical composition of SS316L powder was summarized in Table 1.

Table 1. Chemical composition of SS316L (Wt.%)

Fe%	C%	Cr%	Mn%	Mo%	P%	Si%	Ni%
Bal.	0.03	19.09	1.14	2.32	0.5	0.71	10.07

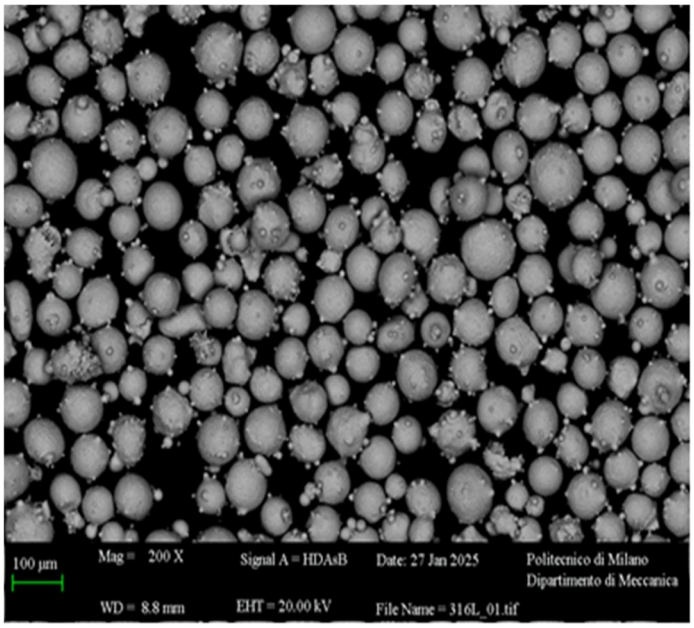

Fig. 1: SEM of SS316L powder

CE Diameter Report - Volume Distribution

Malvern

Measurement Details

Sample Name: 316L_PowderRange

SOP Name: S700sived.vsop

User Name: M4

Edited: False

Date: 19 December 2024 13:32:45

Edited On: 19 December 2024 13:32:45

Analysis

SOP Optic(s) used: 10x

SOP Foreground Segmentation Type[n]: Sharp Edge (General Purpose)

SOP Trash Size: 25

SOP Particle Separation: None

Result

CE Diameter Minimum (µm): 1.01

CE Diameter Maximum (µm): 126.84

CE Diameter D[4,3] (µm): 77.1

CE Diameter D[3,2](µm): 64.92

Particles Counted: 20000

CE Diameter D[v, 0.1]: 56.71

CE Diameter D[v, 0.5]: 76.31

CE Diameter D[v, 0.9]: 100.2

CE Diameter STDV (µm): 12.64

CE Diameter RSD (%): 187.02

Fig. 2: Volume distribution of SS316L

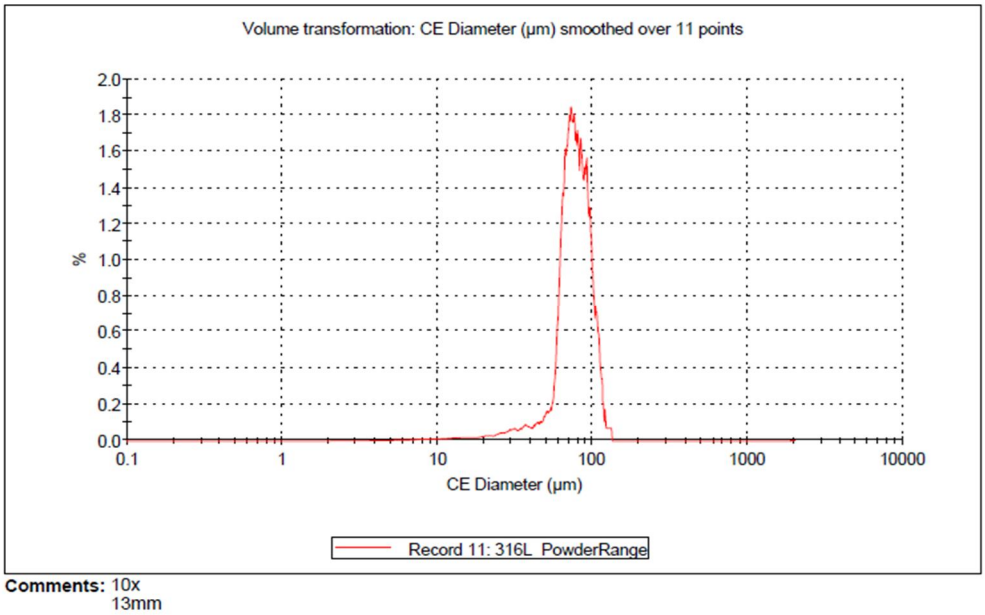

Fig. 3: Volume transformation of SS316L.

2.2 Experimental Setup

The laser direct energy deposition (LDED) process was carried out using a high-power fiber laser system (YLS-3000-CUT, IPG ABB) operating at a wavelength of 1070 nm with a Gaussian beam intensity distribution, as shown in *Fig. 4*. The system was integrated with an ABB industrial robotic arm coupled with a circular two-axis table, enabling precise multi-axis motion control and flexible deposition strategies. A coaxial powder delivery system transported SS316L powder from a hopper to the laser focal point using argon carrier gas at 7.5 L/min, while argon shielding gas at 25 L/min was supplied around the melt pool to minimize oxidation and atmospheric contamination during deposition.

Fig. 4: Ytterbium fiber laser and LDED printhead.

2.3. Process Parameters

A fixed laser spot size of 1.2 mm, layer thickness of 0.2 mm, powder feed rate of 9.5 g/min, overlap of 50%, and hatch spacing of 0.6 mm, which is typical for LDED processes and ensures sufficient melt pool overlap for good metallurgical bonding, while limiting excessive reheating, and standoff distance of 12 mm. All these characteristics were maintained throughout the experiments. The process parameters were systematically varied by adjusting laser power (420, 600, and 800 W) and scan speed (20, 25, and 30 mm/s), resulting in nine distinct deposition conditions. These parameter combinations produced linear energy densities ranging from 14 J/mm to 40 J/mm, allowing investigation of their influence on melt pool behavior, thermal gradients, solidification dynamics, and resulting microstructural and mechanical properties.

The basic relationship of material quality in LDED is the volumetric energy density (VED) in J/mm³, mathematically expressed as [22].

$$VED = \frac{P}{v\ t\ d} \quad (1)$$

where P laser power (W), v scan speed (mm/s), d spot diameter (mm), and t layer thickness (mm).

Nevertheless, for single-track depositions, the fixed spot size (1.2 mm) and layer thickness (0.2 mm) in each deposition track, the linear energy density, mathematically specified as [22],becomes the dominant parameter controlling melt pool characteristics.

$$El = \frac{P}{v} \quad (2)$$

2.4. Characterization Methods

The deposited samples, each with dimensions of 10 x 10 x 10 mm³, as shown in *Fig. 5*, were built by zigzag for cubes strategy. All samples were sectioned, mounted, polished, and prepared following standard metallographic procedures, as shown in Fig. 6. The metallographically prepared samples were chemically etched using an aqueous solution composed of hydrochloric acid (HCl), nitric acid (HNO_3), and distilled water mixed in a 1:1:1 volume ratio to reveal the microstructural features [23].

Optical microscopy (OM) and scanning electron microscopy (SEM) were employed to analyze microstructural features, grain morphology, phase distribution, and defect characteristics. To evaluate mechanical behavior, Vickers microhardness testing was performed using a load of 300 g and a dwell time of 10 s, enabling assessment of local property variations caused by microstructural evolution and porosity distribution, as shown in Fig. 7[24,25].
Hardness profiles were obtained along three vertical traverses across the cross-section (edge–center–edge) from the substrate interface to the top of the deposited height. A total of 150 independent indentations were conducted, consisting of 50 measurements along each traverse. A minimum center-to-center spacing of at least three times the indentation diagonal length was maintained between adjacent indents to avoid interaction effects, in accordance with ASTM E384. The hardness values obtained from each traverse were subsequently averaged, and the mean values were used for plotting and comparative analysis, as shown in Fig. 8.

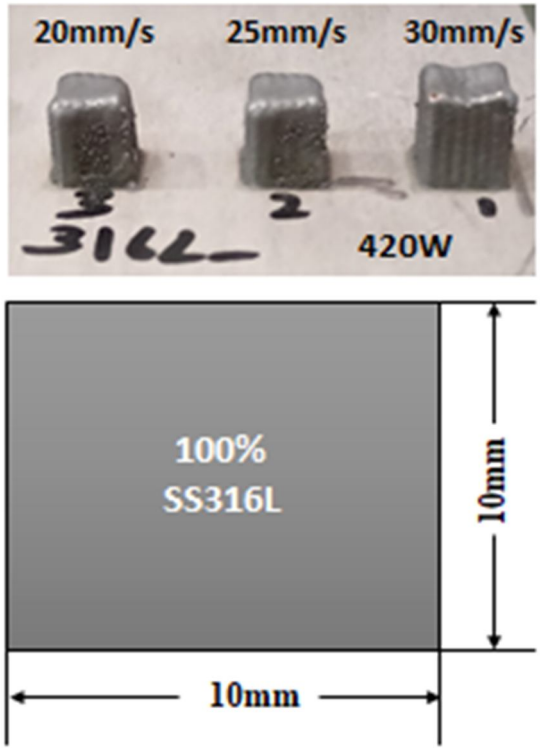

Fig. 5: dimensions of SS316L samples.

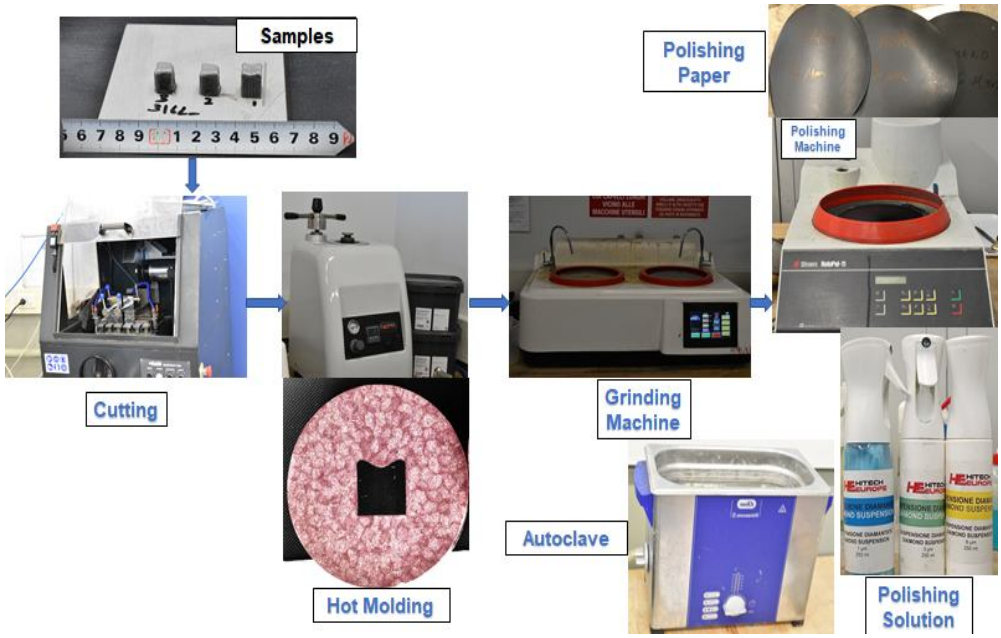

Fig. 6: Sample preparation procedure.

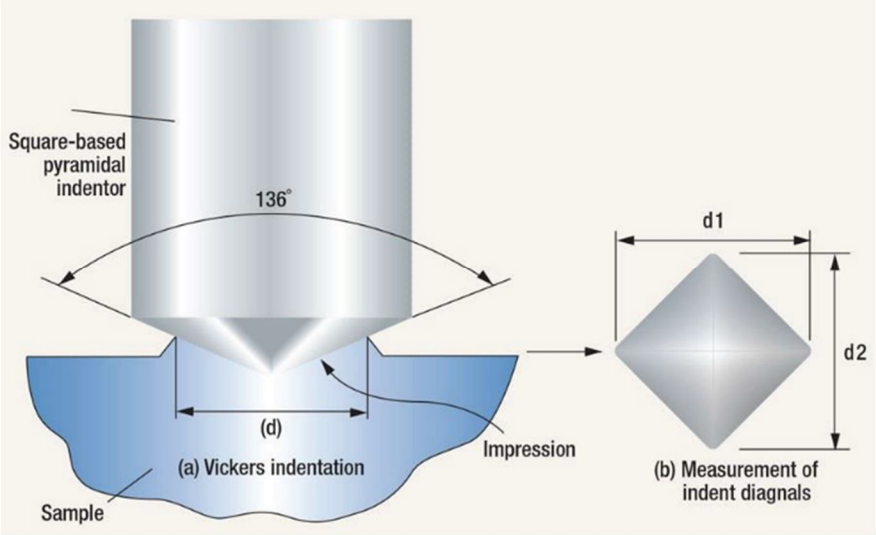

Fig. 7: Principal of Hardness Vickers Calculation [24].

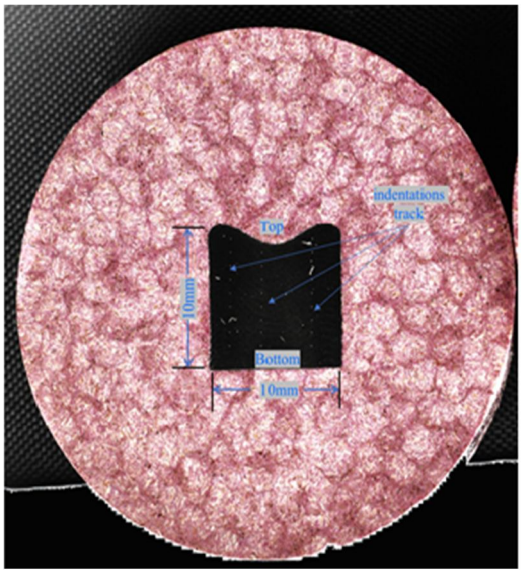

Fig. 8: Microhardness profiles measured along the build height of SS316L.

2.5. Porosity Quantification Methodology

Porosity and relative density were quantified using high-resolution optical images captured across the full cross-sectional area of each specimen with a Mitutoyo Quick Vision optical measurement system. Quantitative porosity analysis was performed using ImageJ software. Optical micrographs acquired from polished and etched cross-sections were used for analysis. For each sample, multiple images were captured at identical magnification from representative regions across the deposited area to ensure statistical reliability. The images were first converted to grayscale and subjected to contrast enhancement to improve pore–matrix differentiation. A global thresholding method was applied to segment pores from the metallic matrix, followed by manual verification to remove artifacts and non-relevant features.

Porosity was quantified by calculating the ratio of the total pore area to the total analyzed area. The reported porosity values represent the average of all analyzed images for each processing condition.

3. Results and discussion

3.1. Porosity and Relative Density

At the lab, the experimental results showed that the linear energy density controls are essential to the optimum densification and the lowest porosity of laser-directed energy deposited samples. Importantly, we report that samples fabricated at the lowest energy densities (such as 420 W and higher scan speeds of 25 and 30 mm/s) resulted in the highest comparative density and least porosity, demonstrating stable melt pool dynamics, complete powder fusion, and suppressed overheating-induced defects. The thermal energy overabundance on samples had negatively impacted the porosity of different melt parameters [26], as such, we compared the results with those produced under high energy densities (higher power, lower scan-speed values), confirming that the increase of thermal energy caused the melt pool to destabilize, with attendant pore formation through keyhole instability and other mechanisms. Accordingly, this experiment proves from a systemic perspective that exact moderation of energy input is vital, and that the best structural, mechanical properties and build quality can only be obtained if the lowest linear energy densities are applied to the parameter matrix under consideration.

Analysis of the nine samples (see Figs. 9 and 10) reveals a strong relationship between linear energy density and porosity and the relative density of the laser-deposited structures. The samples have the lowest porosity and highest relative density at minimized energy densities using lower laser power and increased scan speed, indicating that the melt pool stability and efficient fusion without causing the melt to overheat. For instance, the sample processed at 420 W and 30 mm/s yielded the lowest porosity (0.198%) and the highest relative density (99.802%).

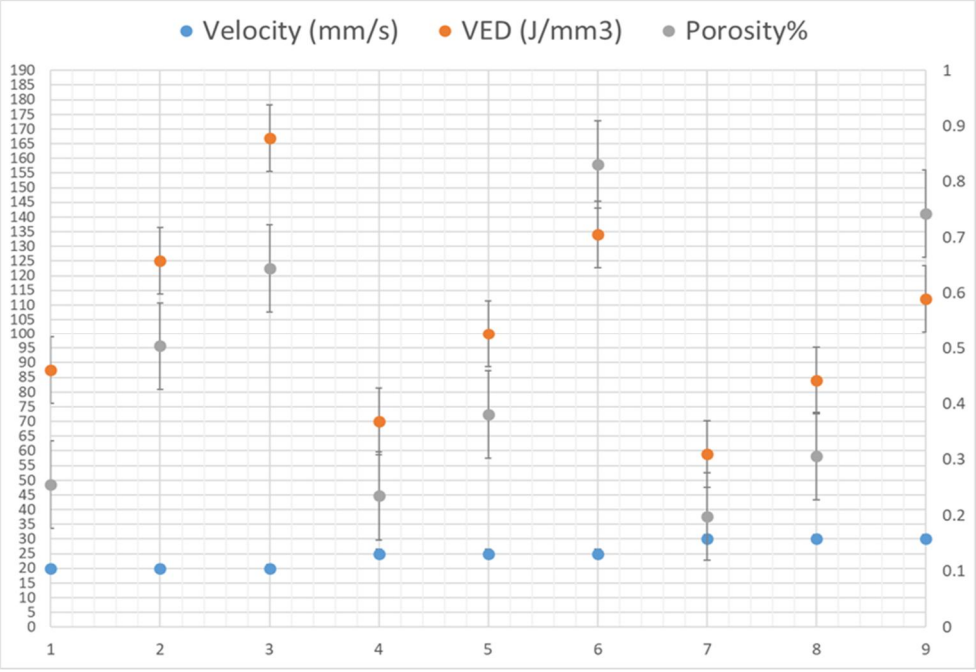

Fig. 9: Relationship between v, VED, and porosity

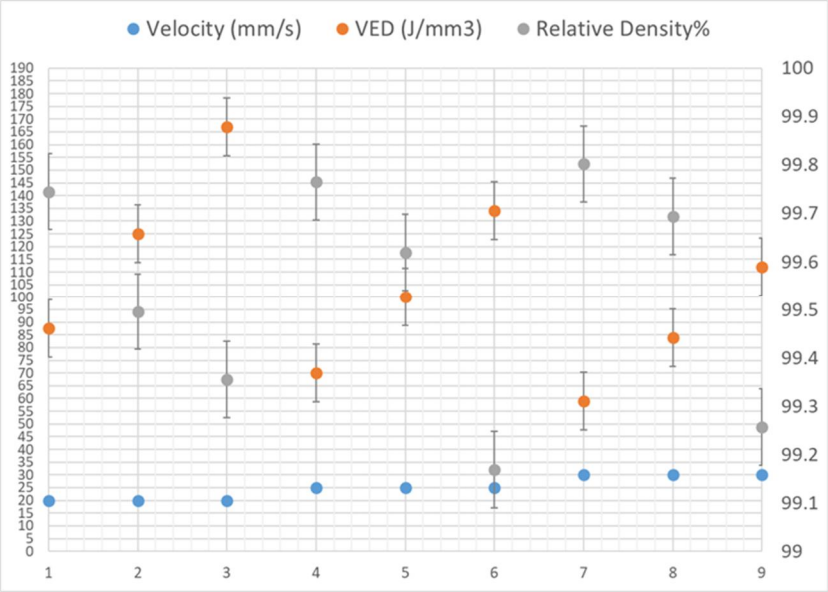

Fig. 10: Relationship between ν, VED, and RD.

3.2. Microstructure Analysis

The microstructural evolution observed by OM and SEM can be understood as a continuous response to increasing energy per unit length (E_l) and the attendant changes in melt-pool geometry and local cooling rate: the lowest E_l runs (420 W at 30 mm/s, $E_l \approx 14$ J/mm as shown in Fig. 11) produce narrow, shallow, regularly stacked melt pools with only tiny, isolated spherical pores visible in OM and, in SEM, the finest cellular solidification substructure with extremely primary spacings, minimal interdendritic segregation, and only sparse, discontinuous carbide/oxide inclusions.

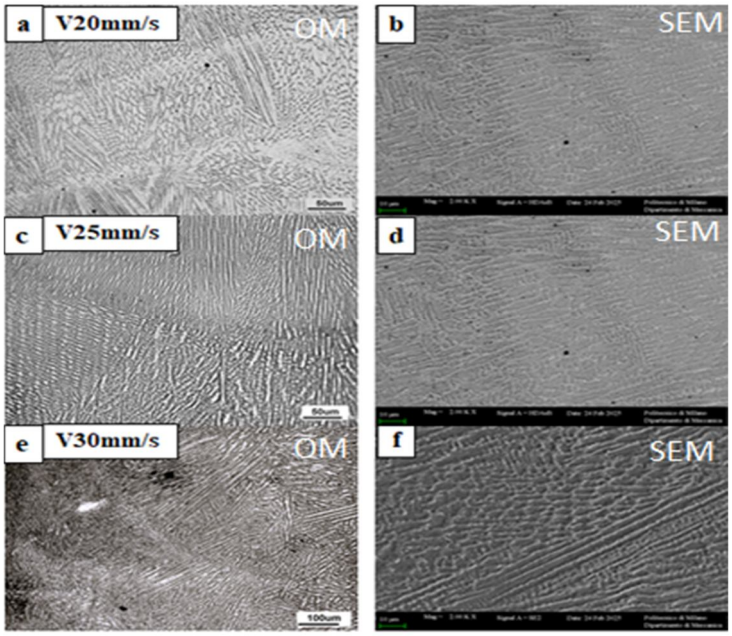

Fig. 11: OM and SEM of SS316L, ν of 20, 25, and 30 mm/s at a P of 420 W

Considerably higher E_l at 420 W (Fig. 11) but slower speeds (25 mm/s and 20 mm/s; $E_l \approx 16.8$ and 21 J/mm) still show well-defined melt-pool bands in OM but progressively wider pools and a small increase in visible pore frequency, while SEM reveals a modest coarsening of cellular/dendritic spacing and a slightly greater tendency for solute and inclusion accumulation at cell walls.

Increasing power to 600 W (Fig. 12) at 30, 25, and 20 mm/s ($E_l \approx 20$, 24, and 30 J/mm) produces wider and deeper melt pools with more frequent small porosity and more irregular overlap footprints in OM; at the SEM scale these conditions exhibit coarser cellular/dendritic arrays, clearer enrichment of alloying elements and inclusion/precipitate contrast at interdendritic locations (manifested in SS316L as more pronounced cell-wall segregation and a likely presence of fine M23C6-type carbide or oxide clustering at boundaries), and a higher incidence of irregular porosity associated with partial keyholing or entrapment during slower solidification [27,28].

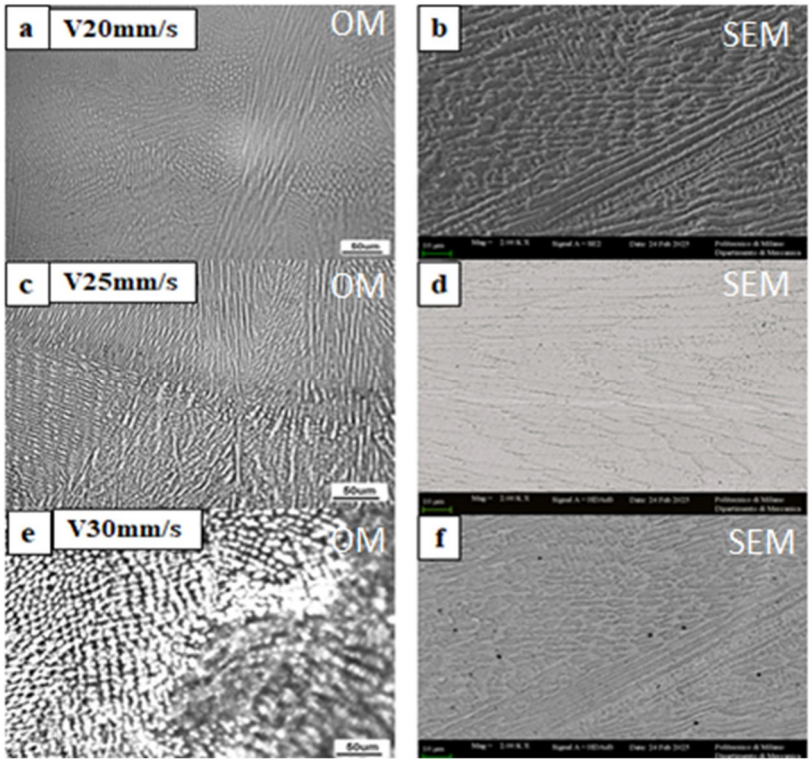

Fig. 12: OM and SEM of SS316L, ν of 20, 25, and 30 mm/s at a P of 600 W

At the highest power, 800 W (Fig. 13) with the three speeds ($E_l \approx 27$, 32, and 40 J/mm), OM shows the broadest, deepest, and most irregular melt pools with the greatest density of both spherical and irregular voids and disturbed overlaps, while SEM reveals markedly coarsened dendritic structures, extensive interdendritic films of segregated solute, and larger inclusion/precipitate particles and networks at grain boundaries; these microstructural features reflect long liquid lifetimes that enable solute partitioning, carbide/oxide precipitation, and coarsening and increase the probability of gas/vapor-induced porosity and lack-of-fusion defects from keyholing [29,30].

As shown in Figs. 11, 12 and 13, all conditions exhibit cellular-to-cellular dendritic solidification morphologies; increasing laser power enhances melt pool boundary features and pore visibility, while increasing scan speed refines the cellular structure but increases microstructural heterogeneity when remelting becomes marginal.

Mechanistically, the superior appearance and highest relative density measured in the 420 W / 30 mm/s condition arise because the low E_l yields the fastest local cooling rates and steep thermal gradients: Rapid solidification reduces primary arm spacing, suppresses diffusion-controlled precipitation and solute segregation, and shortens the time window for gas entrapment and keyhole instability, producing a uniformly fine austenitic matrix with only very fine, discontinuous carbides or oxides and very few pores; conversely, higher E_l raises melt temperatures and liquid lifetime, coarsens the microstructure, promotes interdendritic segregation and carbide/oxide nucleation, and increases porosity, all of which are evident in the graded progression of OM and SEM features across the nine samples [31].

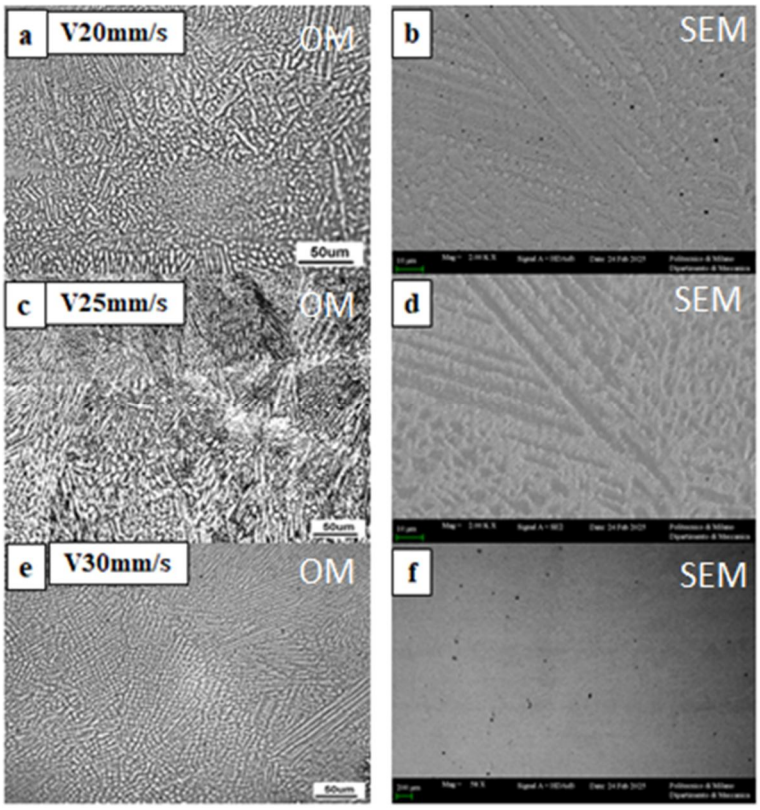

Fig. 13: OM and SEM of SS316L, v of 20, 25, and 30 mm/s at a P of 800 W

3.3. Mechanical Performance through Microhardness Measurement

In this study nine samples of 100% SS316L manufactured by LDED have been examined. The specimens show a very clear, quantitatively strong inverse dependence of Vickers microhardness (as shown in Fig. 14) on the linear energy density across the tested window: samples with the highest E_l (≈40 J/mm at 800 W, 20 mm/s) record the lowest hardness (~185 HV), and those with the lowest E_l (≈14 J/mm at 420 W, 30 mm/s) record the highest hardness (~207 HV). This indication confirms that increasing scan speed (higher v) or reducing power (lower P) raises hardness primarily because both reduce E_l. This behavior is consistent with the laser-AM physics: the cooling rate in the melt/solidification zone scales roughly with scan velocity and inversely with absorbed power (cooling $\propto$ v / P), so higher v or lower P produces faster cooling, finer solidification structures (smaller cellular/dendritic arm spacing or effective grain size), and therefore higher strength/hardness via Hall–Petch–type effects; conversely, high E_l produces larger melt pools, slower cooling, and coarser structures with lower hardness [32, 33]. Directed-energy-deposition (DED) work on AISI 316L shows the same processing physics but also demonstrates that local factors such as lattice micro-strain and subtle phase/δ-ferrite variations can modulate local hardness (so micro-

strain/residual stress may either reinforce or partially offset the grain-size effect in specific regions) [34]. Practically, this means that hardness rising as E_l decreases from 40 to 14 J/mm is physically robust and predictable but must be balanced against manufacturing defects: The AM literature also documents that very low energy input (below the material/process-specific threshold) causes unstable melt pools and lack-of-fusion porosity, while overly high energy can produce balling or gas entrapment, so there is an optimal E_l window for good density and the desired mechanical property set [35]. The behavior and quantitative sensitivity fall within published ranges for additively manufactured SS316L and match the theoretical and experimental analyses linking hardness to cooling rate and energy input in laser additive processes.

Any increase in porosity amount (Fig. 15), that is led to decrease in hardness due to localized plastic strain accommodation around voids. Conversely, relative density (which is inversely proportional to porosity as shown in Fig. 16) correlates positively with hardness because a denser material exhibits greater resistance to indentation.

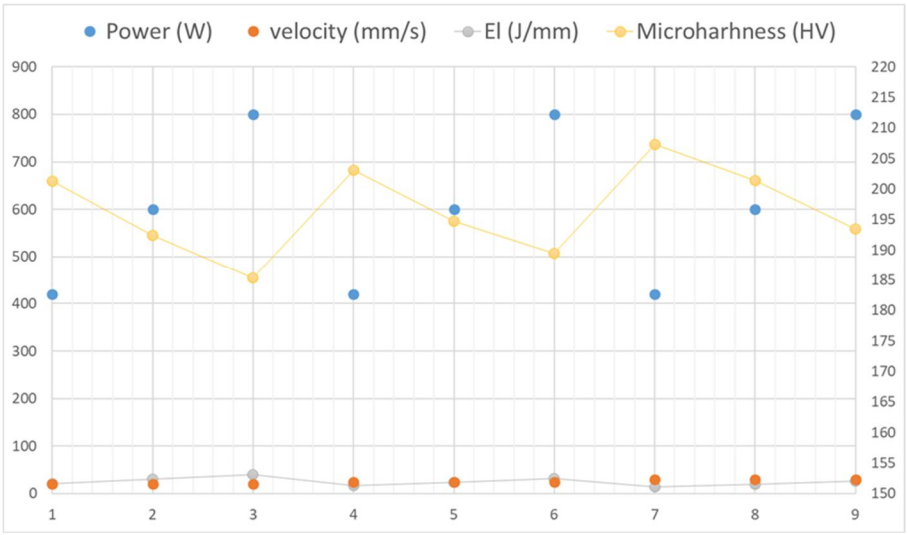

Fig. 14: Relationship between P, v, E_l, and microhardness.

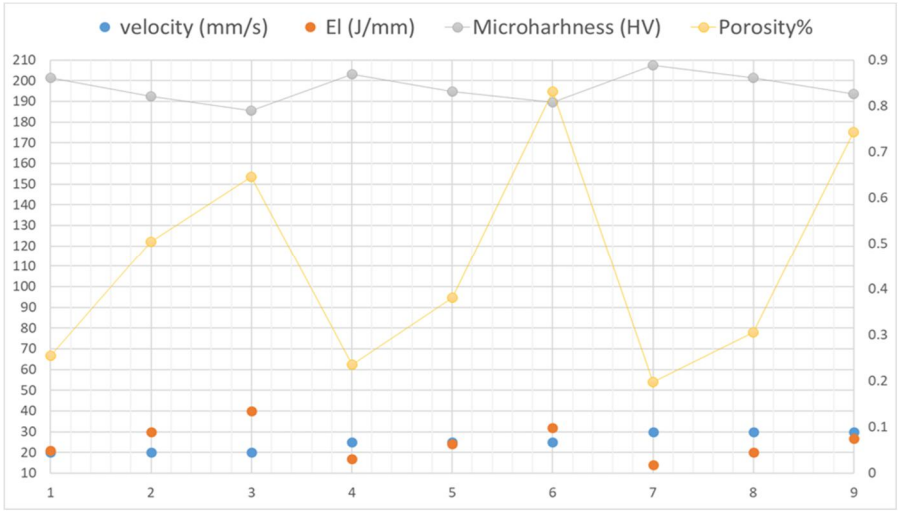

Fig. 15: Relationship between v, E_l, microhardness, and porosity.

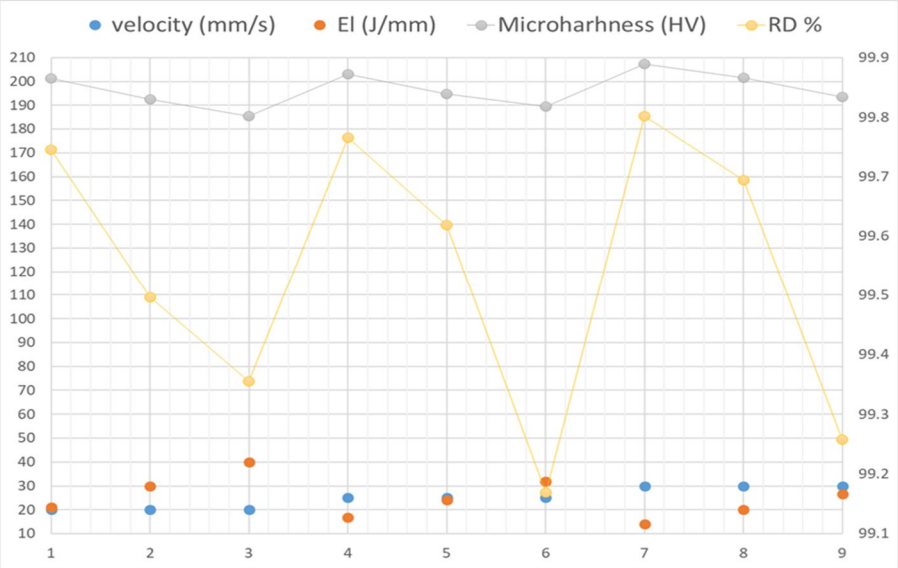

Fig. 16: Relationship between ν, E_l, microhardness, and RD%.

4. Conclusion

This study systematically quantified the effects of laser power and scan speed on porosity formation, relative density, microstructural evolution, and microhardness in SS316L fabricated by laser direct energy deposition.

1- Within the investigated parameter window, porosity ranged from 0.198% to 0.831%, while relative density varied between 99.169% and 99.802%. The lowest porosity (0.198%) and highest relative density (99.802%) were obtained at a scan speed of 30 mm/s and a volumetric energy density of 59 J/mm^3, indicating that reduced energy input promotes stable melt pool behavior and effective densification under the present conditions.

2- Optical and scanning electron microscopy revealed that all samples exhibited cellular-to-cellular dendritic austenitic solidification morphologies. Decreasing linear energy density resulted in finer cellular structures, reduced interdendritic segregation, and fewer observable defects, whereas increasing energy density led to coarsened dendritic features, enhanced solute segregation, and a higher incidence of both spherical and irregular pores. These microstructural trends are consistent with variations in melt pool lifetime and local cooling rate induced by changes in laser power and scan speed.

3- Vickers microhardness values ranged from 185.4 to 207.3 HV and showed a clear inverse relationship with linear energy density. Higher scan speeds and lower laser powers produced higher hardness values, which correlate with microstructural refinement associated with faster cooling rates. The measured hardness variations are consistent with grain and cellular spacing refinement rather than changes in phase constitution.

4- Overall, the results demonstrate that laser power and scan speed exert a coupled and quantifiable influence on densification, microstructure, and microhardness in LDED-processed SS316L. The findings define a limited processing window in which porosity is minimized and microstructural refinement is maximized under the fixed conditions employed in this study. These conclusions are restricted to the investigated parameter range and characterization methods and provide an experimental basis for further targeted optimization studies.

Acknowledgment

This work was supported by SITEC-Laboratory for Laser Applications, Department of Mechanical Engineering/ Politecnico di Milano, Italy, with special thanks to Akshay Ashok Benni.

References

[1] S. S. Dash, Z. Liu, L. Lang, T. Lyu, D. Chen, and Y. Zou, “Laser-based direct energy deposition of compositionally graded titanium alloys: Microstructural evolution, hardness, and tensile properties”, J. Alloys and Compounds, 1020, 179335 (2025). doi: 10.1016/j.jallcom.2025.179335
[2] B. Guan, L. Qin, G. Yang, Y. Ren, and X. Wang, “Laser Polishing of Directed Energy Deposition Metal Parts: A Review”, Additive Manufacturing Frontiers, 3, 200174 (2024). doi: 10.1016/j.amf.2024.200174
[3] Y. Chu, X. Zhao, W. Sun, S. Holdsworth, D. Guan, and Y. Huang, “Laser directed energy deposition additive manufacturing using friction stir channelling extruded wire”, Advanced Powder Materials, 2, 100137 (2023). doi: 10.1016/j.jmapro.2025.09.060
[4] T. Zhao, Y. Wang, T. Xu, M. Bakir, W. Cai, M. Wang, M. Dahmen, Q. Zheng, X. Wei, C. Hong, C. Zhong, P. Albus, T. Schopphoven, A. Gasser, and C. L. Häfner, "Some factors affecting porosity in directed energy deposition of AlMgScZr-alloys", Optics & Laser Technology, 143, 107337 (2021). doi: 10.1016/j.optlastec.2021.107337
[5] P. Liu, K. Yi, I. Jeon, and H. Sohn, "Porosity inspection in directed energy deposition additive manufacturing based on transient thermoreflectance measurement", NDT&E International, 122, 102491 (2021). doi: 10.1016/j.ndteint.2021.102491
[6] W. Liu, Y. Li, C. Yao, D. Zhang, D. Sun, S. Chen, Y. Wu, J. Wang, L. Lu, S.-N. Luo, Y. Tao, and B. Zhang, "Revealing mechanism of pore defect formation in laser directed energy deposition of aluminum alloy via in-situ synchrotron X-ray imaging", Condensed Matter Materials Science, 10702 (2024). doi: 10.48550/arXiv.2404.06853
[7] R. Guzmán-Nogales, F. Estupiñán-López, C. Gaona-Tiburcio, O. E. Lopez-Botello, J. G. Ramírez-Rodríguez, and P. C. Zambrano-Robledo, “Corrosion Resistance Measurement of 316L Stainless Steel Manufactured by Selective Laser Melting,” Materials, 14, 4509 (2021). doi: 10.3390/ma14164509
[8] T. E. Abioye, J. Folkes, and A. T. Clare, "A parametric study of Inconel 625 wire laser deposition", J. Materials Processing Technology, 213, 2145-2151 (2013). doi: 10.1016/j.jmatprotec.2013.06.007
[9] N. Ahmed, I. Barsoum, G. Haidemenopoulos, and R. K. Abu Al-Rub, "Process parameter selection and optimization of laser powder bed fusion for 316L stainless steel: A review", J. Manufacturing Processes, 75, 415-434 (2022). doi: 10.1016/j.jmapro.2021.12.064
[10] C. Gianassi, E. Liverani, A. Cavagnino, L. Zarri, A. Ascari, Y. Cui, and A. Fortunato, "Laser directed energy deposition of FeSi/SS 316L advanced bimetallic high-speed rotors: From material characterization to performance evaluation", Advances in Industrial and Manufacturing Engineering, 11, 100175 (2025). doi: 10.1016/j.aime.2025.100175
[11] J. T. Pacheco, V. H. Meura, P. R. A. Bloemer, M. T. Veiga, O. C. de Moura Filho, A. Cunha, and M. F. Teixeira, "Laser directed energy deposition of AISI 316L stainless steel: The effect of build direction on mechanical properties in as-built and heat-treated conditions", Advances in Industrial and Manufacturing Engineering, 4, 100079 (2022). doi: 10.1016/j.aime.2022.100079
[12] Y. Y. Su, Z. F. Wang, J. C. Xie, G. Xu, F. Xing, K. Y. Luo, and J. Z. Lu, "Microstructures and mechanical properties of laser melting deposited Ti6Al4V/316L functional gradient materials", Materials Science & Engineering A, 817, 141355 (2021). doi: 10.1016/j.msea.2021.141355
[13] N. Sargent, Y. Wang, D. Li, Y. Zhao, X. Wang, and W. Xiong, "Exploring Alloy Design Pathway Through Directed Energy Deposition of Powder Mixtures: A Study of Stainless Steel 316L and Inconel 718", Additive Manufacturing Letters, 6, 100133 (2023). doi: 10.1016/j.addlet.2023.100133
[14] A. Saboori, A. Aversa, G. Marchese, S. Biamino, M. Lombardi, and P. Fino, "Microstructure and Mechanical Properties of AISI 316L Produced by Directed Energy Deposition-Based Additive Manufacturing: A Review", Applied Sciences, 10, 3310 (2020). doi: 10.3390/app10093310
[15] G. A. Barragan, F. Mariani, and R. T. Coelho, "Application of 316L stainless steel coating by Directed Energy Deposition process", IOP Conference Series: Materials Science and Engineering, 1154, 012014 (2021). doi: 10.1088/1757-899X/1154/1/012014
[16] H. Shi, T. Wu, Q. Gong, W. Ding, Y. Chai, A. Weisenburger, L. Chang, Z. Zhang, K. Wang, J. Richter, T. Niendorf, and G. Müller, "Hot corrosion behavior of additively manufactured stainless steel 316L and Inconel 718 in MgCl2/KCl/NaCl chloride salts at 700 °C", Corrosion Science, 207, 110561 (2022). doi: 10.1016/j.corsci.2022.110561

[17] Y. Zhou and F. Ning, "Directed Energy Deposition of SS 316L/SiC Composites Using Coincident and Coaxial Wire-Powder Feeding", Procedia Manufacturing, 35, 557-563 (2023). doi: 10.1016/j.mfglet.2023.08.027
[18] Z. Ma, W. Liu, W. Li, H. Liu, Z. Lv, J. Song, Y. Huang, B. Liu, Y. Liu, and Y. Zhang, "Optimization of density and surface morphology of SS 316L/IN718 functionally graded thin-walled structures using hybrid prediction-multi-objective optimization method", J. Manufacturing Processes, 120, 337-352 (2024). doi: 10.1016/j.jmapro.2024.04.044
[19] T. Zurcher, E. Charkaluk, and V. Fridrici, "Wear behavior of 316L stainless steel obtained by additive manufacturing (laser metal deposition process)", Wear, 570, 205948 (2025). doi: 10.1016/j.wear.2025.205948
[20] A. Whitt, R. Seede, J. Ye, M. Elverud, M. Vaughan, A. Elwany, R. Arroyave, and I. Karaman, "A Process Optimization Framework for Laser Direct Energy Deposition: Densification, Microstructure, and Mechanical Properties of an Fe-Cr Alloy", J. Manufacturing Processes, 101, 114 (2022). doi: 10.1016/j.jmapro.2022.11.028
[21] W. Xiong, “Additive manufacturing as a tool for high-throughput experimentation”, J Mater Inf, 2:12 (2022). doi: 10.20517/jmi.2022.19
[22] G. Gong, J. Ye, Y. Chi, Z. Zhao, Z. Wang, G. Xia, X. Du, H. Tian, H. Yu, and C. Chen, "Research status of laser additive manufacturing for metal: a review", J. Materials Research and Technology, 15, 855-884 (2021). doi: 10.1016/j.jmrt.2021.08.050
[23] R. Nagar, R. Singh, N. Patil, and I. Yadav, “Comparison of electrolytic etching and immersion etching for 304L, 316L and 347 austenitic stainless-steel grades”, J. Materials Research and Technology (2024). doi: 10.1515/pm-2024-0032
[24] S. K. Gürel, İ. A. Yüksel, and T. O. Kılınç, “Uncertainty calculations and calibration of metal hardness testing equipment”,19th International Congress of Metrology, 12002 (2019). doi: 10.1051/metrology/201912002
[25] J. Dar, A. G. Ponsot, C. J. Jolma, and D. Lin, "A review on scan strategies in laser-based metal additive manufacturing", J. Materials Research and Technology, 36, 5425-5467 (2025). doi: 10.1016/j.jmrt. (2025).04.068
[26] H. Park, K. M. Mullin, V. Kumar, O. Wander, T. M. Pollock, and Y. Zhu, "Resolving thermal gradients and solidification velocities during laser melting of a refractory alloy", Additive Manufacturing, 105, 104750 (2025). doi: 10.1016/j.addma.2025.104750
[27] G. Liu, Y. Su, X. Pi, D. Liu, and Y. Lin, "Fatigue Strength Improvement of Laser-Directed Energy Deposition 316L Stainless Steel with In Situ Ultrasonic Rolling by Preliminary Investigation", Materials, 17, 3693 (2024). doi: 10.3390/ma17153693
[28] R. Xiao, S. Guo, M. Zheng, D. Zou, and T. Huang, "New method for high-efficiency keyhole-based wire direct energy deposition: Filler wire melting efficiency", Optics & Laser Technology, 193, 114257 (2026). doi: 10.1016/j.optlastec.2025.114257
[29] S. B. Han, Y. Lee, H. Lee, J. S. Jang, S. H. Park, and H. Song, "Tailoring solidification and strength enhancement through process parameter optimization in Nb-added 316L stainless steel fabricated by directed energy deposition (DED)", Journal of Materials Research and Technology, 39, 4532-4543 (2025). doi: 10.1016/j.jmrt.2025.10.082
[30] S. Lee, R. Ghiaasiaan, P. R. Gradl, S. Shao, and N. Shamsaei, "Additively manufactured 316L stainless steel via laser powder directed energy deposition (LP-DED): Mechanical properties at cryogenic and elevated temperatures", International J. Fatigue, 182, 108197 (2024). doi: 10.1016/j.ijfatigue.2024.108197
[31] T. DebRoy, H. L. Wei, J. S. Zuback, T. Mukherjee, J. W. Elmer, J. O. Milewski, A. M. Beese, A. Wilson-Heid, A. De, and W. Zhang, “Additive manufacturing of metallic components – Process, structure and properties”, Progress in Materials Science, 92, 112–224 (2018). doi: 10.1016/j.pmatsci.2017.10.001
[32] Z. Chen, Z. Zhang, Y. Yang, G. Xiao, M. Yi, T. Zhou, and C. Xu, "Influence of interlayer dwell time on microstructure and mechanical properties additively manufactured 316L stainless steel by laser directed energy deposition", J. Materials Research and Technology, 34, 1304-1312 (2025). doi: 10.1016/j.jmrt.2024.12.120
[33] J. Wang, R. Zhu, Y. Liu, and L. Zhang, "Understanding melt pool characteristics in laser powder bed fusion: An overview of single- and multi-track melt pools for process optimization", Advanced Powder Materials, 2, 100137 (2023). doi: 10.1016/j.apmate.(2023).100137
[34] D. Guo, K. Yan, M. D. Callaghan, D. Daisenberger, M. Chatterton, J. Chen, A. Wisbey, and W. Mirihanage, "Solidification microstructure and residual stress correlations in direct energy deposited type 316L stainless steel", Materials & Design, 207, 109782 (2021). doi: 10.1016/j.matdes.2021.109782
[35] P. K. Shanmuganathan, D. B. Purushothaman, and M. Ponnusamy, "Effect of High Laser Energy Density on Selective Laser Melted 316L Stainless Steel: Analysis on Metallurgical and Mechanical Properties and Comparison with Wrought 316L Stainless Steel", 3D Printing and Additive Manufacturing, 10, 3 (2023). doi: 10.1089/3dp.2021.0061

ترسيب الطاقة المباشر بالليزر للفولاذ المقاوم للصدأ 316 L منخفض الكاربون: دراسة تأثير معلمات المعالجة على المسامية وتطور البنية المجهرية

سامر نوري علي[1]،*، زياد أياد طه[1] ، باربارا بريفيتالي[2]

[1]معهد الليزر للدراسات العليا، جامعة بغداد، بغداد، العراق

[2]قسم الهندسة الميكانيكية، بوليتكنيكو دي ميلانو، فيا لا ماسا 1، 20156 ميلانو، إيطاليا

البريد الالكتروني للباحث: samirnoori@ilps.uobaghdad.edu.iq

الخلاصة: استخدمت تقنية الترسيب المباشر للطاقة بالليزر (LDED) لتصنيع الفولاذ المقاوم للصدأ منخفض الكربون 316L، ولتقييم تأثير معايير المعالجة على المسامية والكثافة النسبية والصلابة المجهرية. استخدم نظام ليزر ليفي يعمل بطول موجي 1070 نانومتر (YLS-3000-CUT، IPG ABB). كان قطر شعاع الليزر 1.2 مم، ومعدل تغذية المسحوق 9.5 غ/دقيقة، وسمك الطبقة 0.2 مم، ومعدل تدفق الغاز الحامل 7.5 لتر/دقيقة، ومعدل تدفق غاز الحماية 25 لتر/دقيقة. تم تغيير قدرة الليزر (420، 600، و800 واط) وسرعة المسح (20، 25، و30 مم/ثانية) بشكل منهجي، مما أنتج تسع عينات بكثافات طاقة خطية تتراوح بين 14 و40 جول/مم^3، وكثافات طاقة حجمية تتراوح بين 59 و167 جول/مم^3. تم فحص الخصائص الميكروية وبنية المسام باستخدام المجهر الضوئي والمجهر الإلكتروني الماسح. وتم تحديد المسامية والكثافة النسبية كميا من خلال تحليل صور المقطع العرضي الكامل. وقيست الصلادة الميكروية باستخدام جهاز فيكرز بحمل 300 غرام وزمن تثبيت 10 ثوان. وتراوحت قيم الصلادة الميكروية بين 185.4 و207.3 HV. وتراوحت قيم المسامية بين 0.198% و0.831%، بينما تراوحت الكثافة النسبية بين 99.169% و99.802%. وأدت كثافات الطاقة الحجمية المنخفضة إلى انخفاض المسامية وزيادة الكثافة النسبية عند جميع سرعات المسح. وتم الحصول على أدنى مسامية (0.198%) وأعلى كثافة نسبية (99.802%) عند سرعة مسح 30 مم/ث وكثافة طاقة حجمية 59 جول/مم^3. تحدد النتائج كميا تأثير قوة الليزر وسرعة المسح على التكثيف والاستجابة الميكانيكية في L316 المعالج بتقنية LDED وتحدد نافذة معالجة محدودة لتقليل العيوب.

IJL, Vol. 25, Issue 1, 2026 **Research Article**
http://doi.org/10.31900/ijl.v25i1.564

Assessment of the Impact of Annealing on the Optical Properties of Cadmium Sulfide Thin Films by Spin Coating Deposition (SCD)

Atyaf Adnan Farhan*

Ministry of Education, Al-Karkh Second Directorate of Education, Al-Mustafa Secondary School for Distinguished Students
*Email of the Corresponding Author: atyafadnan8892@gmail.com

Article history: Received 4 Feb. 2026, Accepted 19 Mar. 2026, Published online 15 Jun. 2026

Abstract: Cadmium sulfide (CdS) thin films have been fabricated on glass substrates via the spin-coating method, followed by thermal annealing at 100°C, 150°C, and 200°C. Optical studies indicated that the deposited films possess high transparency in the visible and near-infrared regions, with transmittance values reaching approximately 75%. The films exhibited a direct optical band gap, which showed a gradual decrease from 2.2 eV to 1.6 eV as the annealing temperature increased. Additionally, increasing the annealing temperature resulted in noticeable improvements in film homogeneity and crystallinity. These findings underscore the crucial role of thermal annealing in modulating the optical properties of CdS thin films, thereby improving their suitability for optoelectronic applications.

Keywords: Spin Coating Deposition (SCD), Atomic Force Microscopy (AFM), Zinc Blende (ZB), CdS (Cadmium Sulfate).

1. Introduction

Cadmium sulfide (Cd S), a typical II–VI compound semiconductor, shows a unique bonding nature that combines the covalency and ionicity. In the former, a large electronegativity difference between cationic Group II (Cd) coating and the VI elements (S), endows largely ionic aspects to the almost covalent bonding. Intense electron localization, binding of lattice energies, and thereby higher thermal stability are some of the outcomes. These basic properties appear as the characteristic melting points and wide band gaps compared to covalent semiconductors of comparable atomic mass (e.g., silicon/germanium) [1].

Cadmium sulfide occurs in two major structural forms, the cubic zinc blende (sphalerite) phase and hexagonal wurtzite phase. The instability at the planar film surface is so solid that when deposited at substrate temperatures where the formation of these phases is thermodynamically stable and kinetically preferrable, thin films may not form ordered phases. For CdS, the metaphase is zinc blende (ZB), which is favoured at lower substrate temperatures (300°C), the thermodynamically-stable wurtzite phase is dominant by virtue of its lower bulk free energy. This phase selectivity has important consequences for epitaxial growth, defect creation and subsequent properties [2]. Recent progress on control of phase-pure or mixed-phase films is also achieved in Fiske cells for device applications via molecular beam epitaxy (MBE) and pulsed laser deposition (PLD). The renewed and persistent interest in CdS thin films is mainly attributed to its critical function as a window material for high-efficiency thin-film photovoltaic (PV) devices, including predominantly heterojunctions with semiconductor absorbers like CdTe and

$Cu(In,Ga)Se_2$ (CIGS) [3,4]. Its appropriateness is based on a combination of key features: the direct band gap (~2.42 eV at room temperature), that lies comfortably in the solar spectrum well below its absorption edge; high (it exceeds 10^4 cm^{-1}) absorption coefficient for photon energies larger than the band gap, which should enable efficient carrier generation in ultrathin layers; and favorable interface energetics with leading absorber materials to promote successful carrier separation. These properties have allowed certified solar cell conversion efficiencies in CdTe devices in excess of 22% and for CIGS they are around 23%, with the key component of recently recorded efficiency architectures remaining a CdS layer [5,6]. Apart from photovoltaic applications, due to the tunable band gap (by alloying with Zn or Se) and the strong excitonic effects, CdS is of interest for light-emitting diodes (LEDs), photodetectors and nonlinear optical devices.

Cadmium sulfide is a congruently sublimating material at around 700 °C or higher abd melts at high pressure near 1750°C, allowing for fabrication with a wide range of techniques including thermal evaporation, chemical bath deposition (CBD), sputtering and close-spaced sublimation (CSS). The static dielectric constant of the material is ~11.6, and its density is 4.84 g/cm^3. A defining and technologically important characteristic of CdS is its inherent n-type conductivity in as-deposited films. This conductivity is due to intrinsic defects, primarily sulfur vacancies (V_S) and cadmium interstitials (Cd_i), acting as shallow donors. On the other hand, successful p-type doping is challenging—a typical example of the problem of "doping asymmetry" in large band-gap II-VI compounds. This is due to the presence of strong self-compensation mechanisms, which leads to a decrease in the formation energy of native acceptor (e.g., Cd vacancy, V_Cd) upon n-type doping or compensating donor defects spontaneously appearing against desired p-type dopants such as Na or N [7,8]. This asymmetry inherently results in the hindrance of CdS homojunction device.

The microstructure of the polycrystalline CdS films is closely related to their electrical and optical properties. Undoped single-crystal CdS has resistivity values as high as 10^12 Ω·cm, whereas polycrystalline films usually show lower resistivity because of grain boundary conduction and native defects. Doping control with group III (In, Al, Ga) [10] or halogen (Cl, Br) can decrease the resistivity to the order of 10^{-3}–10^{-1} Ω·cm, which is essential for low-resistance window layers [9]. Grain size, which is usually in the 0.3–0.5 μm range for standard thicknesses, plays a crucial role in determining the carrier mobility, recombination and optical scattering of a material. In particular, post-deposition thermal annealing is crucial for promoting grain growth, suppressing the density of grain boundaries and passivating intra-grain defects. A significant step in CdTe PV processing is $CdCl_2$ vapor or solution treatment before annealing. This chloride treatment significantly increases recrystallization, facilitates grain boundary passivation (most likely via the generation of ClS donors that compensate deep traps), and optimizes the electronic structure at the CdS/CdTe interface, resulting in large enhancements in VOC and FF [10,11]. Recent investigations include interface engineering with ultrathin (<50 nm) CdS layers or CdS:O alloys to reduce parasitic absorption and improve the blue-response of the solar cells

2. Materials and methods

In the present work, CdS thin films have been deposited onto glass substrates using the spin-coating technique. This method involves dispensing a precursor solution onto the glass substrate, followed by high-speed rotation to achieve uniform film deposition. After deposition, the films have been subjected to thermal annealing at different temperatures in order to investigate the effect of annealing temperature on their structural and optical properties.

2.1. Devices and Materials.

Cadmium sulfide (CdS) was obtained from Sigma-Aldrich (Germany), and a sensitive scale with four digits, an electric oven with high temperature control, a magnetic stirrer, and a spin coating device.

2.2. Film Deposition by Spin Coating Technique

The three main physical stages of spin-coating are (i) deposition and spin-up, (ii) spin-off or viscous flow, and (iii) solvent evaporation. The method commences deposition of a precursor solution onto a

substrate or Slowdive from a syringe or nozzle. The substrate is then quickly sped up to the desired rotation speed. In this early phase, centrifugal forces are the dominant factor driving the solution away radially. This leads to a rapid, exponential decay in film thickness with the extra removed liquid being expelled from the edges of the substrate until an equilibrium metastable fluid layer is formed.

After uniform spreading, the film-thinning rate enters into a regime determined by the competition between centrifugal drainage and viscous resistance. Although solvent evaporation also takes place, the dominating mechanism for thickness decrease is still the viscous flow of solution across the substrate due to centrifugal force. The thickness decays as $t-1/2t-1/2$, where t is time. In the last stage, viscous flow is suppressible because the solution viscosity dramatically increases owing to solvent evaporation. Additional thinning and drying are primarily governed by the solvent evaporation rate, which results in film contraction to form a dry solid film. It should be noted that these stages are not isolated and considerable overlap in time is present, especially between the spin-off and evaporation stages since solvent evaporation occurs throughout the entire process [12]. The resulting DFT (h) follows a known inverse-power relationship with the square root of the spin speed (ω), typically of the form $h\propto\omega-1/2h\propto\omega-1/2$ and diminishes logarithmically in time as spinning progresses through its mid-stage (=the dominant spin-off phase). This relationship is depicted schematically in Fig. 1.

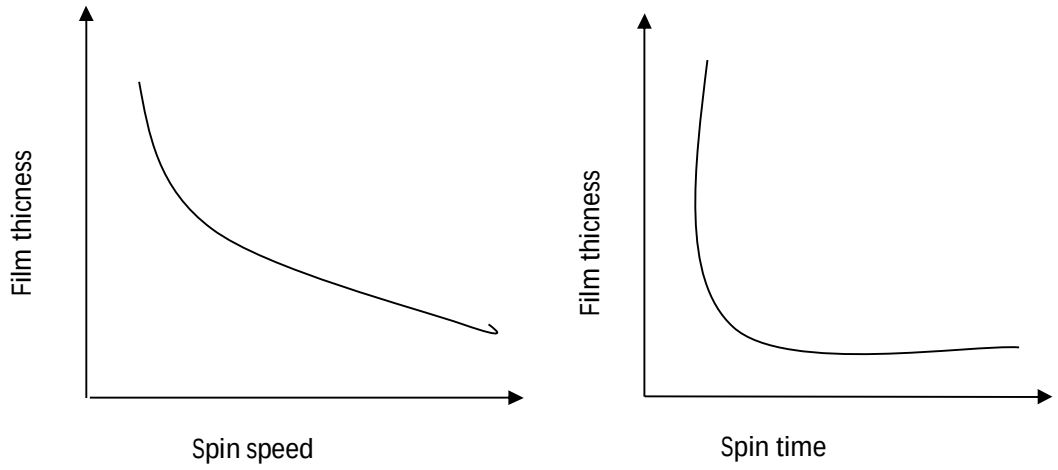

Fig.1: The relation between film thickness and both spin speed and spin time.

2.3. Preparing the Chemicals

Analytical-grade chemicals supplied by BDH were used in the present study. The specifications and chemical parameters of the materials employed are listed in table 1.

Table 1. List of used materials.

Material	atomic weight	Purity	Chemical Composition	Concentration	Company
Cadmium Nitrite	308.47	99%	$Cd(NO3)_2.4H_2O$	0.60 M	BDH
Thiourea	76.12	99%	$Cs(NH_2)_2$	1.0 M	BDH
Polyvinyl alcohol (PVA)	1400	99%			BDH

2.4. Synthesis of CdS/PVA Nanocomposite Thin Films

Thin films of cadmium sulfide polyvinyl alcohol (PVA) matrix nanocomposite have been produced on glass substrate by using the spin coating method. The cadmium source was cadmium acetate tetrahydrate [$Cd(NO_3)_2 \cdot 4H_2O$] and the sulfur precursor used was thiourea [$CS(NH_2)_2$]. Stoichiometric 3:5 (Cd:S) molar ratio was used, with polyvinyl alcohol PVA serving as a host polymer matrix and stabilizer of particle growth and aggregation.

The cation/anion ratio of the Cd:S precursor is one of the most crucial synthetic factors, which is directly responsible for a particular crystallographic phase of the CdS formed. The presence of high sulphur concentration has been demonstrated to promote hexagonal (wurtzite) phase formation, which is usually beneficial for photovoltaic applications because of its electronic properties; while the presence of high cadmium concentration favours cubic (zinc blende) phase stability [13]. The synthesis procedure includes preparation of a precursor matrix by mixing 20 mL of aqueous cadmium acetate solution (0.6 M) with an equal volume of aqueous PVA solution (5% w/v).

The resulting colourless solution was continuously magnetically stirred at 70 °C for 90 min and further aged overnight to afford a homogeneous transparent product, indicating complete incorporation of the cadmium precursor into the polymer matrix. Then, 20 mL of a 1 M thiourea solution was added dropwise with vigorous stirring for another 30 min to start the reaction. Before deposition, the glass substrates were cleaned with a common chemical cleaning process. Then the precursor solution prepared naturally was spin-coated on the substrates. Wet films were then thermally annealed (after deposition) in an ordinary oven at 100 °C, 150 °C and 200 °C. Colouration of the transparent films tints light yellow between 15–20 min during thermal annealing, indicative of NPs being in situ generated within PVA matrix. In this hybrid material, the PVA not only forms a stable and uniform film but also passivates the nanoparticle surfaces, preventing Ostwald ripening and leading to a homogeneous dispersion.

3. Results and discussion

3.1. X-Ray Diffraction (XRD) Analysis

The structural properties of the spin-coated CdS thin films have been examined using X-ray diffraction (XRD) with CuKα radiation. Figures 2, 3, and 4 present the XRD patterns of CdS thin films annealed at 100 °C, 150 °C, and 200 °C for 10–15 minutes, respectively.

The XRD patterns of the annealed samples exhibit diffraction peaks at approximately 24.16°, 20.94°, and 22.00°, corresponding to the characteristic reflections of CdS. The presence of relatively weak and broadened diffraction peaks indicates the formation of nanocrystalline CdS films. The broadening of the diffraction peaks is attributed to the small crystallite size, as peak width increases with decreasing particle size due to size-related effects.

Terminal annealing effect on structural features of the CdS/PVA nanocomposite films is shown in Table 1. The crystalline size, as calculated from X-ray diffraction (XRD), demonstrates a positive link with the annealing temperatures as list in table 2. In particular, as the annealing temperature temperatures from 100 °C to 200 °C, the average crystallite size increases from around ~29.97 nm to ~32.90 nm which can be attributed to the improvement of atomic mobility and grain coalescence of smaller grains at high temperature due to minimization for the total surface free energy balance.The comparative summary of crystallite size (via XRD) and optical band gap (Eg) values of the films annealed at different temperatures are summarized in Table 2.
The correlation between these two parameters provide important information about the quantum confinement effect. In general, a decrease of the optical band gap with increasing crystallite size has been observed for semiconductor nanocrystals when their particle size reaches or exceeds the value of the Bohr exciton radius which is believed to indicate loss of quantum confinement.

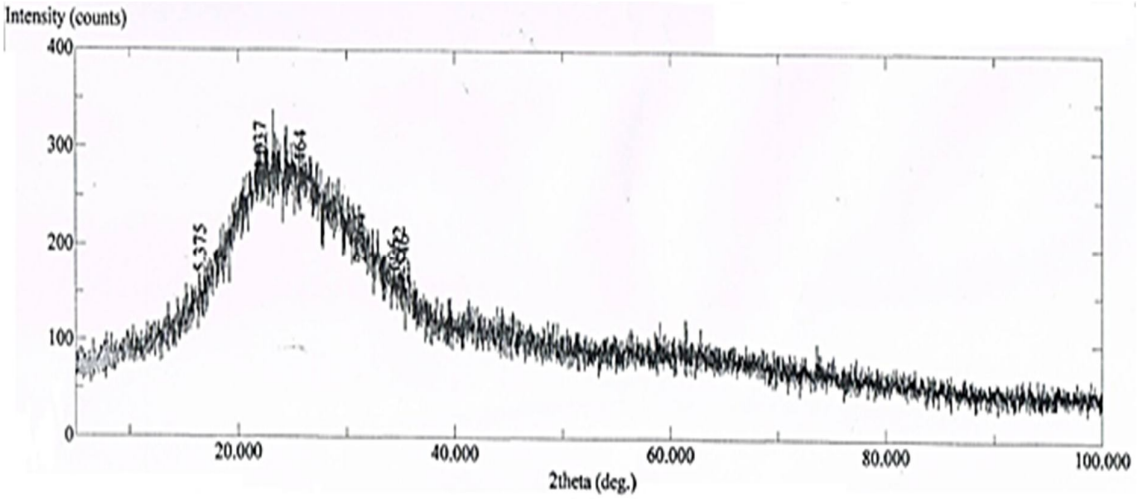

Fig.2: Shows the X-ray diffraction for CdS at 100C°

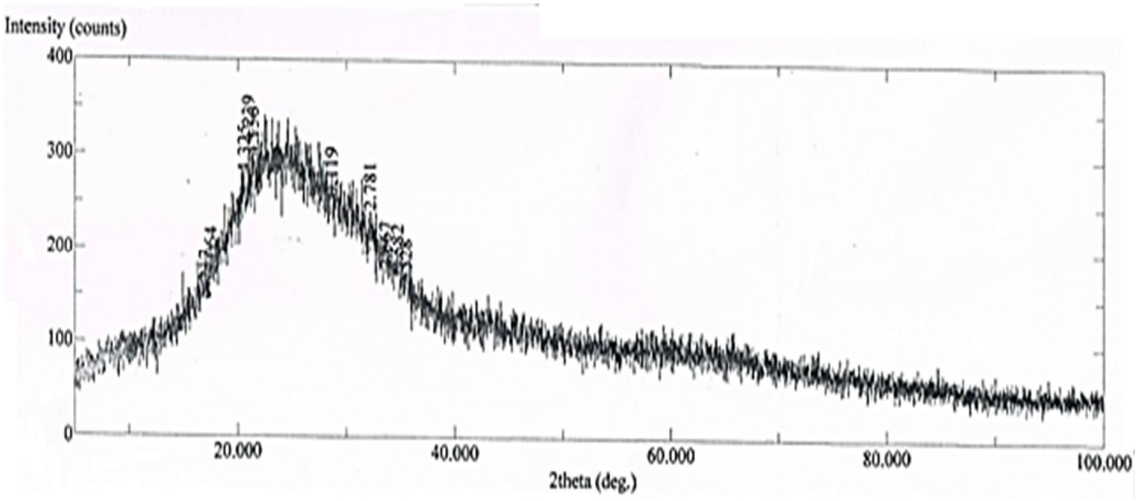

Fig.3: Shows the X-ray diffraction for CdS at 150C°

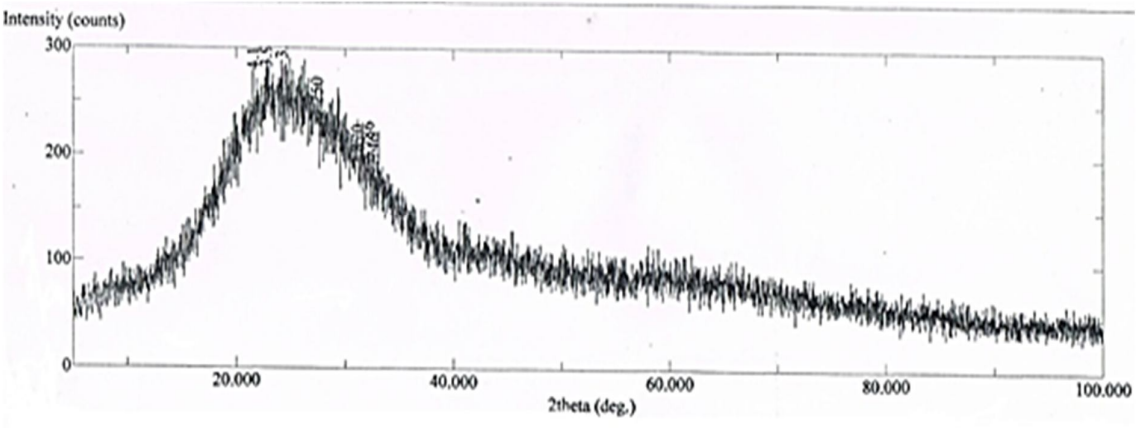

Fig.4: Shows the X-ray diffraction for CdS at 200C°

Table 2. XRD pattern for CdS thin films with different values of annealing temperature.

Annealing Temp (°C)	2θ (Deg.)	FWHM (Deg.)	d_{hkl} (Å)	Intensity	I/I_o	hkl	Card no.
100	16.480	0.259	3.1743	169	62	113	00-041-1049
	22.000	0.282	4.0369	274	100	230	00-010-0454
	25.700	0.282	3.4635	266	98	311	00-041-1049
150	20.520	0.329	4.3246	279	90	113	00-041-1049
	20.940	0.259	4.2388	310	100	230	00-010-0454
	21.360	0.282	4.1564	297	96	311	00-010-0454
200	22.740	0.353	3.9072	281	98	200	00-010-0454
	24.160	0.259	3.6807	289	100	230	00-010-0454
	27.420	0.259	3.2500	234	81	112	00-041-1049

These results prove that the thermal annealing treatment is a reliable process to adjust the
The microstructural and, hence, the optoelectronic characteristics of the CdS/PVA nanocomposite films prepared are shown in Table 2.

Table 3. Values of grain size and energy gap V.S. annealing temperatures.

Ta (C)	Grain No	Avg. Diameter (nm)
100	52	224.45
150	45	212.86
200	81	156.23

Table 4. Average diameter for samples grains at different Ta

Annealing temperature (°c)	Grain size from XRD (nm)	Energy gap (eV)
100	29.97	2.25
150	32.58	1.65
200	32.897	1.60

3.2. Atomic Force Microscopy (AFM)

Fig 5 (a, b & c) shows the atomic force microscopic picture for the three samples at different annealing temperatures Ta=100, 150, and 200 C, respectively. The grain size and the average diameter were listed in Table 4.

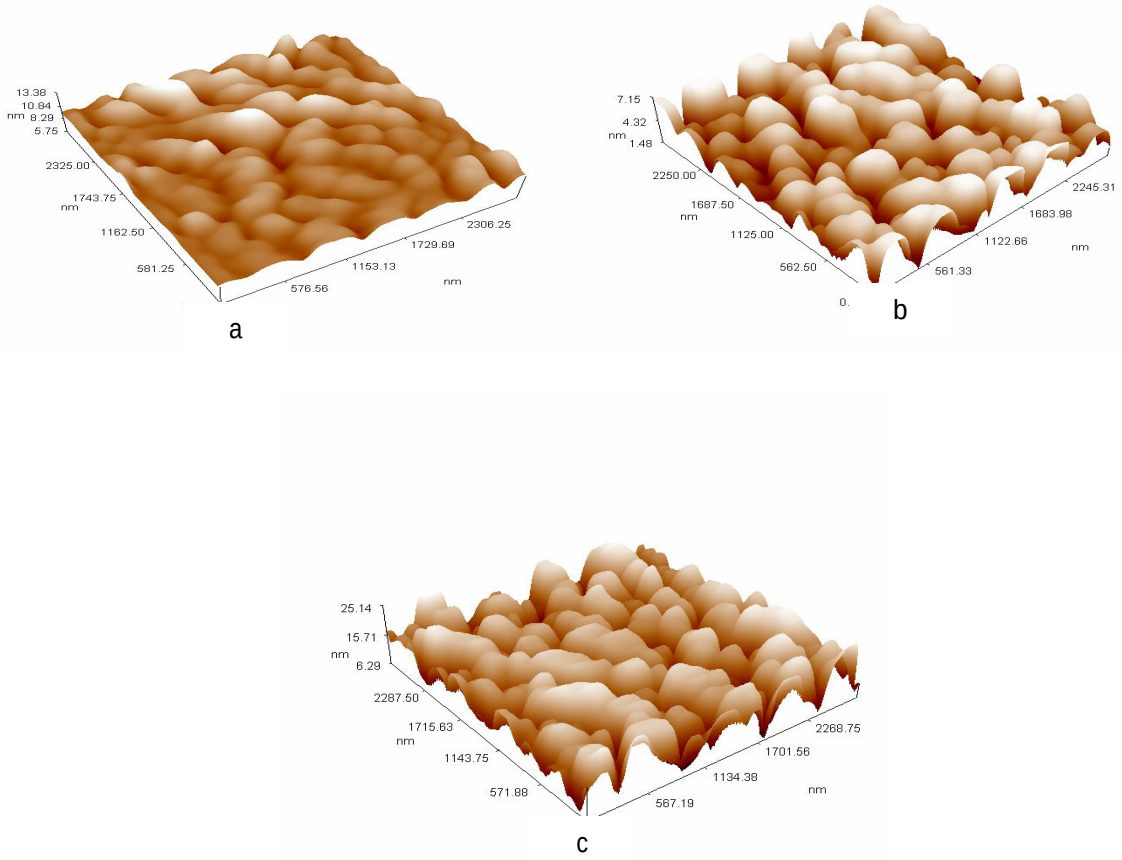

Fig.5: AFM for a) 1st simple at T=100 C^0, b) 2nd simple at T=150 C^0 , c) 3rd simple at T=200 C^0.

3.3 Optical Measurements

3.3.1 Transmittance Spectra

The optical transmittance of the CdS films has been measured at avroom temperature in the 300–1100 nm wavelength range shown in Figure 6. Most of the prepared films possess high optical transparency in the visible and near infrared ranges, with transmittance over 85% for all.

A gradual reduction in the optical transmittance is seen with increasing annealing temperature, and this data is summarized table 4. This decrease is related to the micro structuring evolution of the films. The improvement of sub crystallinity, grain size and texture (XRD) are all confirmed for the post-deposition annealing. These microstructural enhancements contribute to an increased volume fraction of crystalline material and a decrease in the amount of light scattering at grain boundaries that can be directed toward in-plane optical modes, resulting in a higher effective optical path length and inner absorption within the films. As a result, the annealed films show higher photon absorbing ability reflected with the measured decrease in total transmittance.

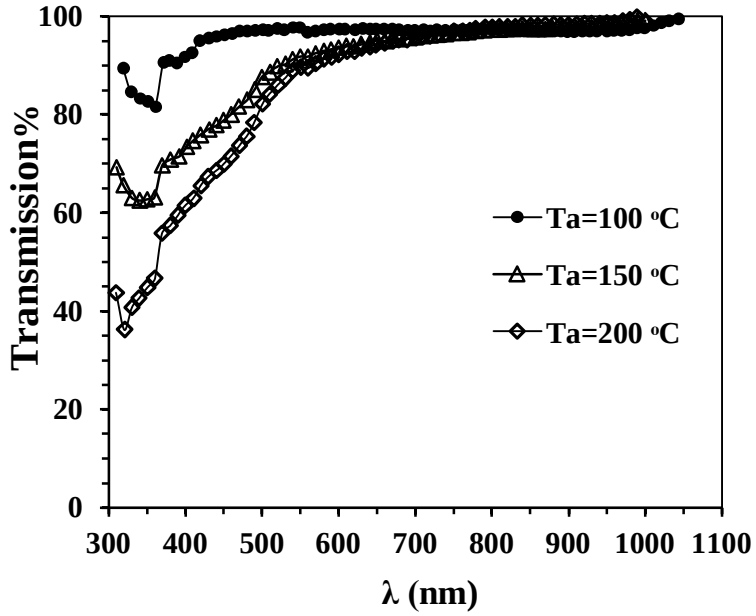

Fig.6: Transmittance spectra of CdS thin films annealed at different temperatures.

3.3.2. Optical Energy Gap

The optical energy gap (Eg) of the CdS thin films has been calculated using the Tauc formula. In order to investigate the nature of the optical transition, $(\alpha h\nu)^2$ was plotted as a function of photon energy ($h\nu$), where α represents the absorption coefficient. Extrapolation of the high-absorbing region in the plot to the energy axis resulted in a straight line, verifying a direct allowed transition for CdS. The calculated optical band gap is shown in Fig.7.

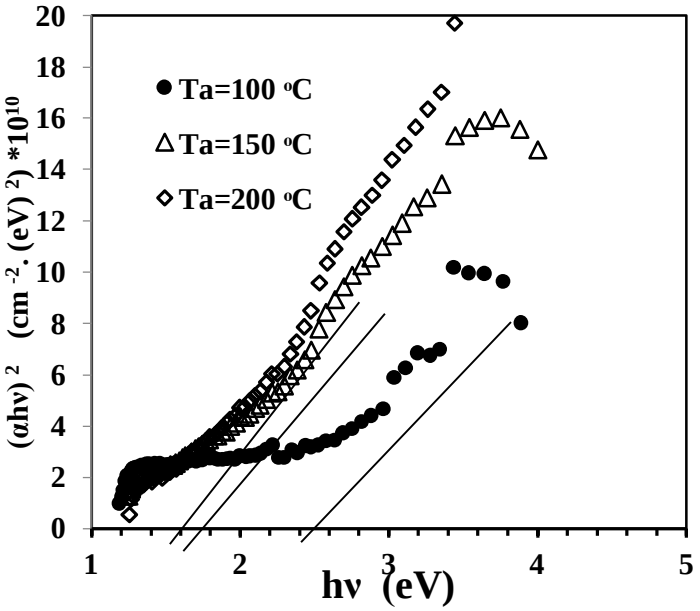

Fig.7: Tauc plots for determining the optical energy gap of CdS thin films annealed at different temperatures.

The optical band gaps of all the samples are respectively 2.3 eV for the unannealed one, and decrease with elevated annealing temperature (Ta). This discovered band gap reduction may be associated with the microstructural evolution of the films following annealing. In contrast, high grain growth and good crystallinity are achieved with the increase of annealing temperature, as verified from XRD. The resulting increase in the crystallite size is responsible for a suppression of quantum confinement effects, which are extremely strong in nanostructured semiconductors. Besides, as the lessened structural disorder and defect density (due to better crystallinity) reduces the density of localized tail states close to the band edge, such a change leads to a clear optical band gap increase.

3.3.3. Optical and Structural Parameters

All calculated optical and structural parameters of the CdS thin films annealed at different temperatures are summarized in Table 5.

Table 5. Calculations of the Optical and structural properties at different temperatures

Parameters	T=100 C^0	T=150 C^0	T=200 C^0
Grain size	29.9	32.58	32.9
Absorption of films	0.011	0.028	0.035
Transmission spectra	97.427%	93.691%	92.235%
Optical Energy Gap	2.25	1.65	1.60

4. Conclusion

CdS/PVA nanocomposite thin films were successfully fabricated using the spin-coating technique, and the effect of thermal annealing on their structural and optical properties was investigated. XRD analysis showed an increase in crystallite size with increasing annealing temperature, indicating improved film crystallinity. Optical studies revealed enhanced absorption and a corresponding decrease in transmittance as the annealing temperature increased. Additionally, the optical energy gap exhibited a noticeable reduction with increasing annealing temperature. These findings demonstrate that thermal annealing is an effective approach for tuning the properties of CdS/PVA thin films for optoelectronic applications.

Ethics Approval and Consent for Authors

I acknowledge that I have completed my research in accordance with the ethics of scientific research and submitted my research paper, which aims to serve the community.

Author declaration

I, Atyaf Adnan Farhan, hereby declare that I am the sole owner of the intellectual property rights to the research manuscript titled "[Assessment of the Impact of Annealing on the Optical Properties of Cadmium Sulfide Thin Films by Spin Coating Deposition (SCD)]" submitted for publication in the Iraqi Journal of Laser.

References

[1] Vanalakar, S.A., Patil, V.L., Patil, S.M., Deshmukh, S.P., Patil, P.S., and Kim, J.H., Chemical and gas sensing property tuning of cadmium sulfide thin films. Materials Science and Engineering: B, **282**, p.115787 (2022), https://doi.org/10.1016/j.mseb.2022.115787.
[2] A. I. Khudiar, S. M. Zulfequar and Z. H. Khan, Chalcogenide Letters, 7, 291-298 (2010). https://chalcogen.ro/291_Kudhiar.pdf
[3] D. Saikia, P. K. Gogoi and P. K. Saikia:Chalcogenide Letters. **7**, 317-323 (2010). https://pubs.acs.org/doi/abs/10.1021/cm990362%2B
[4] V. B. Sanap and B. H. Pawar: Chalcogenide Letters. **6**, 415-419 (2009). https://chalcogen.ro/419_Sanap-sept.pdf

[5] M. Thambidurai, N. Murugan, N. Muthukumarasamy, S. Agilan, S. Vasanthaand R. Balasundaraprabhu: J. Mater. Sci. Technol. **26**, 193-199 (2010).
[6] D. Nesheva, Z. Aneva, S. Reynolds, C. Main and A. G. Fitzgerald:Journal of Optoelectronics and Advanced Materials. **8** ,2120-2125 (2007). https://www.researchgate.net/publication/303876337.
[7] Faris, Mina Mohammed, and Asmaa Kadim Ayal. "Electrochemical Synthesis of Fe-doped TiO2 Nanotube for Gas Sensor Application." Iraqi Journal of Science **66**, 5, 1437-1450 (2025). DOI: 10.24996/ijs.2025.66.4.4
[8] Yildirim, E., Ozmen, S.I., Havare, A.K. and Gubur, H.M., Substrate effect on nanowall-structured CdS thin films obtained by CBD: Structural, optical, and electrochemical characterization for next-generation optoelectronic applications. Materials Chemistry and Physics, **348**, 1311-51. (2026)https://doi.org/10.1016/j.matchemphys.2025.131651.
[9] Hur, S.G., Kim, E.T., Lee, J.H., Kim, G.H. and Yoon, S.G., Characterization of photoconductive CdS thin films prepared on glass substrates for photoconductive-sensor applications. Journal of Vacuum Science & Technology B: Microelectronics and Nanometer Structures Processing, Measurement, and Phenomena, **26(4)**, 1334-1337(2008) https://doi.org/10.1116/1.2945301.
[10] Bhusan, S., & Oudhia, A.. Photoconductivity and photoluminescence studies of chemically deposited CdS-Se: CdCl2, Ho/Nd films. Indian Journal of Pure & Applied Physics, **47**(1), 60. (2009) https://d1wqtxts1xzle7.cloudfront.net/75805510/IJPAP_20471_2060-65-libre.pdf
[11] Oliva, A.I., Castro-Rodrıguez, R., Solıs-Canto, O., Sosa, V., Quintana, P. and Pena, J.L., Comparison of properties of CdS thin films grown by two techniques. Applied surface science, **205(1-4)**,56-64. (2003) https://doi.org/10.1016/S0169-4332(02)01081-4
[12] Faris, M.M. and Ayal, A.K. Effect of voltage on gas sensor performance of anodization synthesized TiO2 nanotubes arrays. Iraqi Journal of Science, **64**,6135-6147(2023). DOI: 10.24996/ijs.2023.64.12.5
[13] M.Zambuto: Semiconductor Device (McGraw-Hill Book Company, USA, (1989).
[14] Haider, A.J., Mousa, A.M. and Al-Jawad, S.M. Annealing effect on structural, electrical and optical properties of CdS films prepared by CBD method. Journal of semiconductor technology and science, **8(4)**, 326-332,(2008)https://d1wqtxts1xzle7.cloudfront.net/50225322/Year2008Volume08_04_08-libre.pdf?1478764913
[15] Kennedy, A., Kumar, V.S. and Raj, K.P., Chemical spray deposition technique of antimony (Sb) doped polycrystalline MnIn2S4 thin films: Preparation and characterization. Materials Letters, **195**, pp.96-99. (2017) https://doi.org/10.1016/j.matlet.2017.02.107
[16] Al-Douri, A.A.,. Annealing temperature effect on the structural and optical properties of thermally deposited nanocrystalline CdS thin films. Iraqi Journal of Physics, **10(18)**,111-116(2012). https://www.ijp.uobaghdad.edu.iq/index.php/physics/article/view/756/542
[17] Akintunde, J.A., Effects of deposition parameters and conditions on the physical and electro-optical properties of buffer solution grown CdS thin films. physica status solidi (a), **179(2)**,363-371(2000) https://doi.org/10.1002/1521-396X(200006)179:2<363::AID-PSSA363>3.0.CO;2-L
[18] D. A. Newmen:Semiconductor Physics and Devices. Richard D. IRWIN, INC., USA (1992).
[19] Heo, J., Ahn, H., Lee, R., Han, Y. and Kim, D., Influence of ITO surface modification on the growth of CdS and on the performance of CdS/CdTe solar cells. Solar Energy Materials and Solar Cells, **75(1-2)**, 193-201(2003) https://doi.org/10.1016/S0927-0248(02)00155-1.
[20] N. Mott and E. Davis: Electronic Process in Non-Crystalline Materials (Oxford University Press, 2nded. (1980).
[21] T.S.Moss: Semiconductor Opto-electronics (Butter Worths Sci. publishing, London (1973).
[22] Muhammed Abdurraheem, Sunday Ajani, Wasiu Yahya, Godwin Egbeyale, Computational Approach to the Study of Photon Radiation Shielding Parameters of Perovskite Ceramics , Iraqi Journal of Physics: **23**, 4 (2025) https://www.ijp.uobaghdad.edu.iq/index.php/physics/article/view/1518
[23] Ali, M.M., Abbas, S.J. and Al-Kabbi, A.S., Effect of Annealing Temperature on Structural and Optical Properties of CdS Thin Films Prepared by CBD and Thermal Evaporation Techniques. Journal of Basrah Researches(Sciences), **45(1)**,(2019)https://iasj.rdd.edu.iq/journals/uploads/2024/12/08/0de7bd73c8b0ee38f2e20224b6867f60.pdf

تقييم تأثير التلدين على الخصائص البصرية للأغشية الرقيقة من كبريتيد الكاديوم بواسطة الترسيب بالطلاء الدوراني (SCD)

أطياف عدنان فرحان *

وزارة التربية والتعليم / مديرية الكرخ الثانية للتربية والتعليم / مدرسة المصطفى الثانوية للطلاب المتفوقين

البريد الالكتروني للباحث: *atyafadnan8892@gmail.com*

الخلاصة: تم تصنيع أغشية رقيقة من كبريتيد الكادميوم (CdS) على ركائز زجاجية باستخدام طريقة الطلاء الدوراني، ثم خضعت لمعالجة حرارية عند درجات حرارة 100 و150 و200 درجة مئوية. أشارت الدراسة البصرية إلى أن الأغشية المترسبة تتمتع بشفافية عالية في نطاقي الضوء المرئي والأشعة تحت الحمراء القريبة، حيث بلغت قيم النفاذية حوالي 75%. أظهرت الأغشية فجوة نطاق ضوئي مباشرة، والتي انخفضت تدريجيا من 2.2 إلكترون فولت إلى 1.6 إلكترون فولت مع ارتفاع درجة حرارة المعالجة. بالإضافة إلى ذلك، أدى رفع درجة حرارة المعالجة إلى تحسينات ملحوظة في تجانس الأغشية وبلوريتها. تؤكد هذه النتائج على الدور المحوري للمعالجة الحرارية في تعديل الخصائص البصرية لأغشية CdS الرقيقة، مما يحسن من ملاءمتها للتطبيقات الكهروضوئية.

IJL, Vol. 25, Issue1, 2026
http://doi.org/10.31900/ijl.v25i1.560

Research Article

Effects of Laser Irradiation on Copper Phthalocyanine Nanostructure and its Optoelectronic Device

Zainab Hazim Abdul Raheem [1,*], Mohammed K. Khalaf [2], Sameer Khudhur Yaseen [1]

[1]*Department of Physics, College of Science for Women, University of Baghdad, Baghdad, Iraq*
[2]*Scientific Research Commission, Baghdad, Iraq*
** Email address of the Corresponding Author: zainab.h@csw.uobaghdad.edu.iq*

Article history: Received 4 Jan. 2026, Accepted 27 Mar. 2026, Published online 15 Jun. 2026

Abstract: Copper phthalocyanine (CuPc) films exhibit strong absorption as well as chemical stability against visible light and hence are attractive organic semiconductors for an optoelectronic device. In the present work, we have studied the influence of 650 nm laser irradiation on the 478.4 nm Cupc thin film and recorded its photodetector behavior. X-ray diffraction analysis showed increased crystallinity of laser-treated samples, in which the crystallite size enhanced from 30.48 to 39.03 nm with diminished microstrains. The average grain size increased from 35.77 nm to 95.19 nm, while the surface roughness decreased as observed by an atomic force microscope (AFM), evidencing a remarkable grain growth and surface smoothing process. The optical properties revealed small changes in the π–π* transitions and a slight increase in the optical band gap from 1.82 to 1.84 eV, indicating a decrease in the disorder of the structure. Hall effect measurements revealed that an increase in the carrier mobility from 0.16 to 28.9 $cm^2/V•s$ resulted in good electrical properties despite a decrease of the free electron concentration (n) due to the hole compensation mechanism. Meanwhile, the responsivity of laser-treated CuPc photodetector dramatically improved from 54.92 to 190.98 μA/mW as well as external quantum efficiency increased from 10.89% to 37.89% at a wavelength of 625 nm. These enhancements are ascribed to the laser-induced molecular realignment, reduced trap density, and enhanced charge transport path.

Keywords: CuPc thin film, Charge transport, Laser Irradiation, Organic Photodetector.

1. Introduction

As an emerging class of optoelectronic materials, organic semiconductors have been attracting increasing attention due to their various advantages, such as being low-cost and easy to fabricate, outdoor mechanical flexibility, lightweight, and tailorable optoelectronic characteristics [1-3]. Among these, metal phthalocyanines have been considered as an attractive family of materials for various optoelectronic applications, including organic photodetectors (OPDs), solar cells, and gas sensors, owing to their chemical stability, strong absorption coefficients in the visible region, and effective charge transport properties [4-5]. Especially CuPc is one of the most studied organic semiconductors due to its thermal stability, environmental strength, and preferable molecular structure [6-8]. The opto-electronic properties

of CuPc thin films are greatly determined by the degree of ordering, surface morphology and defect density, all significantly affected by the fabrication and post-depositing treatment conditions [9-11].

Laser irradiation has lately become an appealing post-deposition modification treatment, because it is local and controllable, no-contact technique [12]. Unlike classical thermal treatments, the laser can locally deposit the needed energy in the material, thus minimizing global heating of the substrate and facilitating structural/morphological optimization. Previous studies have mainly concentrated on the ultraviolet or high-energy laser, which might generate too many thermal effects and chemical damage to organic semiconductors [13]. In this situation, there is a rising interest in the use of visible-light laser irradiation as an alternative, low-energy, and non-destructive method. In the case of CuPc thin film, laser irradiation at 650 nm is particularly attractive since the resulting optical excitation coincides exactly with its intrinsic Q band absorption itself [14].

This spectral complementation ensures that photons can efficiently interact with the molecules to facilitate molecular rearrangement, reinforced π–π stacking, and crystallinity without changing the chemical composition of the material [15]. However, to date, a comprehensive study of the relationship between laser-induced structural and morphological (in terms of charge transport) changes and photodetector performance originating from visible laser-exposed CuPc thin films is still unexplored [16]. Hence, the purpose of the present study is to systematically explore the effect of 650 nm laser light on structural, morphological, optical, and electrical properties in thermally evaporated CuPc thin films. Through systematic characterizations using X-ray diffraction (XRD), atomic force microscopy (AFM), UV–Vis spectroscopy, Hall effect measurements, current–voltage and photoresponse measurements, we discover details of the mechanisms responsible for laser-induced enhancement. By directly correlating laser-induced molecular ordering with device performance, this work offers a useful guideline for developing a simple yet effective approach to improve CuPc-based organic photodetectors.

2. Materials and methods

The blue CuPc pigment powder, with the molecular formula $C_{32}H_{16}CuN_8$, obtained in this work from Sigma-Aldrich Chemical (99% purity), is used as the raw material. After purification, thin CuPc films of varying thicknesses are deposited using thermal evaporation under vacuum. The copper phthalocyanine is heated, evaporated, and then cooled upon contact with a low-temperature surface, forming a single thin film. In this thin-film deposition process, a vacuum of (2×10^{-5}) Torr was used. The dimensions of the deposition tank are designed to ensure the homogeneous distribution of the deposited copper phthalocyanine particles on the substrate, which is the objective of the deposition process. The homogeneity of the deposition layer is crucial for achieving the desired properties and performance. Thin film of copper phthalocyanine 478.4 nm represents S1 thick were produced in a tungsten metal vessel when the evaporation chamber pressure reached 2×10^{-5} Torr, using a coating unit. At room temperature, the material was deposited onto glass, 30 cm from the evaporation tank. The samples are then cooled in the evaporation chamber, and the thickness is measured. The laboratory subsequently ponders over those films' structure, optics, morphology and electrical features (refer to Figure 1), the Diagram of a thermal evaporation system. The evaporation temperature of CuPc depends on the conditions. Still, in general, it requires a higher temperature, ranging from 300 to 400°C, since CuPc is not easily evaporated due to its good thermal resistance.

2.1. Laser irradiation 650 nm

A laser source at 650 nm is based on the visible red-light portion of the electromagnetic spectrum, and serves to be a common wavelength for photo-process applications due to its moderate photon energy and a strong interaction with organic semiconductor absorption bands agree with [17]. This wavelength is

significant in the case of copper phthalocyanine (CuPc) thin films since it coincides with the Q-band absorption, allowing efficient excitation of molecular electronic states. Under 650 nm light irradiation with the laser power 15 mW, and time of irradiation at 10 min, the CuPc experiences photothermal and photochemical processes, which may rearrange molecular packing, improve crystallinity and distribute defects in the film. Red laser photons possess a low enough energy to cause a thermal degradation risk and high enough energy to lead to localized heating for improving the charge mobility via defect healing, and also through molecular reorientation. In addition, the exposure of CuPc thin film represent S2 to 650 nm laser radiation can lead to changes in optical properties; thus, it is a powerful technique for tuning the performance of CuPc-based optoelectronic devices such as photodetectors, sensors and thin film transistors. The controlled and non-invasive nature of this wavelength allows precise tuning of material properties without altering chemical composition, thereby offering a versatile approach for tailoring the functional characteristics of organic thin films.

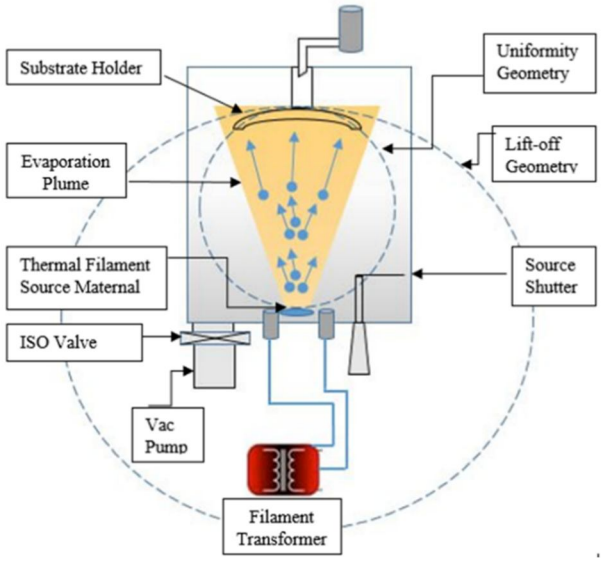

Fig. 1: Thermal evaporation system diagram.

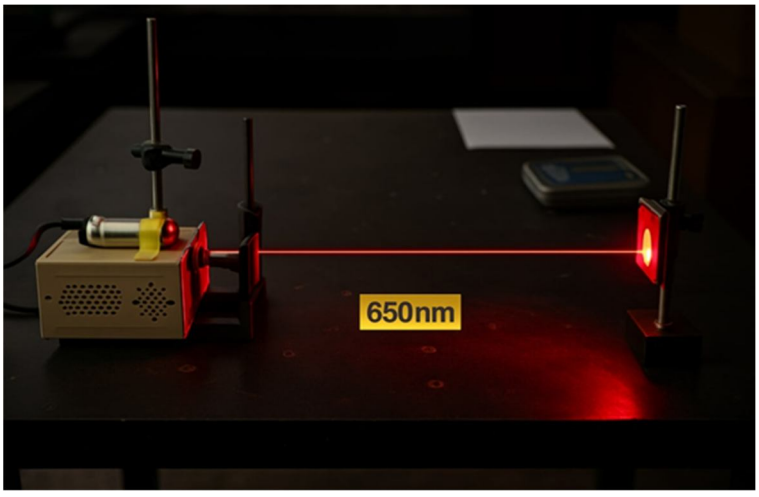

Fig. 2: Schematic of the Laser irradiation 650 nm system.

3. Result and discussion

3.1. Hall effect measurement (HEM)

Finally, the Hall coefficient (RH) of the CuPc films with a thickness of 478.4 nm was derived using Eq. (1). The Hall carrier concentration (nH) and the Hall mobility (μH) could then be obtained by Eqs. (2) and (3), respectively [18,19]. The Hall effect is a crucial tool for characterizing charge carrier dynamics and transport in organic semiconductors. The results in Table 1 show that the resistivity of the two samples are in one order of magnitude of 10^5 Ω•cm, which demonstrates the intrinsic low electrical conductivity of CuPc. However, laser irradiation results in a modest decrease of resistivity from the as prepared value to 1.101×10^5 Ω•cm and accordingly an increase in electrical conductivity from 8.807×10^{-6} to9.080×10^{-6} (Ω•cm) $^{-1}$. This improvement shows the increased charge transport capability after laser treatment probably related to a reorganization of structures and molecules induced by the laser. "Large" changes are also evident in the Hall coefficient: RH rose from 1.792×10^4 cm³/C (untreated film) to 3.183×10^6 cm³/C (laser treatment), confirming that carrier transport has been greatly altered. In accordance with this, the Hall carrier concentration is greatly decreased from 3.483×10^9 to 1.961×10^7 cm^{-3}.

Upon laser irradiation, indicating that the concentration of the free charge carriers for electrical conduction lowered down. In spite of the lower carrier concentration, there is a great improvement in Hall mobility, compared to that of as-prepared films (0.1579cm²/V•s), which reaches 28.90 cm²/V•s after laser irradiation. This large increase in mobility dominates the overall electrical transport response and more than compensates for the reduced carrier density, resulting in a net enhancement of conductivity. The mobility improvement is related to the suppression of trap-assisted scattering, and an enhancement in molecular order and intermolecular orbital overlapping that result in better charge transport efficacies. The conduction type is unchanged during the laser irradiation, indicating that the intrinsic electronic nature of CuPc does not change upon such a substrate treatment whereas the charge transport properties have been greatly enhanced. In general, the above results indicate that 650 nm laser improves the electrical performance of CuPc thin films mainly due to a remarkable enhancement in charge carrier mobility whereas carrier concentration is decreased simultaneously, leading to an enhancement of charge transport efficiency.

$$R_H = V_{H.t}/I.B \quad (1)$$

$$n_H = \pm 1/R_{H.e} \quad (2)$$

$$\mu_H = \sigma/n_H.e = \sigma.|R_H| \quad (3)$$

Table 1. presents the extracted Hall parameters of the CuPc thin films

Sample	(ρ) (Ω cm) Resistivity	(σ) $(\Omega\ cm)^{-1}$ Conductivity	(R_H) (cm^3/C) Average Hall Coefficient	n_H ($/\ cm^3$) Sheet Concentration	μ (cm^2 / V_s) Mobility	Type
S1	1.135 E+5	8.807 E-6	1.792 E+4	3.483 E+9	1.579 E-1	P
S2	1.101 E+5	9.080 E-6	3.183 E+6	1.961 E+7	2.890 E+1	P

3.2. X-ray diffraction

It is clearly shown from the XRD patterns of 478.4 nm thin films that the influence of 650 nm laser light irradiation on structural properties for CuPc is obvious. As depicted in Fig.3, the as-grown film is characterized by a relatively low intensity broad diffraction feature at the (312) plane, which suggests that the sample processed only moderate crystallinity and limited long-range structure order. Such broadening of peaks is indicative of an island like growth behaviour (Volmer–Weber mode), where non-oriented crystallites randomly nucleate on the substrate, leading to a heterogeneous microstructure. For the laser-irradiated CuPc film, by comparison, the diffraction intensity is significantly increased and a clearer, narrower peak appears to be the (312) plane. This behaviour is an indication of appreciable enhancement in crystallinity and molecular ordering brought about by laser irradiation. The observed structural improvement is ascribed to local photothermal effects created by the laser that serve the reorganization of molecules and a reduction in the structural disorder within the film. The enhanced peak sharpness of the laser treated film reveals the growth of crystallite size and a decrease of crystal lattice imperfection towards improving charge transfer characteristics by mitigating grain boundary defects and trap sites. This structural improvement is available in line with the improved carrier mobility determined by the Hall effect measurement. To quantify these changes, the size of crystallite was calculated using the Scherrer equation Eq. (4) [20], and the fitted values are listed in Table 2.

$$D = \frac{0.9\lambda}{\beta \cos\theta} \quad (4)$$

Where:

D: represents the mean crystallite size

β: represents the full width at half maximum (FWHM) of the diffraction peak, expressed in radians.

λ: represents the X-ray wavelength.

θ: the diffraction angle or is the Bragg angle (half the diffraction angle)

K = 0.94: the Scherrer constant, which is approximately equal to one in the case of spherical crystallites.

A diffraction peak stemming from the (312) crystallographic plane is observed for both samples, which verifies that the basic crystal structure of the films is unchanged after irradiation with a laser. The diffraction angle (2θ) exhibited a little shift from 29.15° in the as-prepared film to 29.474° after laser-treatment. This shift indicates small changes in the lattice parameter, presumably due to molecular rearrangement induced by irradiation or relaxation of stress in the film. After the laser treatment, there is an apparent decrease in the full widths at half maximum (FWHMs) from 0.27° down to 0.211°. As FWHM is inversely proportional to crystallite size, this narrowing exactly reflects increasing crystallinity. The calculated crystallite size D increases significantly from 30.48 nm for the prepared film to 39.03 nm for the laser irradiated one.

This improvement could be explained by the establishment of higher-order, and larger crystalline domains probably induced by local photothermal effects on the molecular aligning process and disorder decrease. In addition, the microstrain (ε) decreases from 1.1×10^{-3} to 8.8×10^{-4} associated with laser processing, indicating a decrease in lattice distortion and internal defects, which indeed can be appreciated as a higher value because of the laser exposure. The enhancement can be ascribable to the promotion of columnar growth dependent primarily on film thickness and deposition conditions. (312) diffraction peak of 478.4 nm thickness film can be seen relatively weak and the width is somewhat broadening. This mode is attributed to columnar grain growth and increase of lattice imperfection density. Within an individual phase, the planar grain growth and microstrain accumulation are attributed to the peak broadening/lowing. This behavior is in agreement with the AFM characterization where bigger surface roughness and higher RMS value are reported for laser treated samples. The laser induced crystallite growth points towards a thermally assisted molecular rearrangement, rather than a phase

transition maintaining the intrinsic CuPc crystal structure but with better long-range order. The micro-strain (ε) can be obtained from the XRD data in the table using the positive intercept of a linear fit to RMS value according to simplified Williamson-Hall equation Eq. (5) [21] was utilized. This method allows a full characterization of distortions in the film lattices and provides insight into the structural modifications promoted by the processing conditions.

$$\varepsilon = \frac{\beta \cos\theta}{4} \quad (5)$$

The micro-strain (ε) can be obtained from the XRD data in the table using the positive intercept of a linear relationship according to simplified Williamson-Hall equation Eq. (5) [22] was utilized. This method allows a full characterization of distortions in the film lattices and provides insight into the structural modifications promoted by the processing conditions.

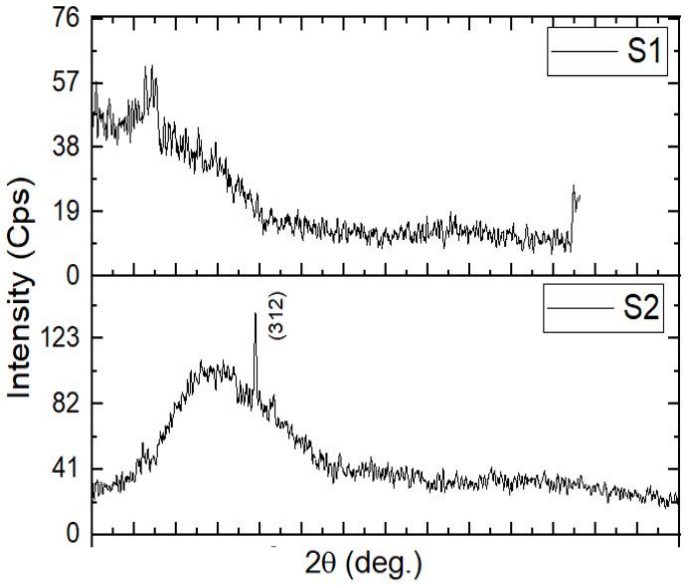

Fig. 3: X-ray diffraction patterns of CuPc thin film grown on a glass substrate at room temperature by thermal evaporation method for S1 and S2

Table 2. Results acquired from X-ray diffraction for copper phthalocyanine films of S1 and S2

Sample	2θ (Deg.)	FWHM (Deg.)	D (nm)	ε	hkl
S1	29.15	0.27	30.47674	$1.1*10^{-3}$	312
S2	29.474	0.211	39.02734	$8.8*10^{-4}$	312

3.3. Atomic force microscopy analysis

AFM is the most reliable surface imaging technique, which provides a three-dimensional representation of nanoscale topography [23]. This allows an analysis of roughness, morphological, and crystal growth information on the CuPc layers before- as well as post-processing. In-situ characterization of surface evolution processes and the processed induced impact on film optical and electrical properties can be accomplished through AFM. Table (3) shows the surface morphological parameters of the CuPc thin films from and respectively.

The average grain diameter (Avg. D) of the as-deposited film is 35.77 nm, which implies that the small gain with a less ordered surface. Once the film is irradiated by laser, average grain size becomes notably larger stirring to be 95.19 nm, so that the energy of laser is able to induce grain growth and molecular rearrangement in the film. The root-mean-square (RMS) roughness, indicating the height difference over the surface, reduces from 169.2 nm in the as-deposited film to 109.4 nm upon laser irradiation. This decrease may be attributed to the smoothly uniform surface topography presumably realized by local melting or re-arrangement due to irradiation of the laser. The value of the Sa is significantly reduced after laser exposure from an average of 145.2 to 68.64 nm. The strong decrease in RMS and Sa values reveals that laser therapy smoothens the surfaces and reduces topography variations, shown in Figures 4 and 5.

Table 3. Values of Avg.D, (Sq), (Sa) of (CuPc) nanostructure of the temperature (R.T), and values of S1and S2

Sample	Avg.D	RMS (Sq)nm	Roughness (Sa)nm
S1	35.77	169.2	145.2
S2	95.19	109.4	68.64

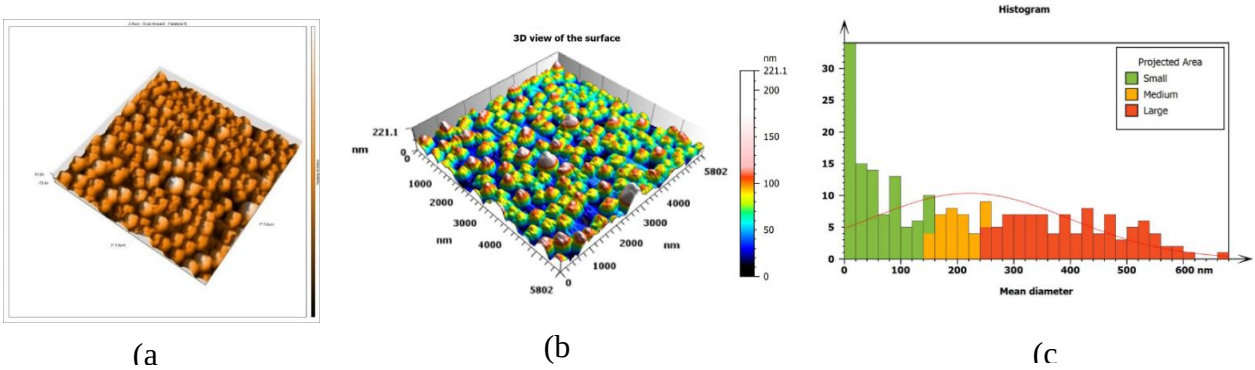

(a (b (c

Fig. 4: AFM analysis for CuPc thin film (a) 2D image, (b) 3D image, and (c) granularity distribution diagrams at S1.

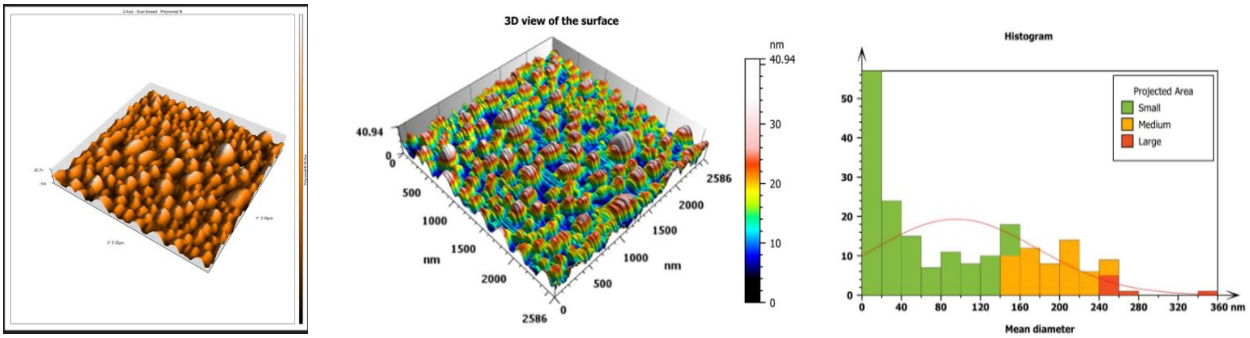

(a (b (c

Fig. 5: AFM analysis for CuPc thin film (a) 2D image, (b) 3D image, and (c) granularity distribution diagrams at S2

3.4. UV- visible analysis

Thermally evaporated CuPc thin films exhibit a noticeable modification in their optical absorption behavior following laser 650 nm treatment. Figure (6) illustrates the UV–Vis absorbance spectra of CuPc thin films before and after exposure to 650 nm laser irradiation. The spectra display the characteristic absorption features of metal–phthalocyanine compounds, namely the B-band (Soret band) in the near-UV region and the Q-band in the visible region, both of which arise from π–π* electronic transitions within the conjugated macrocyclic structure of CuPc. For the as-prepared film (t = 478.4 nm), the Q-band exhibits two well-defined components corresponding to the first and second π–π* transitions, located around ~670 nm and ~610 nm, respectively[24]. These peaks reflect strong molecular ordering and a high level of electronic coupling between CuPc molecules. A significant decrease in the absorbance intensity of Q-band, as well as a small broadening of peaks under laser excitation, was observed under 650 nm laser irradiation.

This decrease in intensity implies that changes in molecular structure may occur upon femtosecond laser irradiation, or a partial shift of electronic states causes recoiling. The movement and broadening of the π–π* transitions imply a change in intermolecular interactions, which may be caused by grain growth, smooth surface, or local heating effects that modify the stacking mode of CuPc molecules. And the B-band in the UV range is another peak that exhibits a drop of absorbance after laser irradiation, which can indicate that there is a shift of optical properties of the thin film. Lowering relative intensities in both the Q- and B-bands indicates that a lower transition probability is involved, which may arise due to reduced disorder and improved surface uniformity (values are consistent with AFM and XRD).

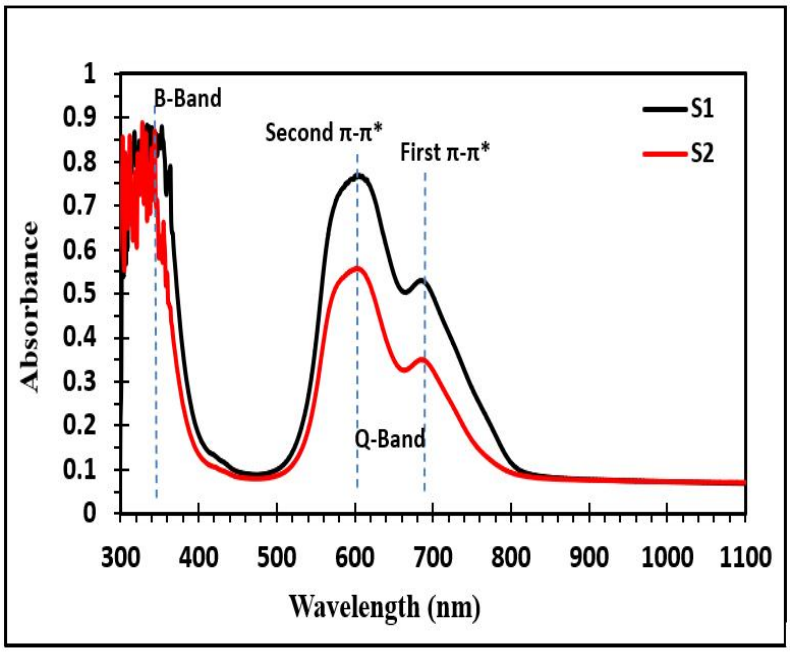

Fig. 6: Absorbance as a function of wavelength for CuPc thin films of S1 and S2 at ambient temperature

Table 4 shows the bandgap optical (Eg) for CuPc thin films before and after laser irradiation at 650 nm. The as-prepared film possesses a bandgap of 1.82 eV, typical for metal–phthalocyanine semiconductors and indicative of their molecular π–π* transition architecture. The bandgap is 1.84 eV on laser treatment. While the effect isn't large, this slight broadening of the optical band gap could result from to laser-

driven changes in the molecular packing and surface structure. The enhanced crystallinity and decreased microstrain in the XRD pattern, together with a smoother surface topology of AFM measurement, could give rise to modified intermolecular interactions due to character variation at grain boundaries, causing anelectronic energy levels shift slightly.

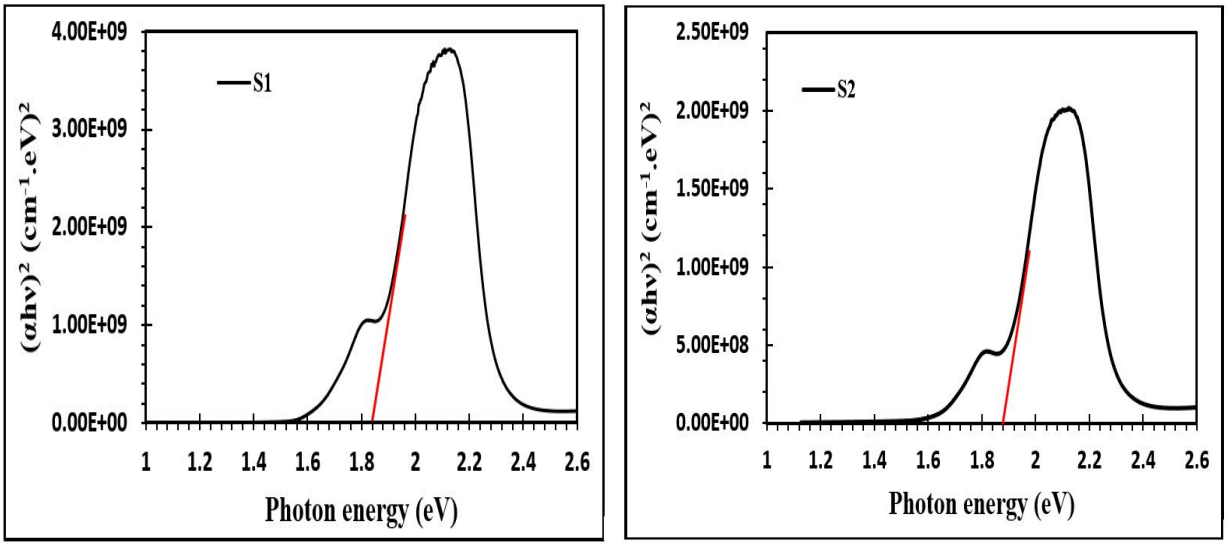

Fig. 7: The band gap of CuPc thin films deposited at S1 and S2 at ambient temperature

Table 4. The band gaps of thickness 478.4 nm and treatment with a laser at 650 nm at ambient temperature.

Sample	Eg (eV)
S1	1.82
S2	1.84

3.5. I-V characteristics

With the bias swept from -5 to +5 V in steps of 0.1 V over an active device area of 1 cm². The dark current subtracted from the gross measured current gives the net photocurrent, given by Eq. (6) [21].

$$I_{ph} = I_{light} - I_{dark} \quad (6)$$

Here, I_{ph} is the photocurrent in the presence of light illumination, P signifies the incident optical power, and A represents the active area of the detector. Remarkably, the dark current is much smaller than the photocurrent, which implies weak leakage without illumination. Furthermore, the good contact electrode quality also contributes to an effective extraction of photo-generated carriers from CuPc thin films into the external circuit, which has a direct impact on device performance. Figure (8) shows the I–V curves of CuPc-based photodetectors obtained in the dark and under illumination with two different samples. In all cases, the presence of a separation between dark current (I_{dark}) and photocurrent (I_{light}) indicates photoconductive response in the CuPc thin films.

In Figure (8a) for the as-prepared CuPc film, the I–V characteristics show almost linear-symmetric behavior of I–V curves, which reveals Ohmic-type contacts between electrodes and organic layer. The photocurrent is significantly higher than the dark current in the entire protocol of applied voltages, indicating efficient photogeneration and conduction of charge carriers [25]. Dark current is very small (low intrinsic leakage), which is important for photodetectors. Upon laser treatment with the 650 nm (Figure (8b)) I–V curves reveal an increase in both photocurrent and dark current. The higher photocurrent intensity under illumination signifies enhanced photoconductive performance, possibly due to laser-induced structural changes (increased crystallinity, decreased microstrain, and better carrier mobility), which are consistent with XRD, AFM, and Hall measurements.

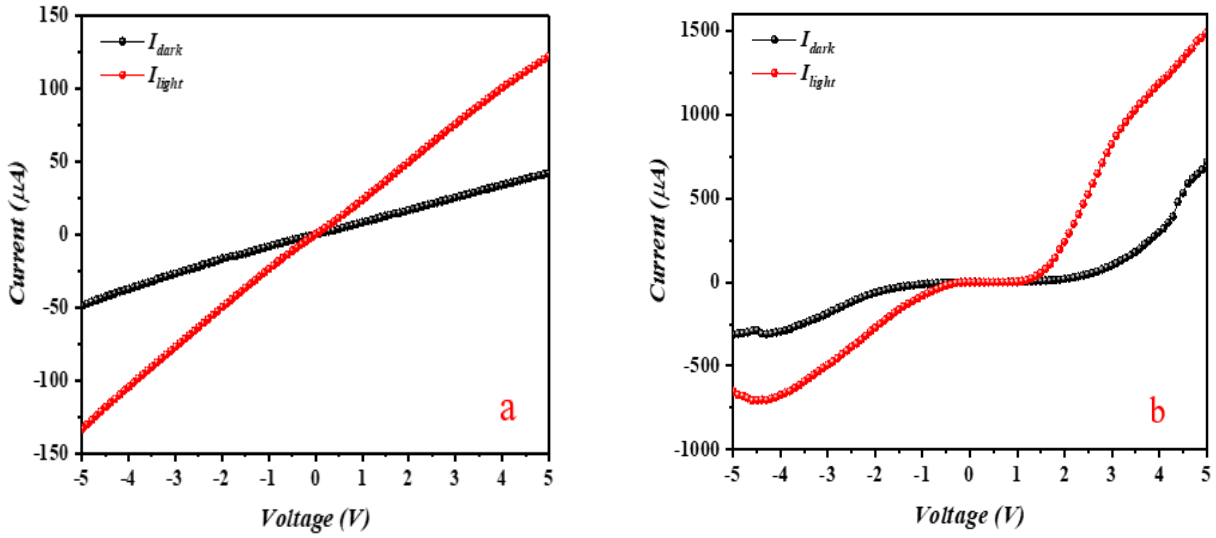

Fig. 8: (a) IV curves of S1 and (b) S2 in dark state and illuminated condition.

This dependence becomes clear when the difference between *I* light and *I* dark increases, indicating that the material has superior performance for photosensing applications. In particular, the thickness-dependent photoresponse properties of CuPc (responsivity R, specific detectivity D* in Eq. (7), (8), and (9) [21], and external quantum efficiency EQE) were systematically measured and their relation to surface morphology determined by AFM. This strategy delivers a systematic insight into the correlations between structural and morphological characteristics and the optoelectronic performance of the device.

$$R = \frac{I_{ph}}{PA} \quad (7)$$

$$D^* = \frac{R.\sqrt{A}}{\sqrt{2qI_D}} \quad (8)$$

$$EQE = \frac{I/q}{P/h\nu} \quad (9)$$

The most relevant photoresponse parameters of the CuPc photodetectors (responsivity, R; detectivity, D*; external quantum efficiency, EQE; and temporal response times, Trise and Tfall) as displayed in Table 8, were obtained for both the pristine and laser-irradiated films at a wavelength of 625 nm. The as-prepared CuPc film (t = 478.4 nm) possesses a responsivity of 54.92 μA/mW, detectivity of 19.3 × 10^9 Jones, and

EQE of 10.89%. These values evidence a moderate photosensing behaviour, which agrees with the standard performance of organic photodetectors using phthalocyanine materials as the active layer. The significantly improved photoresponse of the device is faster with 650 nm light illumination. We observe that responsivity rises more than three times to be 190.98 μA/mW, indicating a far higher photocurrent generation under illumination. Similarly, detectivity can be enhanced to 33.8 × 10^9 Jones which demonstrates better performance of distinguishing weak optical signals from noise. This enhancement is due to the laser-induced improvement in film crystallinity, carrier mobility and reduction of surface roughness as evidenced by XRD and AFM measurements. Meanwhile, the EQE also reveals an obvious enhancement from 10.89% to 37.89% after laser treatment, further indicating the enhanced efficiency of transforming incident photons into charge carriers. This enhancement indicates the promoted optoelectronics property of the CuPc film with structural modification through laser treatment. In terms of the temporal response both the rise time (Trise) rises from 0.30 s to 0.63 s and the fall time (Tfall) falls slightly from 0.31 s to 0.29 s, which can imply that there is a slower trap-assisted process or carrier accumulation in the laser-treated film while at same time making recombination or trapped carrier release more efficient upon end of illumination.

Table 5. Parameters of the photo detector CuPc thin film with 625 nm for S1 and S2

Sample	Responsivity (μA/mW) λ (625 nm)	Detectivity × 10^9 (Jones) λ (625 nm)	EQE (%) λ (625 nm)	T_{rise} (sec.)	T_{fall} (sec.)
S1	54.92	19.3	10.89	0.30	0.31
S2	190.98	33.8	37.89	0.63	0.29

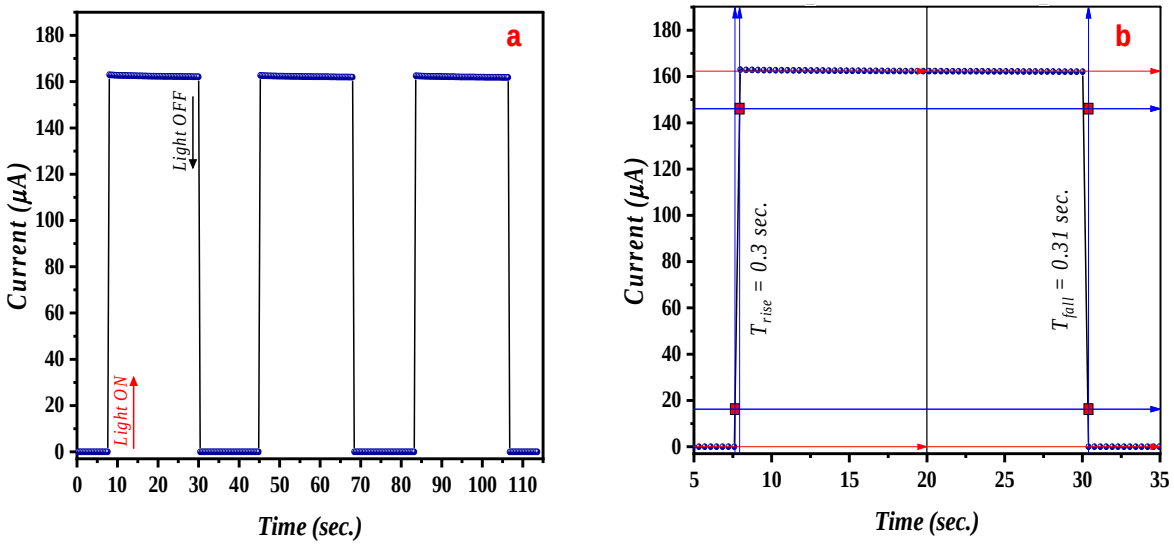

Fig. 9: (a) Time-dependent photocurrent response of CuPc photodetector; (b) Peak photocurrent of different light on-off cycles with S1

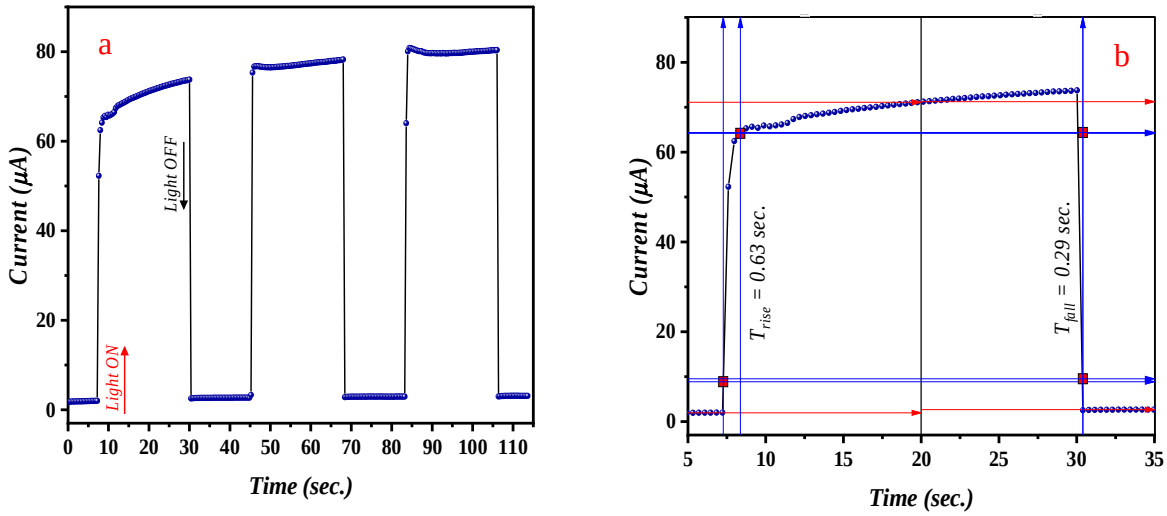

Fig. 10: (a) Time-dependent photocurrent response of CuPc photodetector; (b) Peak photocurrent of different light on-off cycles with S2.

4. Conclusion

This study shows that 650 nm laser irradiation is an effective and non-destructive post-treatment technique to modulate the optoelectronic properties of copper phthalocyanine (CuPc) thin films. The crystalline, grain size, and surface roughness are improved as a result of the laser treatment due to better molecular order and reduced structural defects. Such changes lead to a slight red shift of the optical band gap and a strong improvement in carrier mobility. As a result, the responsivity, detectivity, and external quantum efficiency of the CuPc-based photodetectors based on laser-treated films are greatly improved with stable photoresponse. In general, controlled laser irradiation provides a simple and powerful method for tuning CuPc thin films toward high-quality organic optoelectronic devices.

References

[1] R. Gomez, F. Souza, and R. Lima, "Development of High-performance Organic Semiconductors for Flexible Electronics", Research of Scientia Naturalis, 1, 195-205 (2024), https://doi.org/10.70177/scientia.v1i4.1574.
[2] F. Ding, D. Xue, L. Chi, and L. Huang, "Organic Phototransistor Photonic Synapses for Artificial Vision", Nano-Micro Letters, 18, 203 (2026), https://doi.org/10.1007/s40820-025-02036-0.
[3] Z. J. Abd Al-Kareem and E. T. Abdullah, "Laser-Ablated Silver Nanoparticles Embedded in P3HT: A Study of Structural and Optical Enhancement", Iraqi Journal of Laser, 24, 74-82 (2025), https://doi.org/10.31900/ijl.v24i2.541.
[4] A. M. Schmidt and M. J. Calvete, "Phthalocyanines: an old dog can still have new (photo) tricks!", Molecules, 26, 2823 (2021), https://doi.org/10.3390/molecules26092823.
[5] A. A. A., G. S. R., A. H. M., M. El-Nahass, and F. S. Bahabri, "Structural and Transport Properties of Copper Phthalocyanine (CuPc) Thin Films", Egypt. J. Sol., 25, 307–321 (2020), https://doi.org/10.1016/j.tsf.2020.138250.
[6] A. Nadeem and M. Daoud, "Optical characterization of CuPc thin films", Opt. Mater., 36, 1120–1126 (2014), https://doi.org/10.1016/j.optmat.2014.01.031.
[7] M. A. Osman et al., "Laser-induced modification of organic semiconductor thin films", Appl. Surf. Sci., 427, 1160–1167 (2018), https://doi.org/10.1016/j.apsusc.2017.12.155.
[8] M. Feltri et al., "Laser processing of functional thin films", Appl. Phys. A, 123 (2017),

https://doi.org/10.1007/s00339-017-0942-4.
[9] Z. M. Hassan and A. F. Abdulameer, "Structural and Morphological Properties of as-Deposited and Heat-Treated Composite (CuPc/Alq3) Thin Films", Iraqi J. Sci., 1717–1727 (2023), https://doi.org/10.24996/ijs.2023.64.4.13.
[10] J. Ihlemann et al., "Photothermal and photochemical modification of organic thin films", Appl. Phys. A, 122 (2016), https://doi.org/10.1007/s00339-016-9694-8.
[11] M. T. Hussein, K. A. Aadim, and E. K. Hassan, "Structural and Surface Morphology Analysis of Copper Phthalocyanine Thin Film Prepared by Pulsed Laser Deposition and Thermal Evaporation Techniques", Adv. Mater. Phys. Chem., 6, 85–97 (2016), https://doi.org/10.4236/ampc.2016.64009.
[12] J. Malinowski et al., "Influence of laser irradiation on organic thin-film transistors", Org. Electron., 15, 2220–2227 (2014), https://doi.org/10.1016/j.orgel.2014.05.030.
[13] A. E. Yakimov and S. R. Forrest, "Laser crystallization of organic films", Phys. Rev. B (2002), https://doi.org/10.1103/PhysRevB.65.081306.
[14] M. K. Sørensen et al., "Manipulating Organic Semiconductor Morphology with Visible Light", 2212835, 1–10 (2023), https://doi.org/10.1002/adfm.202212835.
[15] V. Korede et al., "A Review of Laser-Induced Crystallization from Solution", (2023), https://doi.org/10.1021/acs.cgd.2c01526.
[16] Y. Shimizu et al., "Photophysical interactions in laser-treated CuPc thin films", Thin Solid Films (2016), https://doi.org/10.1016/j.tsf.2015.10.09.
[17] H. Lee and J. Kim, "Advances in Near-Infrared Organic Photodetectors: Molecular Design, Exciton Dynamics, and Device Integration", (2026), https://doi.org/10.3390/polym18020201.
[18] S. F. Madlul, N. K. Mahan, E. M. Ali, and A. N. Abd, "Synthesis of CdS:Cu5% thin films by chemical method based on silicon for gas sensor applications", Mater. Today Proc., 45, 5800–5803 (2021), https://doi.org/10.1016/j.matpr.2021.03.170.
[19] N. K. A, O. A. Fahad, and K. A. Khalaph, "Effect of Pulsed Laser Frequency on CdTe Deposited as Solar Cells Device", Int. J. Nanosci., 21, 1–8 (2022), https://doi.org/10.1142/S0219581X21500629.
[20] Z. Hazim A. Raheem, "Effect of SnO_2/In_2O_3 Atomic Ratio on the Structural and Optical Properties of ITO Thin Films", Baghdad Sci. J., 18, 393–400 (2021), https://doi.org/10.21123/bsj.2021.18.2.0393.
[21] M. A. Nawaz et al., "Microstructural study of as grown and 650 °C annealed ZnO nanorods: X-ray peak profile analysis", Dig. J. Nanomater. Biostructures, 11, 537–546 (2016).
[22] H. Ali, Y. Zhang, J. Tang, and X. Xu, "High-Responsivity Photodetection by a Self-Catalyzed Phase-Pure p-GaAs Nanowire", Small, 14, 1–9 (2018), https://doi.org/10.1002/smll.201704429.
[23] L. Mei and G. Guan, "Profilometry and atomic force microscopy for surface characterization", 2, 69–73 (2023), https://doi.org/10.26599/NTM.2023.9130017.
[24] M. T. H. Reem R. Mohammed, "Linear and Non-Linear Optical Properties for Organic Semiconductor (CuPc) Thin Films", 10–20 (2021), https://doi.org/10.30723/ijp.19.48.10-20.
[25] T. Elmore, J. Candler, F. Yakuphanoglu, and R. K. Gupta, "Carrier Transport Mechanism of Copper Phthalocyanine Based Photodiode for Solar Cell Applications", 18–23 (2015).

تأثير معالجة الإشعاع الليزري على البنية النانوية لمركب فيثالوسيانين النحاس وتطبيقاته الكهروضوئية

زينب حازم عبدالرحيم[1,*]، محمد خماس خلف[2]، سمير خضر ياسين[1]

[1] قسم الفيزياء، كلية علوم بنات، جامعة بغداد، بغداد، العراق

[2] هيئة البحث العلمي، بغداد، العراق

البريد الالكتروني للباحث: zainab.h@csw.uobaghdad.edu.iq

الخلاصة: تظهر أغشية فثالوسيانين النحاس (CuPc) امتصاصا قويا للضوء المرئي، فضلا عن استقرارها الكيميائي، مما يجعلها أشباه موصلات عضوية جذابة للأجهزة الكهروضوئية. في هذه الدراسة، بحثنا تأثير تشعيع الليزر بطول موجي 650 نانومتر على غشاء رقيق من CuPc بسمك 478.4 نانومتر، وسجلنا سلوكه ككاشف ضوئي. أظهر تحليل حيود الأشعة السينية زيادة في بلورية العينات المعالجة بالليزر، حيث ازداد حجم البلورات من 30.48 إلى 39.03 نانومتر مع انخفاض في الإجهادات الميكروية. كما ازداد متوسط حجم الحبيبات من 35.77 إلى 95.19 نانومتر، بينما انخفضت خشونة السطح كما لوحظ بواسطة مجهر القوة الذرية (AFM)، مما يدل على نمو ملحوظ للحبيبات وعملية تنعيم السطح. أظهرت الخصائص البصرية تغيرات طفيفة في انتقالات π–π* وزيادة طفيفة في فجوة النطاق البصري من 1.82 إلى 1.84 إلكترون فولت، مما يشير إلى انخفاض في الاضطراب البنيوي. وكشفت قياسات تأثير هول أن زيادة حركة حاملات الشحنة من 0.16 إلى 28.9 سم^2/فولت.ثانية أدت إلى خصائص كهربائية جيدة على الرغم من انخفاض قيمة n نتيجة لآلية تعويض الثقوب. في الوقت نفسه، تحسنت استجابة كاشف الضوء CuPc المعالج بالليزر بشكل ملحوظ من 54.92 إلى 190.98 ميكروأمبير/مللي واط، كما زادت الكفاءة الكمية الخارجية من 10.89% إلى 37.89% عند طول موجي 625 نانومتر. تعزى هذه التحسينات إلى إعادة تنظيم الجزيئات بفعل الليزر، وانخفاض كثافة المصائد، وتحسين مسار نقل الشحنة.

IJL, Vol. 25, Issue1, 2026
http://doi.org/10.31900/ijl.v25i1.557

Research Article

IRAQI JOURNAL OF LASER

Clinical efficacy of Diode Laser in Oral Pyogenic Granuloma

Ayman A. Najim*, Tahrir N. Aldelaimi

Oral and maxillofacial surgery department, College of dentistry, University of Anbar, Ramadi-Anbar province, Iraq.
**Email address of the corresponding author: aymanadnan.n.a@gmail.com*

Article history: Received 27 Dec. 2025, Accepted 28 Mar. 2026, Published online 15 Jun. 2026.

Abstract: Oral pyogenic granuloma (PG) is a benign but very vascular lesion that causes discomfort and bleeding. Conventional surgical excision is effective but has a high recurrence rate and postoperative pain. Diode laser excision is a less invasive procedure that offers precise tissue removal and better hemostasis. Our Objective is to evaluate the safety and efficacy of diode laser excision for the treatment of oral pyogenic granuloma. A total of sixteen patients (mean age 39.3; age range 15 - 74 years; 11 males and 5 females) with de novo oral PG were enrolled and all lesions were removed under local anesthesia using a continuous 1.5 W 980 nm diode laser with minimal bleeding, without the need for sutures and a 0.5 mm safety margin was kept. Patients were evaluated at one week and three weeks after surgery and on postoperative days one and three. Wound healing, hemostasis, pain and satisfaction were all assessed on every visit. The excised tissues were confirmed histopathologically. The diode laser provided better control over intraoperative bleeding, as any small amount of bleeding was easily controlled. Pain settled rapidly, as the majority of patients were comfortable by day three and completely pain-free within one week. The healing process progressed quickly, with satisfactory to excellent results by one week and full recovery by three. Nearly all patients expressed high satisfaction at the last follow-up. Diode laser excision is a safe and efficient treatment for oral PG that provides excellent hemostasis, less discomfort following surgery, quick healing, and high patient satisfaction. These findings corroborate the reliable clinical results of diode laser excision in current standard treatment.

Keywords: pyogenic granuloma, diode laser, benign tumor, laser surgery, oral swelling.

1. Introduction

Oral pyogenic granuloma is a benign proliferation of connective tissue characterized by excessive granulation tissue formation that most commonly affects the skin and mucosal surfaces, although it has been occasionally reported in subcutaneous tissues, intravascular locations, and rarely within the gastrointestinal tract. The etiopathogenesis of oral PG remains controversial and multifactorial; in some studies, it has an infectious origin, mainly related to the presence of staphylococci, streptococci, and other oral microorganisms in the case of ulcerated lesions, although their detection close to the surface of the lesion is often considered as secondary to contamination from the oral flora rather than a primary cause [1,2,3]. On the other hand, it is described by many authors as a reactive or reparative lesion that can be triggered by minor trauma, chronic irritation, and the presence of foreign bodies such as calculus, leading

to an excessive connective tissue proliferation [4, 5]. Trauma is widely recognized as a key factor that triggers the release of angiogenic mediators such as bFGF, which stimulate endothelial proliferation and angiogenesis during the granulation tissue formation [6, 2]. Clinically, oral PG typically presents as a soft, exophytic, pedunculated mass covered by a smooth, shiny mucosal surface. The lesion is highly vascular and bleeds easily even with minor trauma. In some cases, it may present as a sessile plaque rather than a pedunculated growth [8].

These lesions are generally painless and range in size from a few millimeters to several centimeters, often reaching their maximum dimensions within a few weeks to months, Jafarzadeh H [5]. Approximately 75% of oral PGs occur on the gingiva, most frequently in the interdental papilla of the maxillary anterior region, although other intraoral sites such as the lips, tongue, buccal mucosa, and palate may also be affected as seen by Regu P [9]. Lasers have emerged as one of the most impactful tools in modern dentistry, offering precision, control, and operative benefits that traditional scalpels often cannot match. By converting light energy into a highly focused beam, lasers can cut, ablate, or coagulate tissues with minimal trauma to surrounding structure as illustrated by Bernaola-Paredes WE [10]. This technology has the advantages of providing excellent hemostasis, reducing intraoperative pain, promoting faster postoperative recovery, giving the patient overall more comfort, all the qualities of great value, especially in oral surgery, where visibility and patient comfort are important [11]. Diode laser in oral surgery has certain advantages over conventional methods and other laser types, providing a precise, bloodless incision with excellent hemostasis without the need for sutures, minimizing postoperative pain, swelling, and scarring, and faster healing by secondary intention [12, 13].

The diode system is more compact, cost-effective, and easy to maneuver than CO2 and erbium lasers, which makes it particularly well-suited to be used in routine clinical practice and as applied to the treatment of oral pyogenic granuloma, a benign but very vascular lesion that can cause discomfort, bleeding, and aesthetic concerns it brings distinct advantages. The inherent ability of lasers to seal blood vessels during excision minimizes intraoperative bleeding, thereby improving the surgeon's field of view and shortening operative time as noted by Azma E [12]. Moreover, the reduced mechanical trauma compared to scalpel surgery may lower recurrence rates, improve healing profiles, and enhance cosmetic outcomes in delicate oral tissues as demonstrated by Khan MK [14].

2. Materials and Methods

This prospective study was conducted in oral and maxillofacial department of Ramadi teaching hospital and oral and maxillofacial department of college of dentistry in university of Anbar, Anbar province, Iraq. The study included 16 participants: 11 males (=69 %) and 5 females (= 31%), aged 15 to 74 years (mean=39.31). All the participants had to meet a certain criteria before inclusion in the study, they must have de novo Pyogenic granuloma (not recurred) in any oral site, have no systemic disease that compromise the healing process or any condition that preclude laser use. A diode laser (Biolase, USA) of a wavelength 980/810nm was used with power output of 1.5 Watts delivered through a 400um fiber optic cable with an FC connecter operating in continuous mode, both operator and patient were protected with laser goggles. Demographic and clinical data, including age, gender, medical and dental history, were documented. The surgical procedure was fairly explained to the patients and all patients signed consent form before operation. Pre-operative patient preparation included antimicrobial mouth wash and gowning. Local anesthesia technique was either Buccal and mental nerve block (lower gingiva), lingual nerve block (lateral tongue border) or infiltration (upper gingiva and tip of the tongue) using 2.2ml cartridge containing 2% lidocaine and 1:80.000 epinephrine. The margin of the lesion was outlined by simultaneous dual wavelength 980/810nm diode laser using repetitive strokes. The outline was 0.5 mm behind the lesion margin, and careful grasping of the lesion was performed during surgery by tissue forceps to avoid bleeding and tearing of tissue. Much attention was paid to lesion excision to prevent deterioration of the underling minor salivary glands. Following the outlined lesion margins, the lesion was excised with diode laser at 1.5W output and then elevated, the surgical site is left uncovered and un-

sutured as in (Figure 1), post-operative instructions were clarified to the patients, which focused on meticulous oral hygiene and avoiding trauma to the surgical site.

Clinical assessments were conducted to determine intraoperative bleeding and scored as: no bleeding=1, mild bleeding=2 (oozing requiring pressure), moderate bleeding=3 (requiring local hemostatic agents), severe bleeding=4 (requiring ligation). For pain and healing measurements, all the patients were assessed at fixed intervals postoperatively as follows, Day 1, Day 3, Week 1, Week 3. The intensity of pain was measured using verbal pain scale and expressed as: no pain=0, mild pain=1, moderate pain=2, severe pain=3. Tissue healing was assessed using the Landry, Turnbull, and Howley Healing Index. The scores are defined as follows: Score 1 – Very poor healing: Tissue color: ≥ 50% red, Bleeding on palpation: present, Granulation tissue: present, Epithelialization: absent. Score 2 – Poor healing: Tissue color: ≥ 50% red, Bleeding on palpation: present, Granulation tissue: present, Epithelialization: minimal. Score 3 – Good healing: Tissue color: ≥ 25% red, Bleeding on palpation: absent, Granulation tissue: absent, Epithelialization: present. Score 4 – Very good healing: Tissue color: < 25% red, Bleeding on palpation: absent, Granulation tissue: absent Epithelialization: complete. Score 5 – Excellent healing: Tissue color: pink (normal) Bleeding on palpation: absent, Granulation tissue: absent, Epithelialization: complete.

All the samples in this study were put in 10% formalin plastic container and sent to histopathological examination for confirmation of diagnosis of pyogenic granuloma.

2.1 Statistical analysis

Data are presented as mean ranks and other descriptive statistics. Differences in intensity across the tested factors and follow-up time points were assessed using the Friedman test, a nonparametric alternative to repeated-measures ANOVA. Post hoc pairwise comparisons were performed using the Wilcoxon signed-rank test. Values of $p > 0.05$ were considered statistically nonsignificant, while $p \leq 0.05$ was considered significantly different. Statistical analysis was carried out using SPSS (v 20).

3. Results and discussion

Out of the total 16 documented cases, the upper gingiva was identified as the most frequently affected oral site, accounting for 5 cases. This was followed by the lower gingiva, where 4 cases were recorded. The dorsum of the tongue showed involvement in 3 cases, while the lateral border of the tongue and the lower lip were less commonly affected, with 2 cases each reported for both sites as shown in (Figure 2). Bleeding control during surgery worked well. 12 patients (75%) had no bleeding at all, showing just how effective the diode laser was at stopping blood flow. Of the remaining patients, three (18.8%) had mild bleeding that was easily managed with simple pressure, while one patient (6.2%) had moderate bleeding that was successfully controlled using the laser for coagulation. We followed the patients prospectively to track their pain levels from day one up to three weeks after surgery. The results showed pain scores dropping significantly as time went on. Statistical analysis using the Friedman test revealed a significant difference in pain across the follow-up periods ($\chi^2 = 35.629$, $p < 0.0001$) and effect size was calculated using Kendall's W at W=0.113, indicating small effect size all presented in (Table 1).

Further testing with Wilcoxon signed-rank tests confirmed that pain decreased significantly between each successive checkpoint. Interestingly, we found no real difference in pain between the first and third weeks, though pain intensity differed significantly at other measured time points as outlined in (Table 2). We also tracked how well patients healed during the same follow-up period, from the first day through the end of week three. The Friedman test showed highly significant results ($\chi^2 = 45.73$, $p < 0.0001$), Kendall' W effect size was W=0.143, indicating a small effect size as displayed in (Table 3). Wilcoxon signed-rank tests showed notable improvements in healing scores from one point to the next. Overall, our findings revealed highly significant improvements in recovery as time progressed [15], in which (Table 4) clearly illustrates. When it came to patient satisfaction on surgery day, most patients felt quite positive about their experience, with 10 patients rating it as good, and 4 patients calling it excellent, and only 2

patients saying fair or poor. By the next day, no patients reported poor outcomes, and most continued to rate the procedure as good (10 patients) or excellent (3 patients).

After three days, satisfaction shifted further toward excellent ratings (9 patients), with only a few remaining in the fair or good categories. By the end of the first week, all patients reported either good or excellent satisfaction, with most leaning toward excellent (11 patients). At the three-week follow-up, nearly all patients rated their satisfaction as excellent, with only a small minority describing it as good (2 patients) as shown in (Figure 3)**.** The therapeutic efficacy of diode laser in the management of oral pyogenic granuloma is rooted in its photothermal mechanism of action, whereby laser energy emitted in the near-infrared spectrum (810–980 nm) is selectively absorbed by tissue chromophores principally oxyhemoglobin and melanin and converted into heat, producing temperature-dependent tissue effects [16,17]. What distinguishes this mechanism clinically is its inherent dose-dependence: at sub-ablative thermal thresholds, the resultant heat stimulates fibroblast activity and collagen remodeling through photobiomodulation pathways, while supra-lethal doses achieve coagulative necrosis and tissue vaporization [18, 19].

This biological duality is central to understanding both the appeal and the demands of diode laser surgery the same energy source that enables precise, bloodless excision can, if inadequately controlled, generate collateral thermal injury that compromises wound healing. It is worth noting that consensus on optimal laser parameters for pyogenic granuloma excision has not yet been established in the literature, and this methodological heterogeneity should be borne in mind when comparing outcomes across studies [18,19,20]. From a clinical standpoint, the advantages of laser-assisted excision over conventional cold blade surgery are well-grounded in these tissue-level mechanisms. Continuous photocoagulation of the lesion's feeding vessels during advancement of the fiber tip accounts for the superior intraoperative hemostasis that is consistently reported with diode laser use. Reduced mechanical traction on surrounding tissue minimizes collateral damage, while the bactericidal properties of the laser energy lower microbial contamination at the wound surface, a relevant consideration given the inflammatory microenvironment of pyogenic granuloma. Sealing of peripheral sensory nerve endings attenuates postoperative pain, and the combination of these effects typically results in cleaner wound healing, improved aesthetic outcomes, and elimination of the need for sutures in many cases [18, 19, 20].

The findings of the present study are broadly concordant with this body of evidence. Intraoperative hemostasis was consistently excellent, a finding of particular clinical relevance in patients with medical comorbidities predisposing to bleeding complications. Pain intensity showed a progressive and marked reduction across postoperative follow-up intervals, consistent with the conservative nature of laser tissue interaction. Wound healing assessments at one week demonstrated good-to-excellent outcomes in the majority of patients, and overall satisfaction already favorable on the day of surgery was sustained at subsequent follow-up visits. These results support the efficacy and safety of the diode laser protocol employed in this study and are in agreement with comparable single-arm and controlled investigations reported in the literature. However, intellectual honesty demands that these favorable findings be situated within a broader and more critical comparative context. A randomized controlled trial by Anwar et al. comparing diode laser with ethanolamine oleate sclerotherapy in 20 patients with oral pyogenic granuloma yielded findings that merit careful consideration [15]. Although intraoperative bleeding did not differ significantly between groups, postoperative pain was significantly lower in the sclerotherapy arm, and of greater clinical concern recurrence was documented exclusively among laser-treated patients across all follow-up intervals of three, six, and nine months, with no recurrences recorded in the sclerotherapy group. The authors concluded that sclerotherapy constitutes a simpler, less equipment-dependent modality with a more favorable recurrence profile. These findings do not negate the clinical utility of diode laser, but they underscore the importance of avoiding an uncritical endorsement of any single modality and highlight recurrence as an outcome that warrants close attention in laser-based management of pyogenic granuloma. Conventional surgical excision, while historically regarded as the

treatment of choice, is associated with recognized limitations that provide additional context for evaluating laser-based alternatives.

Recurrence following simple excision particularly when surgical margins are inadequate has been documented by Daif et al. [20] and Al-Noaman [22]. The highly vascular nature of pyogenic granuloma renders cold blade surgery susceptible to significant intraoperative and postoperative hemorrhage [5], and comparative data reported by Khan et al. [23] consistently demonstrate higher postoperative pain scores in patients managed by conventional excision relative to those treated by minimally invasive methods. In this context, diode laser represents a genuine therapeutic advance; yet it is most accurately understood as one modality within a spectrum of options, each carrying distinct trade-offs with respect to cost, equipment requirements, operator expertise, recurrence risk, and patient experience. Randomized controlled trials with larger sample sizes, standardized laser parameters, and extended follow-up periods remain necessary to consolidate the evidence base and guide evidence-informed clinical decision-making.

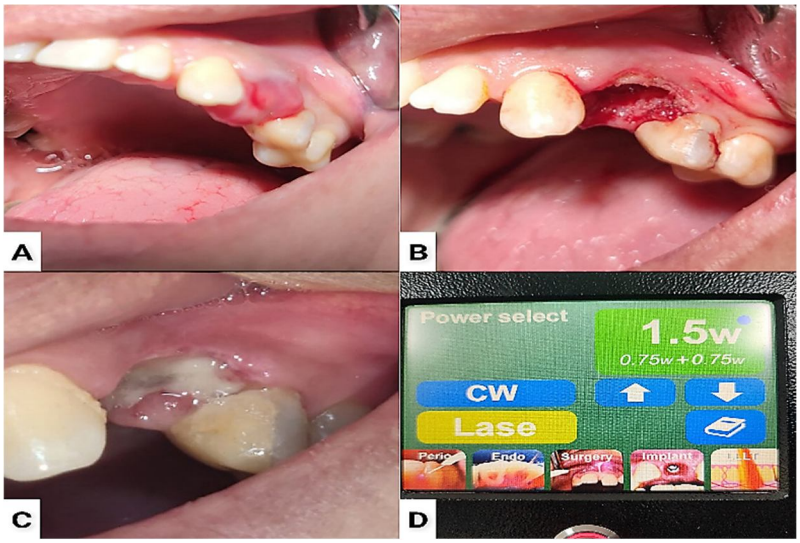

Fig. 1: Diode laser excision of gingival pyogenic granuloma in 30-years old female: (A) Initial situation, (B) immediately post-operative situation, (C) one week following diode laser excision, (D) Laser parameters.

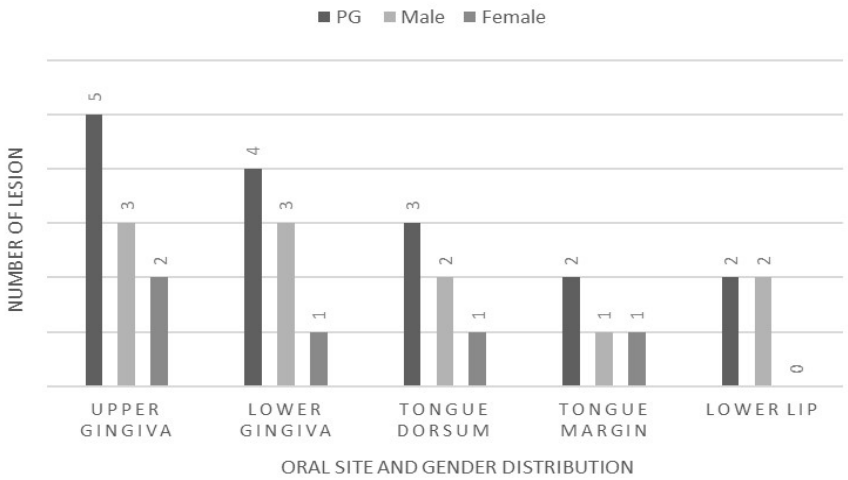

Fig. 2: Distribution of pyogenic granuloma in the oral cavity of male and female patients.

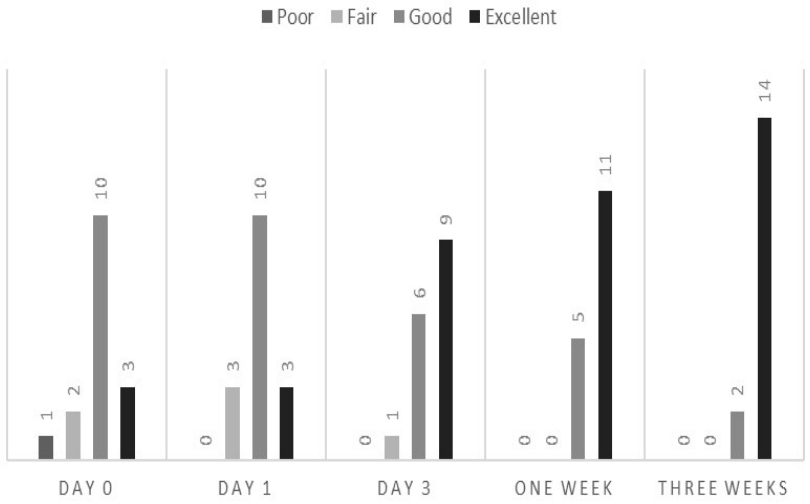

Fig. 3: Satisfaction level during follow-up periods.

Table 1. Statistical analysis of pain score profile across four time periods.

Descriptive Statistics						Friedman Test
Pain durations	N	Mean	Std. Deviation	Minimum	Maximum	Mean ranks
One day	16	1.500	.96609	.00	3.00	3.75
Three days	16	.5625	.72744	.00	2.00	2.56
One week	16	.1250	.34157	.00	1.00	1.91
Three weeks	16	.0000	.00000	.00	.00	1.78
Chi-secure (X^2) 35, 629 P value=0.0001, W=0.113						
The result is significant at p ≤0.05						

Table 2. Comparative statistical analysis of the relationship between pain scores and time.

Wilcoxon Signed Ranks Test						
Pain score	3 days – one day	one week - one day	3 weeks - one day	one week - 3 days	3 weeks - 3 days	3 weeks - one week
Z	-3.217	-3.372	-3.354	-2.646	-2.460	-1.414
Sig. (2-tailed)	0.001	0.001	0.001	0.008	0.014	0.157

Table 3. Statistical analysis of healing score profile across four time periods.

Descriptive Statistics						Friedman Test
Healing durations	N	Mean	Std. Deviation	Minimum	Maximum	Mean ranks
One day	16	1.4375	.51235	1.00	2.00	1.13
Three days	16	2.3750	.61914	1.00	3.00	1.97
One week	16	3.3750	.61914	2.00	4.00	2.94
Three weeks	16	4.5000	.63246	3.00	5.00	3.97
Chi-secure (X^2) =45.73, P value=0.0001, W=0.143						
The result is significant at $p \leq 0.05$						

Table 4. Comparative statistical analysis of the relationship between healing scores and time.

Wilcoxon Signed Ranks Test						
Healing score	3 days – one day	one week - one day	3 weeks - one day	one week - 3 days	3 weeks- 3 days	3 weeks - one week
Z	-3.217	-3.598	-3.624	-3.358	-3.624	-3.626
Sig. (2-tailed)	0.001	0.0001	0.0001	0.001	0.0001	0.0001

4. Conclusion

In this study, good intraoperative hemostasis was achieved following diode laser application avoiding the use of sutures. Post-operative pain was also significantly reduced with excellent healing outcomes, thus the application of diode laser shows favorable results and can be used in the management of oral PG.

Acknowledgment

The authors would like to express their deepest gratitude to all the staff in Ramadi Teaching hospital, department of oral and maxillofacial surgery and all the workers of oral and maxillofacial surgery clinics in college of dentistry, University of Anbar.

Limitations

Lack of patient consistency during follow ups, absence of comparison group, no follow up period to identify recurrences.

Ethics approval and consent for authors

This study was conducted in full accordance with the ethical principles outlined in the Declaration of Helsinki and its subsequent amendments. Ethical approval was obtained from the Ethical Committee at the University of Anbar under Ref 44 on 3/7/2025 prior to the commencement of the study. Written informed consent was obtained from all

participants prior to enrollment, and all patients were assured of their right to withdraw from the study at any time without consequence. Patient data were handled with strict confidentiality throughout all phases of the study.

Author declaration

All authors declare that this work is original and done with full accordance to the declaration of Helsinki and ethical committee guidelines and had not been published nor submitted elsewhere.

Funding

The authors declare there was no external source of funding in this study.

Conflict of interests

The authors declare no conflict of interests

Author contributions

Sample collection, data analysis, surgery, and writing were performed by AAN.
Supervision, conceptualization, and methodology were made by TNA.

References

[1] L. D. Thompson, "Lobular capillary hemangioma (pyogenic granuloma) of the oral cavity," Ear Nose Throat J., 96(7), p. 240 (2017). doi:10.1177/014556131709600716.
[2] D. A. Kerr, "Granuloma pyogenicum," Oral Surg. Oral Med. Oral Pathol., 4(2), pp. 158-176 (1951). doi:10.1016/0030-4220(51)90432-X.
[3] R. Rajendran and B. Sivapathasundharam, Shafer's Textbook of Oral Pathology, 6th ed., Elsevier, New Delhi, pp. 126-130 (2009).
[4] J. Regezi, J. Sciubba, and R. Jordan, Oral Pathology: Clinical Pathologic Correlations, 7th ed., Elsevier/Saunders, St. Louis, p. 118 (2016).
[5] H. Jafarzadeh, M. Sanatkhani, and N. Mohtasham, "Oral pyogenic granuloma: a review," J. Oral Sci., 48(4), pp. 167-175 (2006). doi:10.2334/josnusd.48.167.
[6] M. Murata, K. Hara, and T. Saku, "Dynamic distribution of basic fibroblast growth factor during epulis formation: an immunohistochemical study in an enhanced healing process of the gingiva," J. Oral Pathol. Med., 26(5), pp. 224-232 (1997). doi:10.1111/j.1600-0714.1997.tb01228.x.
[7] S. Daoudi, S. Tabbai, and H. Ramdi, "Oral Pyogenic Granuloma in a Child: Suspected Hormonal and Traumatic Factors, Clinical Features, and Surgical Management," Cureus, 17(5), e84713 (2025). doi:10.7759/cureus.84713.
[8] P. Sarwal and K. Lapumnuaypol, "Pyogenic Granuloma," in StatPearls, StatPearls Publishing, Treasure Island, FL (2025).
[9] P. Regu, S. Aatman, and G. V. Murali, "Pyogenic granuloma of the tongue—a rare clinical finding," Int. J. Dent. Case Rep., 3, pp. 57-61 (2013).
[10] W. E. Bernaola-Paredes, M. B. da Silva Conceição, S. C. Moreira, A. M. A. Souza, P. S. Souza Pina, L. H. Azevedo, et al., "Clinical and histopathological features of congenital epulis in a newborn submitted to laser surgery," J. Oral Maxillofac. Pathol., 26(Suppl. 1), pp. S77-S79 (2022). doi:10.4103/jomfp.jomfp_449_20.
[11] S. Parker, "Laser regulation and safety in general dental practice," Br. Dent. J., 202, pp. 523-532 (2007). doi:10.1038/bdj.2007.370.
[12] E. Azma and N. Safavi, "Diode laser application in soft tissue oral surgery," J. Lasers Med. Sci., 4(4), pp. 206-211 (2013).
[13] D. De Falco, D. Di Venere, and E. Maiorano, "An overview of diode laser-assisted oral surgery," Cureus, 12(7), e9297 (2020).

[14] M. K. Khan and M. K. Jindal, "Diode laser as minimal invasive treatment modality for oral pyogenic granuloma in a pediatric patient: A case report," J. Pediatr. Dent., 7(3), p. 178 (2021).
[15] S. K. Anwar, S. N. Edward, and N. M. ELSayed, "Diode laser versus sclerotherapy: bloodless approaches in the treatment of oral pyogenic granuloma (randomised controlled clinical trial)," Odontology, 111(2), pp. 511-521 (2023). doi:10.1007/s10266-022-00759-9.
[16] N. Silberberg, M. Goldstein, and A. Smidt, "Excessive gingival display-etiology, diagnosis, and treatment modalities," Quintessence Int., 40(10), pp. 809-818 (2009).
[17] E. Işiksal, S. Hazar, and S. Akyalçin, "Smile esthetics: perception and comparison of treated and untreated smiles," Am. J. Orthod. Dentofacial Orthop., 129(1), pp. 8-16 (2006). doi:10.1016/j.ajodo.2005.07.004.
[18] T. N. Aldelaimi, et al., "Gummy smile esthetic correction with 940 nm diode laser," 26(6), pp. 513-515 (2025).
[19] A. A. Khalil, T. N. Aldelaimi, and S. M. Abdulkaream, "Pleomorphic adenoma of palatal minor salivary glands," Rev. Esp. Cir. Oral Maxilofac., 46(3), pp. 145-150 (2024).
[20] F. Alpiste-Illueca, "Dimensions of the dentogingival unit in maxillary anterior teeth: a new exploration technique (parallel profile radiograph)," Int. J. Periodontics Restorative Dent., 24(4), pp. 386-396 (2004).
[21] E. T. Daif, "Correlation of age, sex, and location with recurrence of oral giant pyogenic granuloma after surgical excision," J. Craniofac. Surg., 27(5), pp. 433-435 (2016). doi:10.1097/SCS.0000000000002711.
[22] A. S. Al-Noaman, "Pyogenic granuloma: clinicopathological and treatment scenario," J. Indian Soc. Periodontol., 24(3), pp. 233-236 (2020). doi: 10.4103/jisp.jisp_132_19.
[23] M. A. Khan, S. Nazir, M. U. Haider, M. Hameed, A. Shabbir, and B. Shirazi, "Surgical excision vs minimally invasive (scaling & curettage) treatment for oral pyogenic granuloma," Ann. Punjab Med. Coll., 16(4), pp. 310-313 (2022). doi:10.29054/apmc/2022.1218.

الفعالية السريرية لليزر الدايودي في علاج الورم الحبيبي القيحي الفموي

ايمن عدنان نجم*، تحرير نزال الدليمي

قسم جراحة الفم و الوجه و الفكين، كلية طب الاسنان، جامعة الانبار، الرمادي-محافظة الانبار، العراق.

للباحث البريد الالكتروني:aymanadnan.n.a@gmail.com

الخلاصة: الورم الحبيبي القيحي (Pyogenic Granuloma, PG) هو آفة فموية حميدة شديدة الوعائية، تتظاهر عادة بعدم الارتياح وحدوث نزف متكرر. ويعد الاستئصال الجراحي التقليدي علاجا فعالا، إلا أنه غالبا ما يرتبط بألم ما بعد الجراحة واحتمالية النكس. ويوفر الاستئصال باستخدام ليزر الدايود بديلا علاجيا قليل التداخل، يتميز بالدقة العالية في إزالة النسج وتحقيق إرقاء ممتاز. الأهداف: تقييم فعالية وسلامة الاستئصال باستخدام ليزر الدايود في تدبير الورم الحبيبي القيحي الفموي.

المواد وطرائق العمل: شملت الدراسة ستة عشر مريضا مصابين بورم حبيبي قيحي فموي حديث الظهور (11 ذكور و5 إناث)، تراوحت أعمارهم بين 15 و74 سنة، بمتوسط عمري قدره 39.3 سنة. تم استئصال جميع الآفات تحت التخدير الموضعي باستخدام ليزر دايود بطول موجي 980 نانومتر وباستطاعة 1.5 واط في النمط المستمر. تم الحفاظ على هامش أمان مقداره 0.5 مم، وأسهم النزف الطفيف في الاستغناء عن الخياطة الجراحية. جرى تقييم المرضى في اليومين الأول والثالث بعد الجراحة، ثم بعد أسبوع وثلاثة أسابيع. وتم تسجيل شدة الألم، ومستوى الإرقاء، وسير التئام الجرح، ودرجة رضا المرضى في كل زيارة. كما خضعت النسج المستأصلة للفحص النسيجي المرضي لتأكيد التشخيص .النتائج: أظهر ليزر الدايود قدرة ممتازة على التحكم بالنزف أثناء الجراحة، حيث كان أي نزف طفيف سهل السيطرة عليه. وانخفضت شدة الألم بسرعة، إذ شعر معظم المرضى بالراحة بحلول اليوم الثالث، وأصبحوا خالين تماما من الألم خلال أسبوع واحد. وتقدم التئام الجروح بشكل سريع، مع نتائج جيدة إلى ممتازة بعد أسبوع، وشفاء كامل خلال ثلاثة أسابيع. وأفاد معظم المرضى بدرجة عالية من الرضا في المتابعة النهائية. الاستنتاج: يعد الاستئصال باستخدام ليزر الدايود وسيلة علاجية آمنة وفعالة للورم الحبيبي القيحي الفموي، لما يوفره من إرقاء متفوق، وانخفاض في الانزعاج بعد الجراحة، وتسارع في التئام الجروح، وارتفاع مستوى رضا المرضى. وتدعم هذه النتائج الأداء السريري المتسق لليزر الدايود كخيار علاجي موثوق في الممارسة السريرية الروتينية المعاصرة.

IJL, Vol. 25, Issue1, 2026
http://doi.org/10.31900/ijl.v25i1.562

Research Article

IRAQI JOURNAL OF LASER

Spectroscopic Diagnostics of Laser-Induced Silver Plasma Using LIBS at Different Laser Energies

Dalal Y. Sarhan*, Kadhim A. Aadim

Institute of Laser for Postgraduate Studies, University of Baghdad, Baghdad, Iraq
** Email address of the Corresponding Author: dalal.yaarob2401m@ilps.uobaghdad.edu.iq*

Article history: Received 17 Jan. 2026, Accepted 28 Mar. 2026, Published online 15 Jun. 2026

Abstract: Laser-induced breakdown spectroscopy (LIBS) has been used to investigate the plasma generated from a silver target by the Nd:YAG laser system at a wavelength of 1064 nm. The plasma was produced at different laser pulse energies (500, 600, 700, and 800 mJ) to study the effect of laser energy on plasma parameters. The electron temperature (Te) was determined using the Boltzmann plot method, while the electron density (ne) was calculated using Stark broadening of the spectral lines. Moreover, other plasma parameters such as plasma frequency (f_p), Debye length (λ_D), and Debye number (N_D) have been evaluated. The results showed that the electron density increased from 3.11×10^{17} cm^{-3} to 5.32×10^{17} cm^{-3} with increasing laser energy, while the electron temperature increased from 0.64 eV at 500 mJ to 0.84 eV at 800 mJ. The plasma frequency also increased from 5.01×10^{12} Hz to 6.55×10^{12} Hz, whereas the Debye length decreased from 3.37×10^{-7} cm to 3.06×10^{-7} cm. The Debye number (ND) was greater than unity, confirming that the generated plasma satisfies the basic conditions of a stable ionized plasma. These results indicate that increasing laser energy significantly influences excitation, ionization processes, and overall plasma characteristics.

Keywords: LIBS, Ag plasma, Stark broadening, plasma parameters, Laser-induced plasma.

1. Introduction

Laser-induced breakdown spectroscopy (LIBS) is a versatile spectroscopic technique that analyzes the spectral emission from laser-generated plasma, resulting in the rapid detection of the elements of matter. Recent literature has increased the application of LIBS in many research works [1] as it is very fast and can be used to conduct tests without having to move the sample. The effectiveness of this technique depends on several factors such as the wavelength of the laser, the number of pulses, pulse repetition rate and energy. The principle of operation can be seen as the repair of the sample, followed by irradiation with a laser of a certain energy level. This process takes out a small portion of the sample and produces a hotter plasma [2,3]. Plasma usually consists of ions and electrons. It is the collision of these ions that causes them to achieve a high energy level which is then dropped back to a lower energy level to cause the production of certain radiation. The light emitted is then imaged using a spectrometer to analyze its components and concentration [4]. The particularities of silver nanoparticles have made them essential and very relevant in studies and research as they are applicable to a wide range of fields and applications, including biological

applications and drug delivery [5], optics, and medicine [6]. The use of silver nanoparticles has also been widely felt in day-to-day life, including coating most of the surfaces of household appliances and equipment, because of their antibacterial effect and the capability to prevent the growth of fungi [7]. One of the key techniques that may be used to investigate the impact of lasers on plasma during the process of ablation is LIBS technology, which will help in enhancing the properties of the photoemission [8].
Past research studies have revealed that silver nanoparticles are antibacterial because of their large total surface area and nano capacity, since nanoparticles are more effective in killing bacteria than the larger nanoparticles, thus making them indispensable in biological applications. [9]. Rajaa N. Ketan, Muayyed J. Zoory, and others have demonstrated that pulse-coupled analysis and uncalibrated analysis are among the most important factors upon which LIBS technology depends [10]. As Wisam D. Jalal, Mohanad A. Aswad, and others have shown, LIBS is one of the most important technologies in medicine. They used LIBS and other techniques to study children's teeth using an Nd-YAG laser with a wavelength of 1064 nm and a specific energy to record the emission spectrum. They proved that LIBS is more accurate and comprehensive than other techniques for practical and academic dental applications [11].

The elemental composition and emission lines of silver plasmas produced by laser ablation at various energies (500,600,700,800mJ) help to evaluate the parameters and behavior of the plasmas, including density and temperature of the electrons, which are important aspects of successful analysis. The spectroscopic characterization is aimed at measuring the spectrum emitted to identify silver atoms and ions, to study the excitation mechanism of plasma, and the influence of the laser on the material and its effects on the formation of plasma. The value of this characterization is that it exhibits high analysis speed, enhanced laser properties, and the synthesis of nanoparticles, which are useful in the biological domain.

Even though LIBS has been widely used in plasma diagnostics, little is known systematically on the silver plasma produced at relatively high laser energies. In this study, the plasma properties of silver were studied in the range of laser energy of 500-800 MJ with LIBS. The research aims at measuring the most important plasma parameters, including electron temperature, electron density, plasma frequency, Debye length, and Debye number. The results obtained give a better picture about the impact of the laser energy on the behavior of the plasma and its spectroscopic characteristics.

2. Materials and Methods

Figure 1 presents the schematic diagram of the experimental setup used for LIBS plasma generation. A Q-switched Nd:YAG laser operating at a wavelength of 1064 nm was used to generate plasma. The laser beam was focused perpendicularly onto a high-purity silver target (Ag, 99.99%). The silver sample had an approximate thickness of 1 mm and was carefully cleaned prior to the experiment to remove any surface contamination. The target was mounted on a fixed holder, and the distance between the focusing lens and the sample surface was maintained at approximately 10 cm. Plasma was generated using different laser pulse energies of 500, 600, 700, and 800 mJ, while the number of laser pulses was kept constant at 300 pulses for all measurements.

At the point of interaction between the laser beam and the silver surface, the rapid heating and ablation processes took place, which resulted in the appearance of the high temperature plasma plume consisting of excited atoms, ions, and free electrons. An optical fiber probe has been placed at a proper angle to the plasma to prevent exposure to the laser beam to gather the optical emission of the plasma plume.

The emission obtained was passed to a spectrometer that was linked to a computer to acquire spectral data and analyze it. The emission spectra, which indicated the association between the intensity of emission and wavelength, were demonstrated on the spectrometer, and the achieved spectra were analyzed with the aid of special analysis software. The spectrometer had a wavelength error of about 0.02 nm. According to the spectral resolution and the procedures that were applied during the analysis of the Boltzmann plot and Stark broadening, the error of the determined plasma parameters was determined to be approximately 5 percent.

The laser pulse energies (500-800 mJ) selected were to make sure that there would be enough plasma formation and high emission intensity that could be analyzed using spectroscopy. At lower energies, the plasma emission can be weak and unstable, and consequently, the measurement of plasma parameters (e.g., electron temperature, electron density) is less precise. Thus, comparatively large laser energies have been utilized in the given study to increase the ablation efficiency, the population of additional exciting species in the plasma plume and achieve emission lines with sufficient strength to permit a more stringent spectroscopic diagnostic.

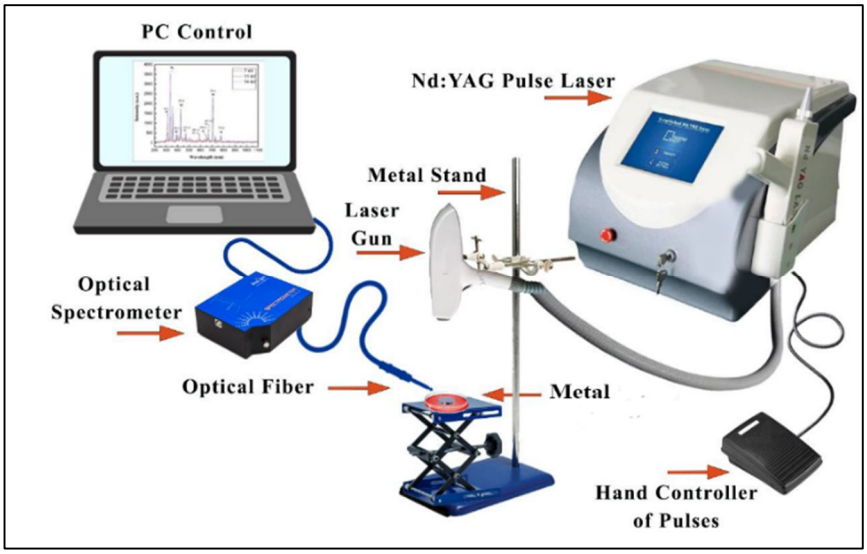

Fig. 1: Schematic diagram of the LIBS experimental setup using an Nd:YAG laser (1064 nm) [12].

2.1. Plasma Parameters Calculation

The plasma parameters have been calculated from the emission spectra using several well-known spectroscopic relations. The electron temperature (Te) was determined using the Boltzmann plot method according to the following relation [13]:

$$\ln\left[\frac{\lambda_{ji} I_{ji}}{hcA_{ji}g_j}\right] = \frac{1}{k_B T}(E_j) + \ln\left[\frac{N}{U(T)}\right] \qquad (1)$$

where Iji is the emission line intensity, lambda_ji is the wavelength of the spectral line, Aji is the transition probability, gj is the statistical weight of the upper level, h is Planck's constant, c is the speed of light, Ej is the upper energy level, kB is the Boltzmann constant, Te is the electron temperature, N is the total number density of emitting species, and U(T) is the partition function.
The electron density (ne) was calculated using the Stark broadening method according to [13]:

$$n_e = \left(\frac{\Delta\lambda_{FWHM}}{2w}\right) N_r \qquad (2)$$

where $\Delta\lambda_{FWHM}$is the full width at half maximum of the spectral line, w is the Stark broadening parameter, and Nr is the reference electron density.

The plasma frequency was calculated using [13]:

$$f_p = \sqrt{\frac{e^2 n_e}{\varepsilon_0 m_e}} \quad (4)$$

Where e is the electron charge, ε0 is the permittivity of free space, and me is the electron mass.
The Debye length was calculated from [14]:

$$N_D = \frac{4}{3}\pi n_e \lambda_D^3 \quad (5)$$

3. Result and discussion

Figure (2) represents the emission spectra of silver plasma generated using LIBS technology at different energies ranging from (500 to 800mJ). The figure represents the relationship between emission intensity and wavelength, which ranges from (200 to 800 nm). The visible lines represent sharp peaks belonging to silver atoms and ions resulting from electronic transitions between different energy levels. It was found that the emission intensity is affected by changing laser energy, as increasing the laser energy leads to an increase in emission intensity (the emission intensity at (800mJ) was observed to be higher than at (500mJ). This is because the increased energy leads to increased evaporation of the material from the sample surface and the generation of a hotter plasma, in addition to increased electronic transitions between silver atoms and ions. It was also found that the positions of the spectral peaks did not change despite the change in laser energy; only the intensity of the radiation changed.

This promotes the production of a more stable plasma in terms of elemental composition, in addition to the fact that silver is a pure element without any additional impurities. These results are coherent with the changes in Figure 3, which shows the relationship between the electron density ne measured in ($\times 10^{17}$ cm^{-3}) and the electron temperature Te measured in (eV). It was observed that the density and temperature of electrons are directly proportional to the change in laser energy; there is a direct relationship between the emission intensity and the temperature and density of electrons, and this proves that the properties of the plasma depend on the laser energy. This is one of the features that indicates an improvement in plasma properties, in addition to its suitability for spectral diagnosis**.**

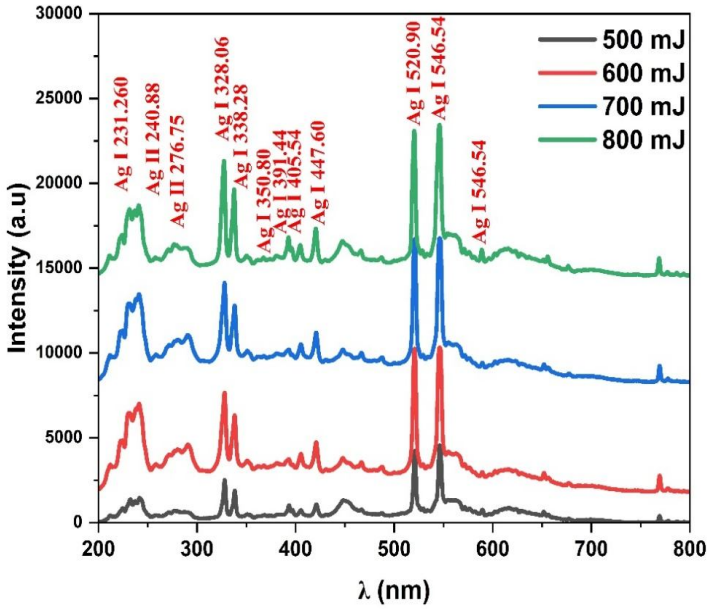

Fig. 2 Emission spectra of Ag plasma at different laser energy.

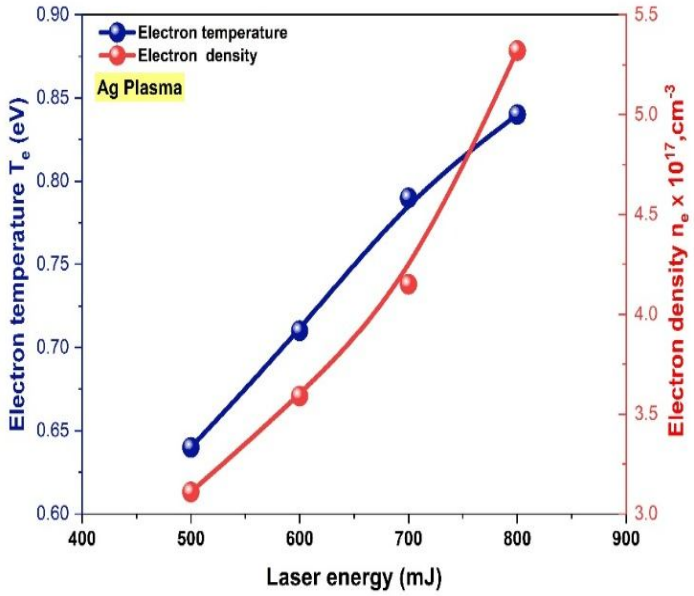

Fig. 3 The relationship between electron density and temperature at different laser energies.

Figure 4 illustrates the Boltzmann chart of silver plasma with a varying laser energy (500, 600, 700, and 800 mJ). The electron temperature was determined using these plots using the intensities of the Ag spectral lines created by the emission. The logarithmic function ln (I ln /Ag) is plotted against the vertical axis, and the maximum energy level of the transition is plotted against the horizontal axis. There is a line and the slope of the line (slope = -1/kTe) is taken to determine the temperature of the electrons.

This is demonstrated in the results that the electron temperature rises with the increase of laser energy, with maximum and minimum values at 800 mJ and 500 mJ. The increased value of the R 2 (>0.90) is a good fit linear and it shows that the plasma meets the LTE condition. Such findings indicate that the higher the laser energy, the higher the plasma excitation and ionization increases the emission intensity,

as indicated by the spectra in Figure 2.

Figure 5 shows the Stark Broadening of the silver (Ag I) spectral line, centered approximately at a wavelength of 547 nm, at multiple energies ranging from (500 to 800mJ). It shows that the penetrating intensity is proportional to laser energy (increasing the laser energy leads to a rise in the number of free electrons, a rise in the amount of ionized material, a rise in the spectral peak intensity, and an increase in the full width at half maximum (FWHM).

This peak has been used to calculate the electron charge because the broadening of the line indicates an increase in electron density. It was observed that at 500mJ, the FWHM is narrow, indicating weak plasma ionization, while at 800mJ, the FWHM, or Stark broadening, is wide, demonstrating strong plasma ionization. This proves that laser energy has a clear effect on the Stark effect due to collisions between ions and electrons of the silver element, resulting in a high-density plasma [14].

To verify the validity of the local thermodynamic equilibrium (LTE) condition in the plasma, the McWhirter criterion was applied. According to the McWhirter criterion, the electron density must satisfy the following conditions:

$$n_e \geq 1.6 \times 10^{12} T_e^{\frac{1}{2}} (\Delta E)^3 \mathrm{cm}^{-3}$$

where T is the temperature of the electrons (in eV), and 0 is the difference in the energy of the relevant energy levels (in eV).

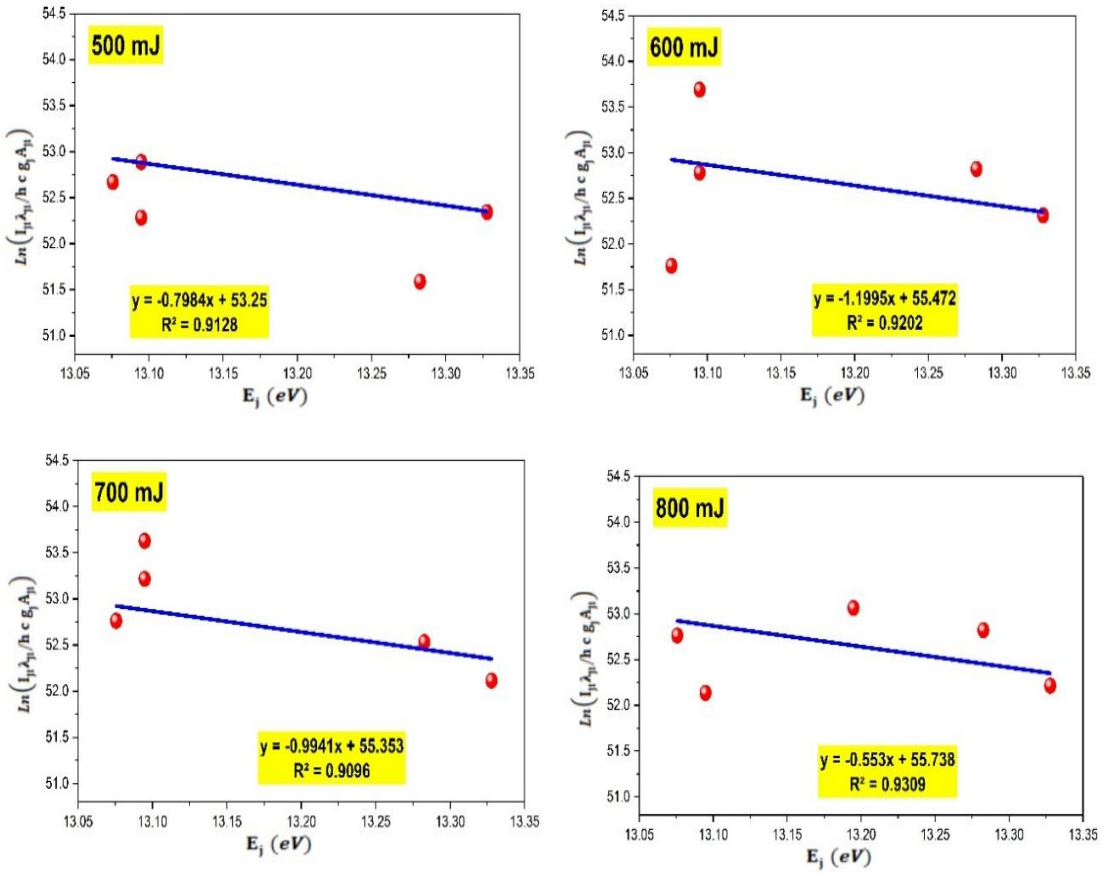

Fig. 4 Boltzmann plots of Ag plasma at different laser energies (500–800 mJ) used to determine the electron temperature (Te).

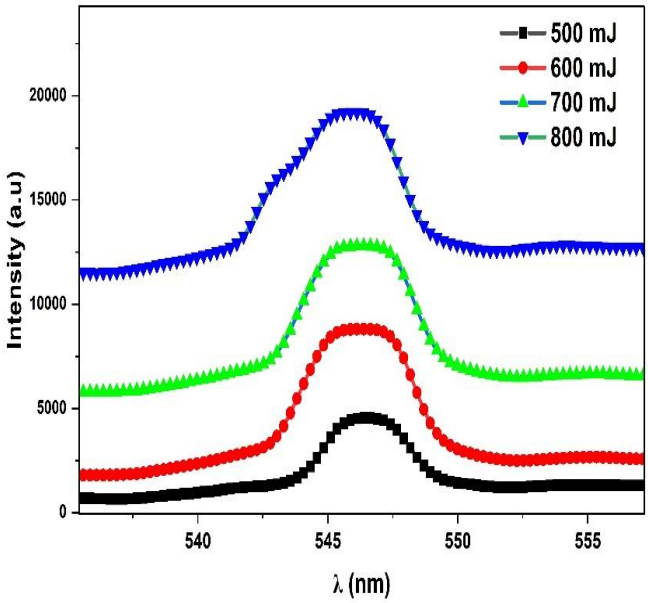

Fig. 5 Stark Broadening of the Ag spectrum

This study determined the minimum electron density necessary to satisfy the LTE condition using the obtained parameters of the plasma and found that the value was quite lower than the experimental values of electron densities. The McWhirter criterion is easily fulfilled since the values of the measured electron density are of the order of 10^{17} cm $^{-3}$. Thus, it may be concluded that the plasma produced in this experiment may be in the local thermodynamic equilibrium.

Table 1 summarizes the main plasma parameters of silver plasma, including electron temperature (Te), electron density (ne), plasma frequency (fp), Debye length (λD), and Debye number (Nd), and their dependence on laser energy. It can be observed that the electron temperature increases from 0.64 eV at 500 mJ to 0.84 eV at 800 mJ. Similarly, the electron density increases from 3.11×10^{17} cm^{-3} to 5.32×10^{17} cm^{-3} with increasing laser energy. This behavior is attributed to the higher laser energy, which enhances the ablation rate of the target material and increases the number of excited and ionized particles in the plasma plume. The plasma frequency (fp) also increases with increasing electron density, since the plasma frequency is proportional to the square root of electron density ($fp \propto \sqrt{ne}$). As the number of free electrons increases, the collective oscillation frequency of electrons in plasma increases accordingly.

On the other hand, the Debye length (λD) decreases gradually from 3.37×10^{-7} cm at 500 mJ to 3.06×10^{-7} cm at 800 mJ. The Debye length represents the characteristic shielding distance in plasma and depends on both electron temperature and electron density according to the relation $\lambda D \propto \sqrt{(Te / ne)}$. Therefore, the increase in electron density at higher laser energies leads to a reduction in the Debye length, indicating stronger electrostatic shielding and a more confined plasma environment. Moreover, with rising laser energy, the increase in Debye number (Nd) is caused by a rise in the electron density and a drop in Debye length. The values of Nd obtained are bigger than unity, which means the produced silver plasma meets the minimum plasma requirements and the behavior of a stable and well-ionized plasma.

Table 1. Laser-induced plasma parameters of Ag Plasma at different laser energy

E (mJ)	Te (eV)	ne (cm^{-3})*10^{17}	fp (Hz) *10^{12}	λD (cm) *10^{-7}	Nd*10^{3}
500	0.64	3.11	5.01	3.37	1.48
600	0.71	3.59	5.38	3.32	1.65
700	0.79	4.15	5.74	3.29	1.82
800	0.84	5.32	6.55	3.06	1.93

The uncertainty in the calculated plasma parameters mainly arises from the spectral measurement accuracy and the fitting procedures used in the Boltzmann plot and Stark broadening methods. The wavelength resolution of the spectrometer was approximately ±0.02 nm, which introduces a small uncertainty in determining the spectral line positions and widths. Consequently, the estimated uncertainty in the calculated electron temperature and electron density is about ±5%.

The practical applications of silver in (medical and biological) applications can also be related to the obtained plasma parameters. The antimicrobial activity of silver made it be popular in the application of antibacterial coating on medical devices, wounds, and antibacterial dressings. It is important to understand the plasma characteristics like the electron temperature and the electron density since these are the parameters that directly affect the ablation efficiency, ionization, and the silver species that form when the laser interacts with the material. Increased electron temperature and density show greater excitation of the plasma and better ablation of material which will be useful in increasing the control of silver particle formation and surface modification process. Thus, spectroscopic diagnostics introduced in the present paper will help to understand better the interaction of laser with silver that would facilitate optimization of laser-based procedures in the preparation of antimicrobial coatings, biomedical sensors, and silver-based nanomaterials. The parameters of plasma retrieved in the current research are affirmative of other LIBS

studies carried out in the past. Subsequent rises in electron temperature and electron density under rising laser energy are consistent with the findings of studies done on the spectroscopic diagnostics of CuZn plasma produced by a Nd:YAG laser, in which both parameters increased substantially with laser pulse energy owing to greater laser–matter interaction and excitation interactions (Shaltout et al., 2010) [17]. Besides, the recent LIBS experiments on metallic targets proved that the more laser energy is used, the more plasma excitation is developed and, as a result, the higher the temperature of electrons and their density and the intensity of spectral emissions (Azam et al., 2025) [18]. Moreover, recent spectroscopic studies of laser-induced plasma in metallic materials observed electron densities of the order of 1017 cm - 1 and demonstrated that the parameters of the plasma strongly depend on the laser energy and the conditions of the experiment (Abed et al., 2025) [19]. Thus, the findings made in the current research are well consistent with the already existing and published experimental research on laser-induced plasma diagnostics.

4. Conclusion

During this study, a sample of silver plasma has been prepared by irradiating the sample with multiple energies ranging from 500 to 800mJ and 300 pulses. The expansion of the silver emission line was observed due to the strong integration between electrons and ions in plasma, in addition to clear changes in plasma parameters. The Boltzmann diagram method was used to determine the electron heat (Te), and it was observed that Te is directly proportional to the laser energy, as the value of Te gradually increased with the increase in laser energy. Similarly, for the electron density (n_e), its value was shown to rise with a rise in laser energy, and it was characterized using the Stark Broadening method. The results showed that all plasma parameters increase with the increase in laser energy, and this is evidence of an increase in plasma density and the ablation rate with higher energies, in addition to an increase in plasma temperature and in coherence, except for the Debye length(λD), whose value decreases with the increase in energy, because the increase in density of electron leads to the proximity of the particles, and thus the expansion in the internal electric field decreases. The results obtained confirm that laser energy is a key factor in controlling the properties of the silver plasma, as increasing the energy leads to improved excitation and ionization within the plasma. In the Boltzmann diagram that used to calculate electron heat (T_e) from the slope of the straight lines, all diagrams showed that the value of R^2 is greater than 0.90, which confirms the fulfillment of the thermal equilibrium condition (LET) and the possibility of using the Boltzmann method to determine the electron heat.

Author Declaration

The authors declare that this work is original, has not been published before, and is not under consideration elsewhere. All authors approved the final manuscript.

Ethics Approval and Consent for Authors

This study does not involve humans or animals; therefore, ethical approval is not required.

Authors Contribution

Dalal Y. Sarhan performed the experiments and wrote the manuscript. Kadhim A. Aadim supervised the work and revised the manuscript. All authors approved the final version.

References

[1] L.J. Radziemski, D.A. Cremers, Laser-Induced Plasmas and Applications, Marcel Dekker, Inc, New York, 1989.
[2] P. Thapa, N. Bachhar, Sh. Sarma, Substrate-dependent thermal sensing using silver nanoparticles synthesized via laser ablation in solution., Scientific Reports, **15**, 23614 (2025) https://doi.org/10.1038/s41598-025-02431-y

[3] Shaker, A.H., Aadim, K.A., and Nida, M.H. Spectroscopic analysis of zinc plasma produced by alternating and direct current jet. J Opt 53, 1273–1281 (2024). https://doi.org/10.1007/s12596-023-01256-0
[4] S. F. Khaleel and K. A. Aadim, "Investigation study of the plasma parameters for bronze produced by Nd:YAG laser at wavelength 1064 nm: effect of laser energies", Journal of Optics, **54**, 256-266 (2025). https://doi.org/10.1007/s12596-025-02698-4
[5] S. Aisida, K. Ugwue, A. Nwanya, A. Bashir, N. Nwankwo, I. Ahmed, F. Ezema, Biosynthesis of silver oxide nano- particles using leave extract of Telfairia Occidentalis and its antibacterial activity, Mater. Today Proc. **36** (2021) 208-213, https://doi.org/10.1016/j.matpr.2020.03.005.
[6] Q. Mohameed, F. Hattab, M. Fakhry, Effect of substrate temperature on structural characteristics of nano silver oxide structural characteristi prepared by pulsed-laser deposition, IJAP 11 (2015) 33-36. https://www.jasj.net/iasi/article/103341.
[7] M. Alhamid, B. Hadi, A. Khumaeni, Synthesis of silver nanoparticles using laser ablation method utilizing Nd:YAG laser, AIP Conf. Proc. **2202** ,020013(2019), https://doi.org/ douru 10.1063/1.5141626M.
[8] M.M. Hameed, A.-M.E. Al-Samarai, K.A. Aadim, Synthesis and characterization of gallium oxide nanoparticles using pulsed laser deposition.Iraqi Journal of Science, **61**(10), 2582–2589(2020) https://doi.org/10.24996/ijs.2020.61.10.14
[9] Turki, Z. T., Fahem, M. Q., Mankhi, Z. A., & Jawad, M. H. (2025). Magnetic field effect on cadmium oxide plasma properties detected by laser spectroscopy. Russian Physics Journal, 68(5), 804-812.
[10] A. Al-Sharqi, K. Apun, M. Vincent, D. Kanakaraju, L. Bilung, Enhancement of the antibacterial efficiency of silver nano- particles against gram-positive and gram-negative bacteria using blue laser light, Int. J. Photoenergy (2019), https:// doi.org/10.1155/2019/2528490
[11] A A-K. Hussain, A. A. Al-Razzaq,Plasma characteristics of Ag:Al alloy produced by fundamental and second harmonic frequencies of Nd:YAG laser. Iraqi J. Physics.**14**(31), 205-214(2016) https://doi.org/10.30723/ijp.v14i31.188
[12] Ketan, R. N., Zoory, M. J., & Mohamad, H. J. (2025). Laser-Induced Breakdown Spectroscopy: Principles and Advanced Applications. Journal of Applied Sciences and Nanotechnology, 5(1), 25-32.
[13] Jawad, M.H., Abdulameer, M.R. Spectroscopic investigation of plasma from Al–Ni alloy using OES technique: influence of voltage on plasma parameters. Indian J Phys 99, 4845–4850 (2025). https://doi.org/10.1007/s12648-025-03738-2
[14] M.A. Essa, K. A. Aadim., "Spectroscopic study the plasma parameters for SnO2 doped ZnO prepared by pulse Nd:YAG laser deposition", Iraqi J. Phys., **17**, 125–135 (2019). https:// doi.org/10.20723/ijp.17.42.125-135
[15] M. H. Jawad and M. R. Abdulameer, "The effect of background argon gas pressure on parameters of plasma produced by Dc- glow discharge," Iraqi J. Sci., vol. 64, no. 3, pp. 1210–1218, 2023, doi: 10.24996/ijs.2023.64.3.17.
[16] M.H. Jawad, M.R. Abdulameer, Spectral analysis of brass plasma generated by a Nd:YAQ laser at λ = 1064 nm. Russ Phys J., **68**, 903–911 (2025). https://doi.org/10.1007/s11182-025-03509-w
[17] Shaltout, A. A., Mostafa, N. Y., Abdel-Aal, M. S., & Shaban, H. A. (2010). Electron number density and temperature measurements in laser produced brass plasma. The European Physical Journal Applied Physics, 50(1), 11003.
[18] Azam, H., Shahbaz, R. M., & Hussain, A. (2025). Role of laser pulse energy as an effective strategy to improve the signal intensity in laser-induced breakdown spectroscopy. Results in Optics, 21, 100845.
[19] Abed, H. A., Mazhir, S. N., & Alrashid, S. N. (2025). Spectroscopic Investigation of Plasma Parameters in an Iron Target: A comparative study of different laser energies. Baghdad Science Journal, 22(10), 3421-3429.

التشخيص الطيفي لبلازما الفضة المحفزة بالليزر باستخدام تقنية التحليل الطيفي بالليزر عند طاقات ليزر مختلفة

دلال يعرب سرحان*, كاظم عبد الواحد عادم

معهد الليزر للدراسات العليا، جامعة بغداد، بغداد، العراق

البريد الالكتروني للباحث: dalal.yaarob2401m@ilps.uobaghdad.edu.iq

الخلاصة: في هذا العمل استخدمت تقنية التحليل الطيفي بالانهيار المستحث بالليزر (LIBS) لدراسة البلازما المتولدة من هدف فضة باستخدام ليزر Nd:YAG بطول موجي 1064 نانومتر. تم توليد البلازما عند طاقات ليزر مختلفة لدراسة تأثير طاقة الليزر في معاملات البلازما. حسبت درجة حرارة الإلكترون باستخدام طريقة مخطط بولتزمان، بينما حسبت كثافة الإلكترونات باستخدام اتساع ستارك لخطوط الطيف. كما تم تقييم بعض معاملات البلازما الأخرى مثل تردد البلازما وطول ديباي وعدد ديباي. أظهرت النتائج أن زيادة طاقة الليزر تؤدي إلى زيادة درجة حرارة الإلكترون وكثافة الإلكترونات وشدة الانبعاث الطيفي، في حين ينخفض طول ديباي مع زيادة كثافة البلازما. وتشير قيم عدد ديباي إلى أن البلازما المتولدة تحقق شروط البلازما المستقرة. تؤكد هذه النتائج أن طاقة الليزر تعد عاملا مهما في تحديد خصائص البلازما المتولدة من الفضة باستخدام تقنية LIBS.

IJL, Vol. 25, Issue 1, 2026 **Research Article**
http://doi.org/10.31900/ijl.v25i1.569

Tapered and Coated Optical Fiber with Fe_3O_4 Nanoparticles and Magnetic Fluid for Magnetic Field Detection

Fatima Adel Hamed*, Soudad S. Ahmed

Department of Physics, College of Science, University of Baghdad, Baghdad, Iraq
** Email address of the Corresponding author: fatma.adel1704a@sc.uobaghdad.edu.iq*

Article history: Received 27 Feb. 2026, Accepted 12 Apr. 2026, Published online 15 Jun. 2026.

Abstract: In this work, an optical fiber sensor was developed for magnetic field detection. Single-mode and multi-mode fibers were used based on two main processes: chemical etching using hydrofluoric acid (HF) and coating with Fe_3O_4 nanoparticles. The nanoparticle layer was deposited using pulsed laser deposition (PLD) with an Nd:YAG laser operating at a wavelength of 1064 nm and 70 pulses, achieving a thickness of 49.4 nm in the sensing region. This work demonstrates the use of Fe_3O_4 nanoparticles in the coating process through two different techniques within the optical fiber system. In the first technique, the nanoparticles were deposited as a solid coating via pulsed laser deposition (PLD), achieving a thickness in the nanoscale range of 40–60 nm, which provides an effective surface for interaction. In the second technique, Fe_3O_4 nanoparticles were used in the preparation of a magnetic fluid that acts as a liquid coating, forming a stable and magnetically responsive medium. This dual use of Fe_3O_4 in both solid and liquid coatings provides more effective interaction than the use of a single coating technique. The magnetic fluid was prepared by dispersing 5 g of Fe_3O_4 powder in 13 g of paraffin oil. The experimental results showed that increasing the etching time during the chemical etching process using hydrofluoric acid (HF) led to a reduction in the optical fiber diameter, accompanied by a decrease in the transmitted optical power. These results are consistent with previous studies, which have shown that the tapering process using hydrofluoric acid (HF) transforms a conventional optical fiber into a sensitive element capable of responding to external variations. Therefore, this approach provides a suitable way to improve fiber sensitivity and enables its use in magnetic field sensing applications.

Keywords: Optical fiber sensor, tapered optical fiber, Oil-based magnetic fluid, Fe_3O_4 nanoparticles, Pulsed laser deposition (PLD).

1. Introduction

Optical fiber technology is widely used for data transmission and in communications technology [1, 2]. Optical fiber sensing systems have seen rapid development thanks to their superior sensing performance, and their applications have expanded significantly in recent years due to several advantages, including low cost, small size, light weight, high sensitivity and resistance to electromagnetic interference (EMI) [3, 4, 5]. In optical communication systems, external interference is minimized to ensure reliable signal transmission and reception [2]. In contrast, optical fiber sensing systems are specifically designed to

enhance their sensitivity to external disturbances, allowing changes in light radiation to serve as measurable indicators of environmental changes [3, 4]. The light signal propagating through the fiber is typically modulated before transmission [2]. In sensing applications, however, the optical fiber itself acts as the modulator [3, 4]. Furthermore, as a transducer, it converts physical parameters such as temperature, stress, strain, rotation, electric current, and magnetic field into corresponding changes in optical properties, including intensity, phase, wavelength, and polarization [3, 4, 5]. Despite their advantages, conventional fiber optic sensors often suffer from limited sensitivity, restricting their performance in sensing applications [6, 7]. Recent studies have not adequately explored the integration of chemically etched fiber optics using hydrofluoric acid (HF) [8, 9], pulsed laser deposition (PLD) of Fe_3O_4 thin films [10, 11, 12], and an oil-based stable magnetic fluid within a single fiber optic sensing architecture [13, 14]. Therefore, this paper presents an improvement in the sensitivity of a conventional fiber optic sensor. The sensor is used in magnetic field detection applications, as well as in medical and biological applications (biosensing) and sensing in hazardous environments (environmental applications) [15, 16].

2. Materials and Methods

The experimental process involved fabricating tapered optical fibers using controlled chemical etching. The tapering process was carried out in two main stages. In the first stage, the optical fiber was mechanically clamped and integrated into an optical meter. One end of the fiber was connected to a laser light source operating at a wavelength of 1550 nm, while the other end was connected to a photometer to enable continuous monitoring of the output light energy during the etching process. In the second stage, tapering was achieved by localized etching of the sensing area of the fiber using a 40% hydrofluoric acid (HF) solution prepared at a 1:5 mixing ratio (HF:H_2O). The acid was applied using a plastic needle to ensure precise and localized control of fiber diameter reduction. After the etching process was complete, the acid was removed, and the fiber was immediately immersed in distilled water for 5 min, with the water being changed twice to ensure complete termination of the chemical reaction. Laboratory safety precautions were strictly observed during the tapering process using hydrofluoric acid (HF). The chemical etching process was carried out inside a fume hood to provide a safe working environment. Protective gloves were worn throughout the experiment to avoid direct contact with the acid. In addition, glass containers were avoided because HF reacts with glass; therefore, suitable plastic containers were used. The experimental setup of the optical fiber tapering process is shown in Figure 1.

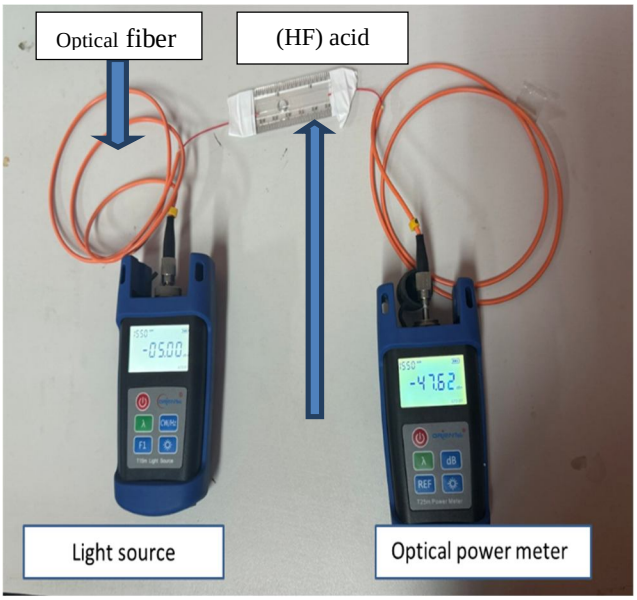

Fig. 1: The experimental setup of the optical fiber tapering process.

2.1. Functional Fiber Coating with Fe_3O_4

Functional coating included the following steps: preparation of the target material (Fe_3O_4) and pulsed laser deposition (PLD).

2.2. Preparation of Fe_3O_4 Target

Fe_3O_4 powder (2g) was used to prepare the deposition target in the form of a pellet. The powder was compressed using a 20-ton hydraulic press under a pressure of 20 bar for 10 min to obtain a dense and mechanically stable target suitable for laser ablation. The use of dense pellet targets is a standard requirement in pulsed laser deposition (PLD) to ensure stable ablation and reproducible thin-film growth. The prepared Fe_3O_4 pellet used as the deposition target is shown in Figure 2.

Fig. 2: The (Fe_3O_4) pellet.

2.3. Pulsed Laser Deposition (PLD) Process

The deposition process was carried out inside the vacuum chamber of a pulsed laser deposition (PLD) system under controlled vacuum conditions, maintaining a chamber pressure of 0.8 Torr. Both the optical fiber substrate and the Fe_3O_4 target were fixed inside the chamber, with the target mounted on a rotating bracket to ensure uniform ejection during deposition. An Nd:YAG laser was used to eject the Fe_3O_4 target, focusing the beam directly onto the target surface. A fixed number of laser pulses (70 pulses) were applied to each deposition sample. The deposition parameters included a wavelength of 1064 nm, a pulse time of 11.7 s, a pulse energy of 500 mJ, and a frequency of 6 Hz. The literature has extensively reported the use of Nd:YAG lasers in the deposition of thin films of oxides, including Fe_3O_4, as providing controlled and reproducible growth under suitable discharge conditions. Safety precautions were also observed during the PLD process. The deposition was carried out within the designated deposition system while ensuring the safe operation of the laser. Appropriate protective eyewear was worn to avoid direct exposure to the laser beam or its reflections. The PLD setup used for the deposition process is shown in Figure 3.

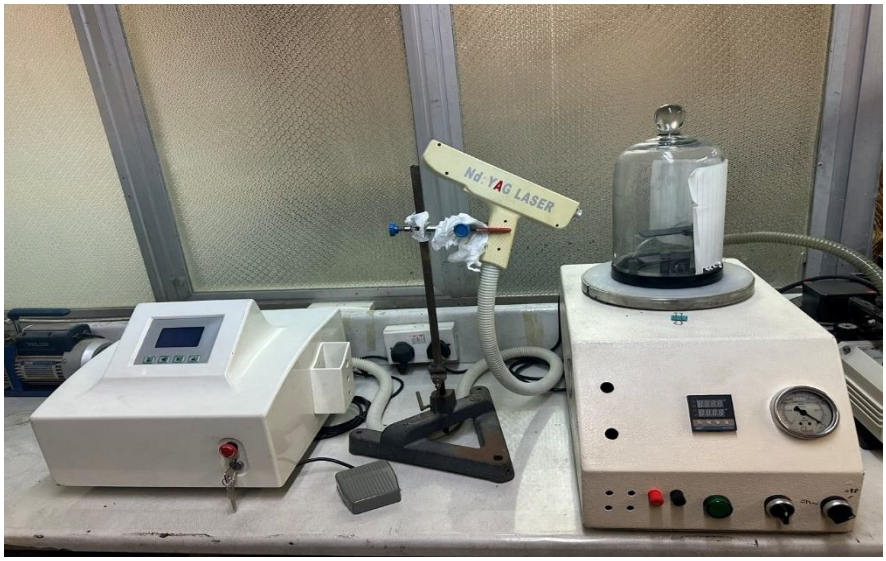

Fig. 3: (A) The PLD setup

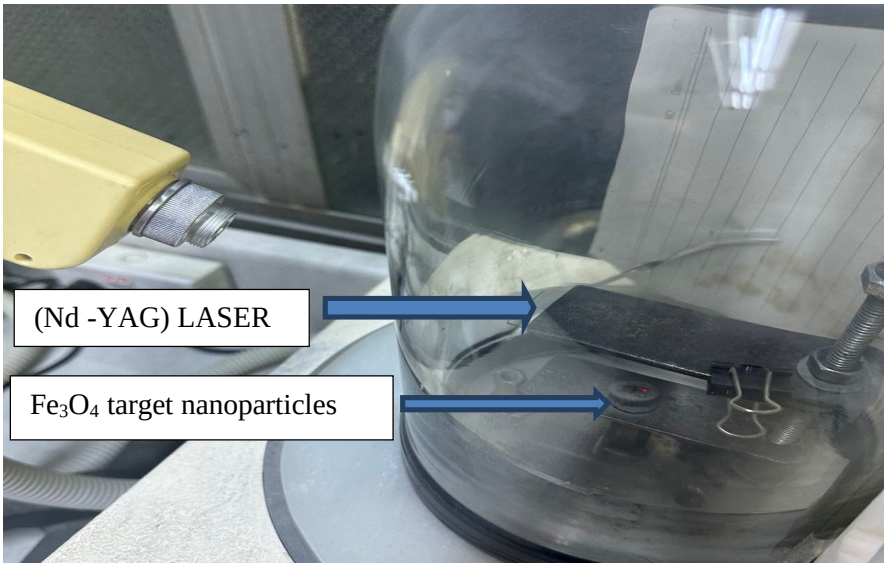

Fig.3: (B) The quartz chamber

2.4. Preparation of Oil-Based Magnetic Fluid

An oil-based magnetic fluid was prepared by dispersing 5 g of magnetite powder (Fe_3O_4) in 13 g of paraffin oil (5:13 ≈ 1:2.6 ratio), using oleic acid (OA) as a surfactant to improve particle stability. Ethanol 70% was used as a temporary dispersing solvent to enhance nanoparticle distribution and ensure homogeneity of the mixture. The mixture was stirred manually to ensure uniform dispersion of the Fe_3O_4 particles and then left for 15–20 min to allow the ethanol to evaporate completely. After the ethanol had evaporated, paraffin oil was gradually added while continuing to stir manually until a homogeneous magnetic fluid was obtained. The prepared magnetic fluid was then applied to the modified (tapered) part of the optical fiber using the drop-casting technique. A carefully measured microscopic droplet was placed on the sensitive area to ensure uniform coverage of the conical surface. The coated fibers were

then kept at room temperature to allow the magnetic liquid layer to stabilize. Figure 4 shows the prepared oil-based magnetic fluid.

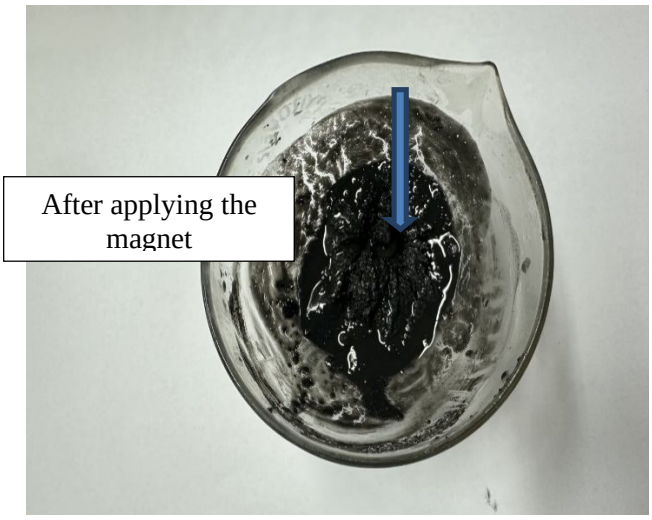

Fig. 4: Oil-Based magnetic fluid

3. Results and Discussion

3.1 Tapered Optical Fiber Diameter Measurement

The reported diameter values in Fig. 5 and Fig. 6 represent the average measurements obtained at multiple positions along the etched region (before and after tapering) using an optical microscope with a magnification of 50×. These measurements correspond to an etching duration of 60 min, which was selected based on a time-dependent etching process conducted at 30, 40, and 60 min. The reduction in optical fiber diameter is attributed to the chemical reaction between hydrofluoric acid (HF) and silica (SiO_2), which is the primary constituent of the optical fiber. The etching process predominantly affects the cladding layer, where HF progressively removes portions of the cladding. Consequently, this partial removal leads to a continuous decrease in fiber diameter with increasing etching time.

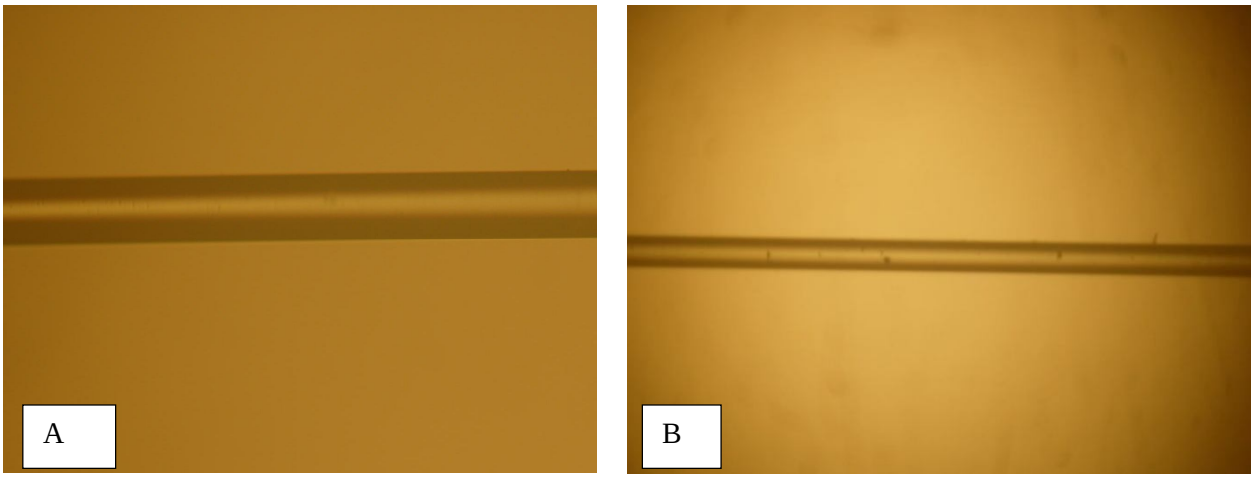

(A) **Fig. 5:** The diameter of multi-mode fiber before and after tapering. (A) Before tapering)121.4 μm) (B) After tapering (65.1 μm) at 60 min.

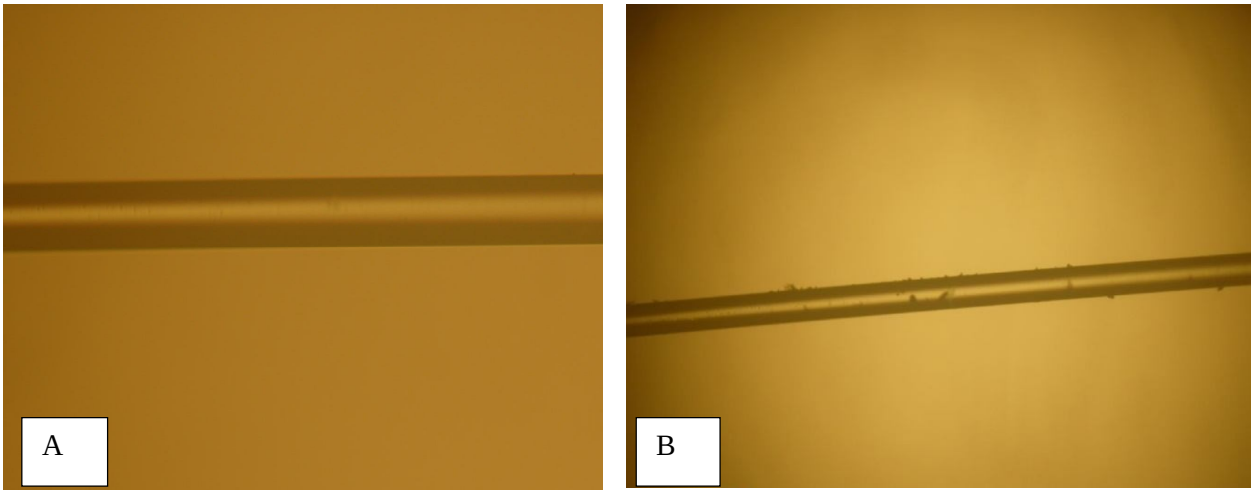

Fig. 6: The diameter of single-mode before and after tapering (A) Before tapering (121.4 µm) (B) After tapering (48.41 µm) at 60 min

3.2. The Results of Tapered Optical Fiber Output Power Measurement

Fig. 7 shows the variation of the output power of the multimode optical fiber with increasing etching time. Multimode fiber supports multiple propagation modes that allow light to travel through different paths within the core. During the tapering process, the reduction in fiber diameter weakens the confinement of these modes, causing a portion of the optical power to extend into the surrounding medium in the form of an evanescent field. Although some modes continue to propagate, mode redistribution occurs within the tapered region, leading to increased propagation losses. As a result, the transmitted power gradually decreases with increasing etching time. This gradual reduction is attributed to the distribution of optical power among multiple modes, which reduces the overall sensitivity of multimode fiber to diameter changes compared to single-mode fiber.

This behavior is attributed to the reduction in fiber diameter, which weakens the confinement of light within the core and enhances the evanescent field, leading to increased optical losses. The obtained results were compared with previously published studies. In her study entitled “Performance Improvement of the Endoscope by Coating with Antimicrobial Agent,” Huda Sahi Raham (2023) reported similar findings, where tapered optical fibers were fabricated using chemical etching with hydrofluoric acid (HF). The study demonstrated that the output power decreases with increasing etching time due to the reduction in fiber diameter and the associated increase in optical losses. This behavior is in good agreement with the present results. Due to the presence of only one propagation mode, the single-mode fiber is highly sensitive to structural changes, resulting in a rapid decrease in output power.

This calibration enabled accurate control of the film thickness by adjusting the number of laser pulses. Accordingly, 70 pulses resulted in a film thickness of approximately 49.4 nm, with a corresponding deposition time of about 11.7 s at a repetition rate of 6 Hz. The observed linear dependence between film thickness and pulse number is consistent with standard pulsed laser deposition behavior reported for oxide thin films under fixed deposition conditions, where the growth rate remains nearly constant and thickness control is achieved through pulse counting. Fig. 8 shows the variation of output power of the single-mode optical fiber with increasing etching time. It can be observed that the transmitted power decreases significantly as the etching time increases. Figure 9 shows that the deposition rate was calibrated using a film thickness of 97.4 nm obtained at 138 laser pulses, yielding an average deposition rate of approximately 0.706 nm/pulse based on the relation $r = t/N$.

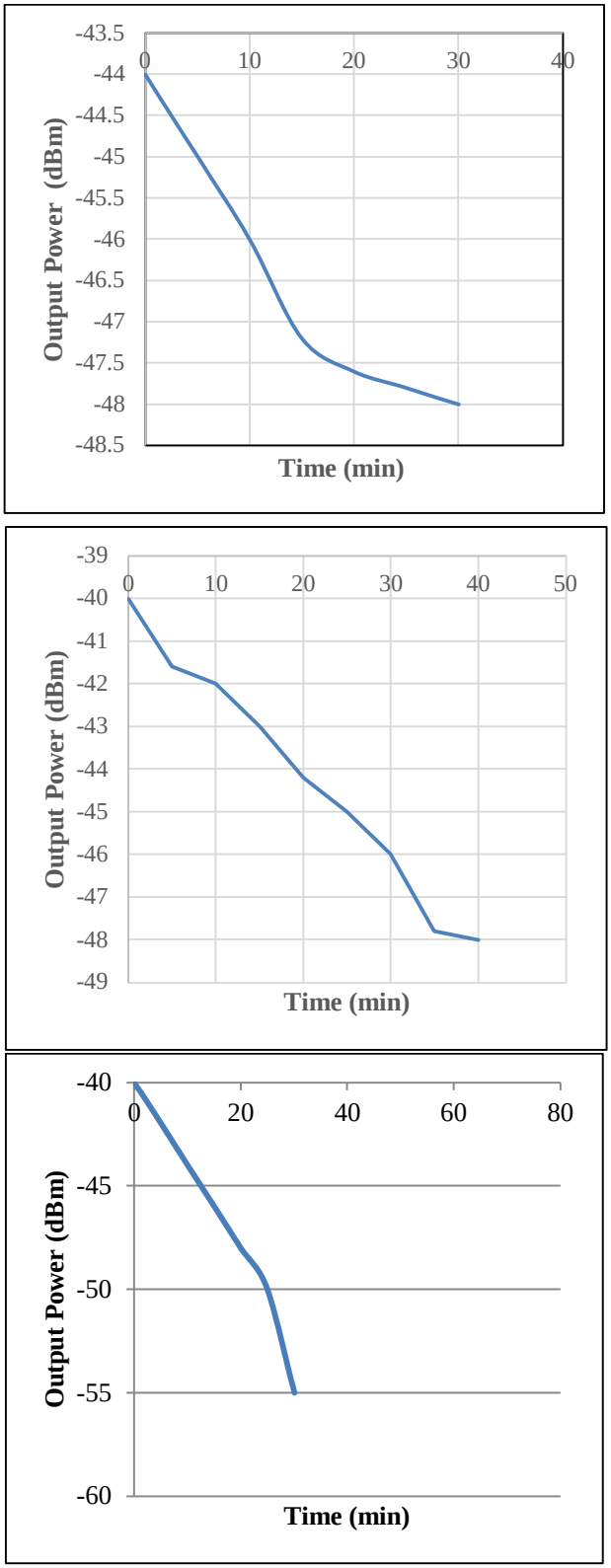

Fig. 7: (A) Output power for the multi-mode fiber at (30 min), (B) Output power for the multi-mode fiber at (40 min), (c) Output power for the multi-mode fiber at (60 min).

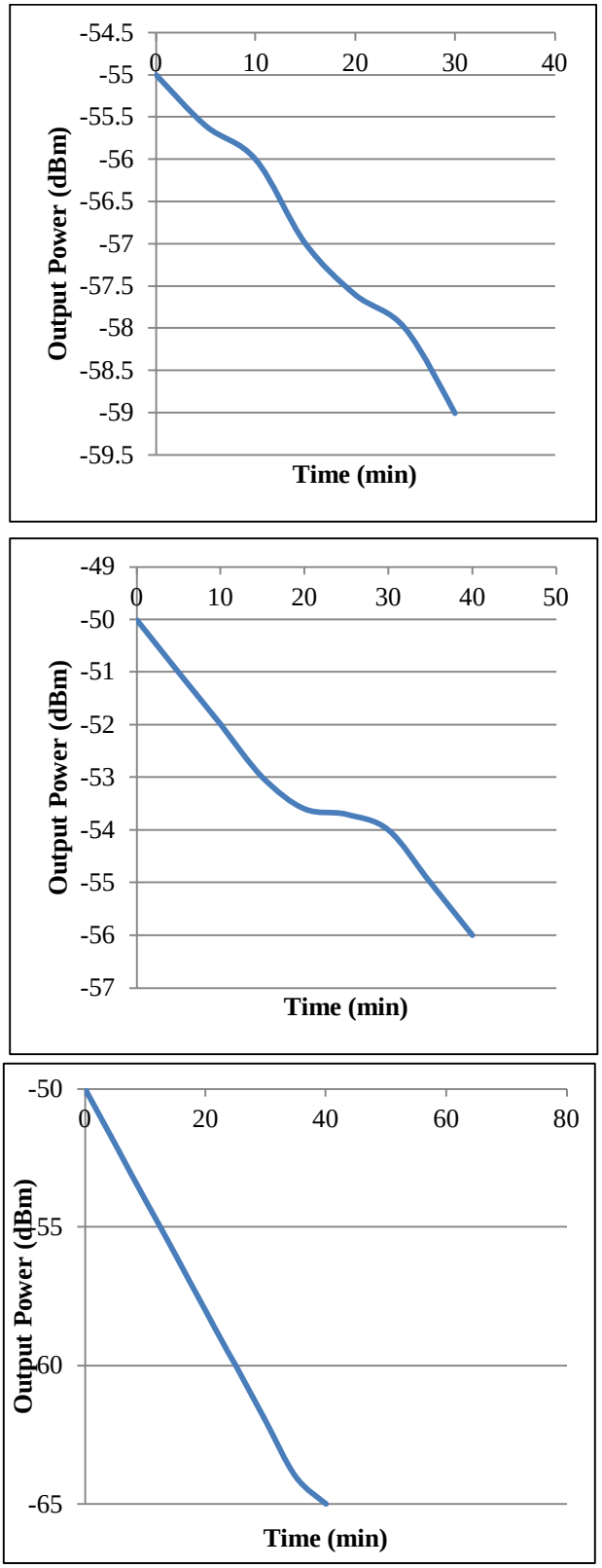

Fig. 8: (A) Output power for the single-mode fiber at (30min), (B) Output power for the single-mode fiber at (40 min), (c) Output power for the single-mode fiber at (60 min)

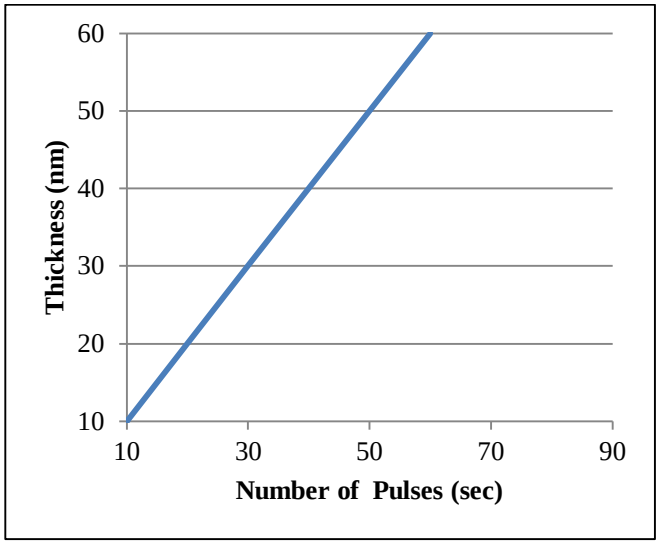

Fig. 9: Thickness of the Fe_3O_4 as a function of pulses in (sec).

4. Conclusion

The tapering process successfully modified the optical fiber geometry in both single-mode and multimode fibers, reducing the fiber diameter and transmitted optical power because of weaker light confinement and increased evanescent-field-related losses. In addition, a thin Fe_3O_4 layer with a thickness of approximately 49.4 nm was successfully deposited onto the tapered region by pulsed laser deposition, while a paraffin oil-based magnetic fluid containing Fe_3O_4 nanoparticles was prepared and applied to create a magnetically responsive sensing medium. The combined use of the solid coating and magnetic fluid improved the sensitivity of the optical fiber sensor. Overall, the developed optical fiber structure demonstrates strong potential for compact, low-cost, and highly sensitive magnetic field sensing, with promising applications in magnetic field monitoring, environmental sensing, and industrial measurement systems.

Author Declaration

The authors declare that this manuscript is original, has not been published before, and is not under consideration for publication elsewhere.

Author's Contributions

The first author performed the experimental work, collected and analyzed the data, and wrote the manuscript. The second author supervised the work, contributed to the interpretation of the results, and revised the manuscript. All authors approved the final manuscript.

References

[1] G. Keiser, "Optical Fiber Communications", 4th ed. New York, NY, USA: McGraw Hill, (2011).
[2] G. P. Agrawal, "Fiber-Optic Communication Systems", 4th ed. Hoboken, NJ, USA: Wiley, (2012).
[3] C. Pendão, and I. Silva, "Optical Fiber Sensors and Sensing Networks: Overview of the Main Principles and Applications", Sensors, 22 (19), 7554 (2022). https://doi.org/10.3390/s22197554
[4] M. Elsherif, A. E. Salih, M. Gutiérrez Muñoz, F. Alam, A. K. Yetisen, and H. Butt, "Optical Fiber Sensors: Working Principle, Applications, and Limitations", Advanced Photonics Research, 3 (11), 2100371 (2022). https://doi.org/10.1002/adpr.202100371

[5] E. Urrutia, I. Ayesta, M. Azkune, M. A. A. N. Illarramendi, M. A. Illarramendi, and J. Zubia, "Recent Advances in Sensor Applications of Microstructured Optical Fibers: A Review", IEEE Sensors Journal, 25 (11), 18584–18607, (2025). https://doi.org/10.1109/JSEN.2025.3558308
[6] S. Korposh, S. W. James, S. W. Lee, and R. P. Tatam, "Tapered Optical Fibre Sensors: Current Trends and Future Perspectives", Sensors, 19 (10), 2294 (2019). https://doi.org/10.3390/s19102294
[7] S. K. Dontha, K. Vejandla, and S. P. Valluri, "Design and Simulation of a C-Shaped Optical Fiber Sensor for Sensitivity Enhancement", Journal of Optics, 2025. https://doi.org/10.1007/s12596-025-02701-y
[8] M. A. Riza, Y. I. Go, and R. R. J. Maier, "Dynamics Rate of Fiber Chemical Etching: New Partial Removal of Cladding Technique for Humidity Sensing Application", Laser Physics, 30 (12), 126205 (2020). https://doi.org/10.1088/1555-6611/abbe83
[9] B. S. Ali, and S. S. Al-Bassam, "Tapered Coated Coreless Optical Fiber Pollution Sensor", Journal of Physics: Conference Series, 2114 (1), 012054 (2021). https://doi.org/10.1088/1742-6596/2114/1/012054
[10] X. Wang, Y. Liao, D. Zhang, T. Wen, and Z. Zhong, "A Review of Fe_3O_4 Thin Films: Synthesis, Modification and Applications", Journal of Materials Science & Technology,34 (8), 1259–1272 (2018). https://doi.org/10.1016/j.jmst.2018.01.011
[11] X. Huang, and J. Ding, "The Structure, Magnetic and Transport Properties of Fe_3O_4 Thin Films on Different Substrates by Pulsed Laser Deposition", Journal of the Korean Physical Society, 62 (12), 2228–2232 (2013). https://doi.org/10.3938/jkps.62.2228
[12] K. A. Abdulkareem, S. Kadhim, and S. B. Ali, "The Structural and Optical Properties of Nanocrystalline Fe_3O_4 Thin Films Prepared by PLD", Engineering and Technology Journal, 40 (2), 334–342 (2022). https://doi.org/10.30684/etj.v40i2.2235
[13] B. Bateer, Y. Qu, X. Meng, C. Tian, S. Du, R. Wang, K. Pan, and H. Fu, "Preparation and Magnetic Performance of the Magnetic Fluid Stabilized by Bi-Surfactant", Journal of Magnetism and Magnetic Materials, 332, 151–156, (2013). https://doi.org/10.1016/j.jmmm.2012.12.009
[14] Q. Xiang, Y. Ying, J. Xue, H. Wang, H. Yan, Y. Wang, H. Dai, Q. Yuan, and B. Zhou, "Liquid-Metal-Based Magnetic Fluids", Nature Reviews Materials, 9, 433–449 (2024). https://doi.org/10.1038/s41578-024-00679-w
[15] G. M. Jassam, S. S. Alà, and M. F. Sultan, "Fabrication of a Chemical Sensor Based on Surface Plasmon Resonance via Plastic Optical Fiber", Iraqi Journal of Science, 61 (4), 765–771 (2020). https://doi.org/10.24996/ijs.2020.61.4.8
[16] N. S. Rahim, S. S. Ahmed, and M. F. Sultan, "Optical Fiber Biomedical Sensor Based on Surface Plasmon Resonance", Iraqi Journal of Science, 61 (7), 1650–1656 (2020). https://doi.org/10.24996/ijs.2020.61.7.13
[17] G. M. Jassam, "Acetic Acid Concentration Estimation Using Plastic Optical Fiber Sensor Based Surface Plasmon Resonance", Iraqi Journal of Physics, 17 (43), 11–17 (2019). https://doi.org/10.30723/ijp.v17i43.482
[18] A. I. Mahmood, A. I. Mahmood, and S. S. Ahmed, "Refractive Index Sensor Based on Micro-Structured Optical Fibers with Using Finite Element Method", Iraqi Journal of Science, 59 (3), 1577–1586 (2018), https://doi.org/10.24996/ijs.2018.59.3C.5
[19] G. M. Jassam, and S. S. Ahmed, "Tapered PCF mach–zehnder interferometer based on surface plasmon resonance (SPR) for estimating concentration toxic metal ions (lead)", Journal of Optics, 53(1), 163–168 (2024). https://doi.org/10.1007/s12596-022-01086-6
[20] H. S. Raham, and S. S. Al-Bassam, "Optical fiber sensor based on surface plasmon resonance for detection of Escherichia coli (E. coli)", Journal Of Optics, 52(2), 631–636 (2023). https://doi.org/10.1007/s12596-022-01007-7
[21] G. M., Jassam, Z. A., Abbas, and S. H. Mohammed, "Single mode optical fiber sensor based on surface plasmon resonance for the detection of the lactic acid for the chemical sensor", Journal of Optics. (2024). https://doi.org/10.1007/s12596-024-02211-3

ألياف بصرية مدببة ومطلية بجسيمات نانوية من أوكسيد الحديد وسائل مغناطيسي للكشف عن المجال المغناطيسي (Fe_3O_4)

فاطمة عادل حميد*، سؤدد سلمان أحمد

قسم الفيزياء، كلية العلوم، جامعة بغداد، بغداد، العراق

البريد الالكتروني للباحث:fatma.adel1704a@sc.uobaghdad.edu.iq

الخلاصة: في هذا العمل تم تطوير مستشعر ألياف بصرية للكشف عن المجال المغناطيسي حيث تم استخدام ألياف أحادية النمط ومتعددة الأنماط اعتمادا على عمليتين رئيسيتين، هما الحفر الكيميائي باستخدام حامض الهيدروفلوريك (HF) وترسيب طبقة من جسيمات أوكسيد الحديد (Fe_3O_4) تم ترسيب الجسيمات النانوية باستخدام تقنية الترسيب بالليزر النبضي (PLD) باستخدام ليزر من نوع (Nd:YAG) بطول موجي قدره 1064 نانومتر وعدد 70 نبضة، حيث تم الحصول على سمك يقارب 49.4 نانومتر في منطقة الاستشعار.يوضح هذا العمل استخدام جسيمات (Fe_3O_4) في عملية الطلاء من خلال تقنيتين مختلفتين ضمن منظومة الألياف البصرية حيث تم في التقنية الأولى ترسيب الجسيمات النانوية كطبقة صلبة باستخدام تقنية (PLD) مما أتاح الحصول على سمك ضمن المدى النانوي (40–60 نانومتر) حيث يوفر سطحا فعالا للتفاعل. أما في التقنية الثانية، فقد تم استخدام جسيمات (Fe_3O_4)في تحضير سائل مغناطيسي يعمل كطبقة طلاء سائلة، مكونا وسطا مستقرا ومستجيبا للمجال المغناطيسي. إن هذا الاستخدام المزدوج للطلاء الصلب والسائل يوفر تفاعلا أكثر كفاءة مقارنة باستخدام تقنية طلاء واحدة فقط .تم تحضير السائل المغناطيسي عن طريق تشتيت 5 غرام من مسحوق (Fe_3O_4) في 13 غرام من زيت البارافين. وأظهرت النتائج التجريبية أنه مع زيادة زمن الحفر الكيميائي باستخدام (HF) ينخفض قطر الليف البصري ويصاحب ذلك انخفاض في القدرة الضوئية المنتقلة. وتتفق هذه النتائج مع دراسات سابقة، والتي بينت أن عملية التخصير باستخدام حمض الهيدروفلوريك (HF) تحول الليف البصري التقليدي إلى عنصر حساس قادر على الاستجابة للتغيرات الخارجية. وبذلك يوفر هذا النهج المقترح طريقة فعالة لتحسين حساسية الألياف البصرية مما يجعلها مناسبة للاستخدام في تطبيقات استشعار المجال المغناطيسي.